University of Alberta

Multiple Microbial Processes in Membrane Aerated Biofilms Studied Using Microsensors

by

Shuying Tan

A thesis submitted to the Faculty of Graduate Studies and Research
in partial fulfillment of the requirements for the degree of

Doctor of Philosophy

in

Environmental Science

Department of Civil and Environmental Engineering

Fall 2012

Edmonton, Alberta

Abstract

Membrane aerated biofilms (MABs) have exhibited unique advantages over conventional biofilms for wastewater treatment. However, due to the limited available technology to probe the internal biofilms, the information for multiple microbial processes inside the MABs is quite inadequate. Microsensor techniques make it feasible to detect chemical gradients and herein explore the microbial activities of processes inside biofilms. In this work, multiple microbial processes including sulfate reduction, sulfide oxidation, nitrification and denitrification inside the MABs were investigated using microsensor techniques. O_2, pH, H_2S, ORP, NH_4^+ and NO_3^- microsensors were successfully fabricated and implemented to measure *in situ* the corresponding chemical gradients inside the MABs.

The amperometric H_2S microsensor was further developed and displayed linear response within the range of 0 - 600 μM (20.4 mg L^{-1}) total sulfide concentration with a high sensitivity up to 1.21 pA $\cdot \mu M^{-1}$. The response time could be less than 1 second. This H_2S microsensor was used to measure the change of H_2S concentrations from the low to high and from the high to low.

The simultaneous occurrence of multiple microbial processes inside a piece of MAB has been revealed using microsensor techniques. The multiple microbial processes were stratified: sulfate reduction followed by denitrification and sulfide oxidation near the bulk liquid-biofilm interface; nitrification in the middle; and aerobic oxidation near the membrane. These results were promising in providing multi-functional biofilms for engineering applications.

COD/SO_4^{2-} ratios of 1 and 2 at constant COD concentration were examined to evaluate the effects of COD/SO_4^{2-} ratios on the ability of simultaneous multiple microbial processes. The results showed that under the two conditions, the activity of sulfate reduction at COD/SO_4^{2-} ratio of 1 was higher. COD/NH_4^+ ratios of 4 and 10 at constant COD concentration were investigated to check the effects of COD/NH_4^+ ratio on the occurence of simultaneous multiple microbial processes. It was found that nitrification and denitrification activities at a COD/NH_4^+ ratio of 4 were higher than those at a COD/NH_4^+ ratio of 10.

The biofilm structures were observed using scanning electron microscopy. Microscopic observations showed the denser structure near the bulk liquid-biofilm interface and porous structure near the membrane.

Acknowledgements

I would like to express my sincere gratitude to the following people who contributed to this work and provided assistance to me.

First, I would like to appreciate my supervisor, Dr. Tong Yu. His guidance, support and encouragement are invaluable to successfully complete my research and dissertation. I am indebted to Dr. Selma Guigard and Dr. Yang Liu, who served as the members of my supervisory committee. Their advice and critique on my dissertation research are highly treasured. I also thank Dr.Hermann Eberl and Dr. Jingli Luo who served as the members of my final oral examining committee.

I am grateful to the following people for their assistance and kindness during this research. Dr. Phillip M. Fedorak in the Department of Biological Sciences served for my candidacy examination member and provided invaluable suggestion for my following research. He also allowed me to use his lab and staff to conduct the experiment of fluorescence in situ hybridization. Mr. Roman Lipiecki in the machineshop of the Department of Chemistry and Mr. Allan M. Muir from Argyll Innovations Inc. provided their assistance in constructing the membrane aerated biofilm reactors. The following staff and my colleagues in the Department of Civil and Environmental Engineering offered their kind laboratory assistance: Maria Demeter, Jela Burkus, Kusumakar Sharma, Sabinus Okafor, Shujie Ren, Miao Yu and Hong Liu.

I would like to acknowledge the financial supports for my research from Natural Sciences and Engineering Research Council of Canada (NSERC), China

Scholarship Council (CSC) and Queen Elizabeth II Graduate Scholarship.

Finally, I would like to thank my family members. A special contributor to this research is my husband, Xinhu Tang. He was always there to support me during my frustrating times and provide possible assistance during my experiment and thesis writing.

Table of Contents

List of Tables

List of Figures

List of Abbreviation

AOB	-Ammonia-Oxidizing Bacteria
CLSM	-Confocal Laser Scanning Microscopy
COD	-Chemical Oxygen Demand
DI	-Deionized
DO	-Dissolved Oxygen
FISH	-Fluorescence in situ Hybridization
ID	-Inner Diameter
LIX	-Liquid Ion-Exchange
MABR	-Membrane Aerated Biofilm Reactor
MAB	-Membrane Aerated Biofilm
OD	-Outer Diameter
ORP	-Oxidation-Reduction Potential
SEM	-Scanning Electron Microscopy
SRB	-Sulfate Reducing Bacteria

Chapter 1

Introduction

1.1 Membrane aerated biofilm reactors

Membrane aerated biofilm reactors (MABRs), as a novel type of biofilm process, have attracted increasing interets in the past decades (Casey *et al.*, 1999; Terada *et al.*, 2003). In MABRs, gases (*e.g.*, oxygen) diffuse through membranes into membrane aerated biofilms (MABs), while liquid substrates (*e.g.*, organic carbon) pass through in the opposite direction, i.e. from the bulk liquid into the MABs. This is called "counter-diffusion" mass transfer inside the MAB (Figure 1-1). In conventional biofilm reactors, biofilms grow on a non-permeable substratum. Gases and liquid substrates are both supplied from the bulk liquid, which is named "co-diffusion" mass transfer inside the conventional biofilm (Figure 1-1).

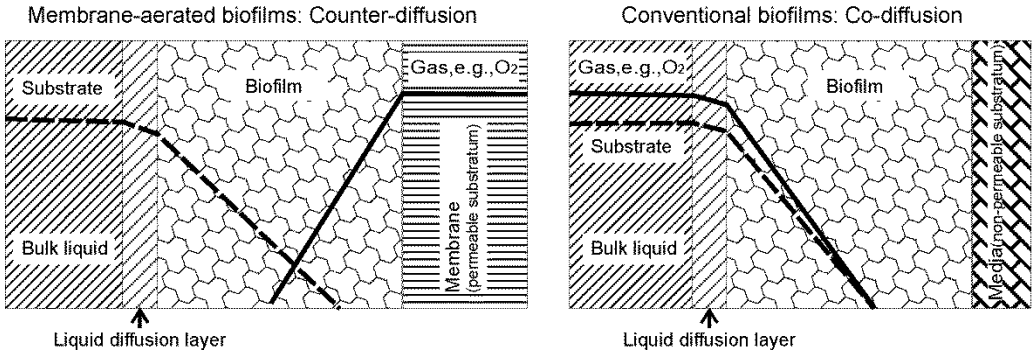

Figure 1-1 Illustrative diagrams of "counter-diffusion" of substrates and gas in MABs (left) and "co-diffusion" of substrates and gas in conventional biofilms (right)

Compared with conventional biofilm reactors, MABRs have the following advantages: 1) flexibility to manipulate biofilm processes by controlling gases and liquid substrates from the opposite side of the biofilms; 2) high gas utility efficiency due to the bubbleless aeration from the membranes supporting biofilm growth; and 3) low capital and operational costs. For example, simultaneous nitrification and denitrification can be achieved in one piece of MAB, so there is no need for complex aeration systems, additional tanks, piping or pumps (Nerenberg, 2005; Cole, 2005).

The MABs growing on gas permeable membranes are perhaps the most important feature inside the MABRs (LaPara *et al*., 2006). As a result of the different mechanisms of mass transfer, the stratification of microbial processes in MABs might be quite different from that of conventional biofilms. For example, the active layer is generally considered to be present in the outer region (near the bulk liquid-biofilm interface) of conventional biofilms (Casey *et al.*, 1999). But for MABs, it is considered to exist in the middle (Cole *et al.*, 2005). Although the unique configuration of mass transfer (counter-diffusion) might result in a unique and complex microbial community arrangement, researchers know very little about the internal structure and functions of the microenvironments inside the MABs. The "counter-diffusion" of gases and substrates within MABs makes it possible to manipulate the biofilm processes by controlling gas pressure and substrate concentrations. Previous studies mainly focused on nitrification and denitrification in oxygen-based MABR which applies oxygen as gas supply. In an oxygen-based MABR, aerobic oxidation and nitrification could be achieved if

oxygen fully penetrated the MAB. Under oxygen limiting conditions, denitrification might occur in an anoxic region near the bulk liquid-biofilm interface where the concentration of organic carbon is high. Under the same conditions, nitrification might be present in an oxic region near the biofilm-membrane interface where the concentration of organic carbon is low in the same piece of biofilm (Cole, 2005). This may explain, in previous studies, why simultaneous nitrification and denitrification were observed in a piece of MAB (Cole, 2005). However, in a conventional biofilm reactor, due to the co-diffusion of mass transfer, if nitrification occurs in the oxic region near the biofilm-bulk liquid interface where the concentration of organic carbon is low, denitrification should not be present in the same piece of biofilm. This is because heterotrophic denitrifying bacteria need more organic carbon than autotrophic nitrifying bacteria.

Previous studies on nitrification and denitrification did provide profound insights into the understanding of MABs (Hibiya *et al.*, 2003; Terada *et al.*, 2003), but the information on sulfate reduction is needed to expand the understanding of microbial processes in oxygen-based MABs. It has been demonstrated that sulfate reduction plays a significant role in wastewater treatment (Freese and Stuckey, 2004). Sulfate reduction was generally considered a chemoheterotrophic process because most sulfate reducing bacteria (SRB) could obtain carbon from organic matters (Maier *et al.*, 2000). In addition, H_2S, the main end product of sulfate reduction, could be corrosive to concrete pipes, malodorous and toxic to humans. Therefore, a better understanding of sulfate reduction in oxygen-based MABs will

enhance the perception of the relationships among multiple microbial processes, and therein, to improve the manipulation of biofilm processes. The studies on the occurrence of simultaneous multiple microbial processes will provide multi-functional biofilms for engineering applications.

Since biological systems are considered to be sensitive to reactor conditions (Cole, 2005), how reactor conditions affect microbial community structure and activities needs to be explored. The information obtained by studying the microbial processes and the effects of reactor conditions on the occurrence of microbial processes of MABs will improve the fundamental studies on biofilms. More detailed fundamental research will improve the understanding of the microbial community structure and activities, enhance the process performance of MABRs, and help build better mathematical models in aid of full-scale applications of MABRs. In all, better understandings of the microbial processes and the effects of reactor conditions on the occurrence of multiple microbial processes within MABs have both practical and theoretical significance.

Microbial processes are dynamic in biofilms; therefore, analytical tools for *in situ* measurements are important to understand community structure and activity in oxygen-based MABs. The following section will introduce the essential application of microsensor techniques on the biofilm studies.

1.2 Microsensor techniques

Microsensor techniques as a set of tools to study biofilms exhibit their unique advantages in *in situ* determination of chemical gradients and bacterial

activities in microbial communities. They allow for the probings of local microenvironments and quantification of local chemistry at the micrometer-scale level with high spatial and temporal resolutions (Santegoeds *et al.*, 1998; Revsbech, 2005; de la Rosa and Yu, 2005; Lewandowski and Beyenal, 2007). In the metabolic activities of the microorganisms, the consumption of certain substrates and generation of metabolic products will alter the distribution of chemical species in biofilms. The information on microbial activities and mass transport of these chemical species in biofilms can be obtained from the concentration profiles of these chemical species measured by specific microsensors. This information cannot be obtained by using macro-scale measurements. With the development of microsensor techniques, previously unavailable chemical and microbial information inside biofilms has become accessible. This information has revealed the structure and functions of biofilm, as well as the relationship between microbial activities and the occurrence of specific microorganisms in a biofilm community (Lewandowski and Beyenal, 2007).

Although microsensor techniques provided the above advantages, they also brought challenges for biofilm measurements. For instance, in the biofilm studies, the microsensors' tips must be very small and robust enough. The microsensors must also be sensitive and highly selective (Schreiber *et al.*, 2008). Therefore, they require not only sophisticated skills for fabrication, but also good performance for calibration and measurements. Currently, there are only a few microsensors used in biofilm studies, such as oxygen (O_2), sulfide (S^{2-}), pH,

oxidation-reduction potential (ORP), ammonia (NH_4^+) and nitrate (NO_3^-) microsensors (Lewandowski and Beyenal, 2007; Revsbech, 2005). Different microsensors have different measuring theories, properties and performance, and require different fabrication skills. For instance, a liquid ion-selective ammonia microsensor measures the membrane potential which is determined as a function of ammonia ion concentration (Lewandowski and Beyenal, 2007). It can be fabricated with a very small tip. However, its lifetime is usually short, 1-5 days depending on the frequency of the usage (Revsbech, 2005). A combined oxygen microsensor measures the limiting current, which is linearly proportional to oxygen partial pressure when oxygen crosses the external surface of the membrane (Lu and Yu, 2002). Its fabrication procedure is complicated and it is very challenging to fabricate a combined oxygen microsensor with a small tip. Nevertheless, the combined oxygen microsensor has a long lifetime up to 6 months, and it is less subject to electromagnetic interference because the cathode, anode and guard electrode are assembled in one body.

To investigate multiple microbial processes in biofilms using microsensor techniques, all microsensors should be prepared and calibrated before biofilm measurements. However, it is challenging to prepare different types of microsensors for studying dynamic biofilms in a period of one or two days. The more microsensors involved, the more challenging it becomes. In addition, the microbial matrix inside the biofilms might shorten a microsensor's lifetime. For time management, it might take more than 20 hours for one skilled person to continuously conduct one set of measurements using six kinds of microsensors.

Based on current understanding of biofilms, the measured profiles following the procedures in most previous studies may not be the profiles that actually occurred under growth conditions in the biofilm reactor (Okabe *et al*., 1999). Most of the previous studies on microsensor measurements in biofilms mainly followed the following procedure: biofilms were taken from reactors and incubated in a synthetic medium (Okabe *et al.*, 1999) or filtered wastewater from wastewater treatment plants (de la Rosa, 2005) in a flow chamber for a certain period of time before measurements were made. Therefore, to accurately reflect what happened in the biofilm, the profiles measured using microsensors under the growth conditions are necessary (Okabe *et al.*, 1999).

1.3 Objectives

The overall goal of this research is to expand the fundamental understanding of the internal structure and function of biofilms, and herein, benefit the design and operation of MABRs. Specifically, the objectives of this research are as follows:

1. Develop H_2S microsensor techniques. This research is to further develop a H_2S microsensorto detect the end product of sulfate reduction, H_2S. It will also expand the understanding of the internal structure and functions of MABs by using the H_2S microsensor in combination with O_2, NH_4^+, NO_3^-, ORP and pH microsensors,.
2. Measure concentration profiles and chemical gradients in MABs ***in situ.*** To investigate simultaneous multiple microbial processes in one

piece of MAB, it is important to measure the profiles of O_2, H_2S, NH_4^+, NO_3^-, ORP and pH under growth conditions without taking biofilms out of the reactors. The biofilms reactors will be designed for this purpose.

3. Investigate simultaneous multiple microbial processes in a single piece of biofilm. Specifically, nitrification, denitrification, sulfate reduction, sulfide oxidation and aerobic oxidation will be examined using microsensor techniques.
4. Investigate the effects of the operating conditions on the occurrence of multiple microbial processes in MABs. Specifically, the effects of chemical oxygen demand (COD)/NH_4^+-N and COD/SO_4^{2-} ratios in the bulk liquid will be investigated using microsensor techniques.

1.4 Overall approach

The overall approach of this research is to characterize the structure and microbial activity within MABs using microsensor techniques. MABRs were designed and operated under specified and well-defined conditions. During the operation period, the wastewater composition in bulk liquid, such as COD, SO_4^{2-} and NH_4^+ were regularly measured. When the MABs reached pseudo-steady state and the O_2, H_2S, NH_4^+, NO_3^-, ORP and pH microsensors with good performance were fabricated, the six types of microsensors were used to measure the chemical gradients. The results from the microsensor measurements are to investigate the occurrence of multiple microbial processes, such as sulfate reduction, nitrification

and denitrification within one piece of MABs. After the first set of microsensor measurements, the operational conditions of the MABR were changed. When the MABs reached a new pseudo-steady state status, another set of microsensor measurements was taken. The reactors were operated under different COD/NH_4^+-N and COD/SO_4^{2-} ratios in order to study the effects of the operational conditions on the occurrence of multiple microbial processes in MABs. Finally, the biofilms together with the membranes were cut and taken out of the reactors to observe the microbial structure using scanning electron microscopy (SEM). Figure 1-2 shows a schematic diagram of the overall approach of this research.

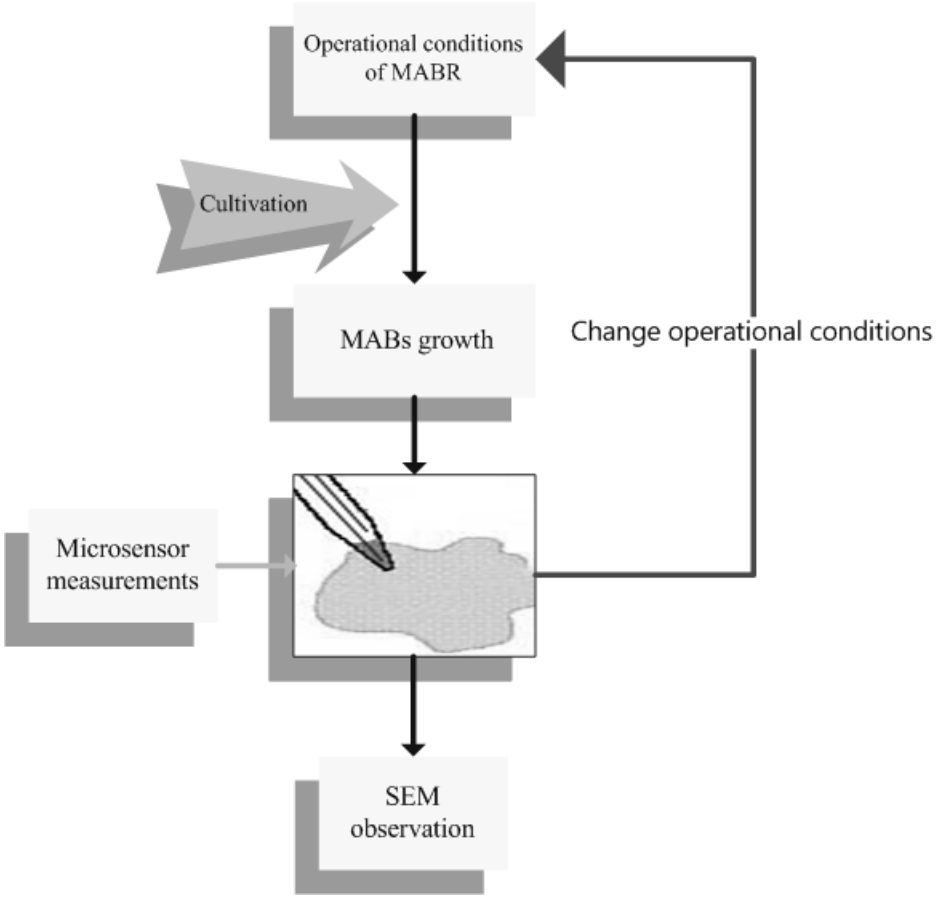

Figure 1-2 Schematic diagram of the overall approach of this research

1.5 Outline of the dissertation

This dissertation is presented in the following structure:

Chapter 1 introduces the background information on MABRs, MABs, biofilm processes and microsensor techniques. The objectives and overall approach of this research are also covered.

Chapter 2 is the literature review. It includes four sections, the first of which is a review of MABRs: the selection of membrane types, the application of MABRs, as well as the effects of operational conditions on reactor performance in MABRs. The second section reviews biofilm structure and activities: the factors affecting biofilm structure and activity, structure and activity in conventional biofilms, as well as structure and activity in MABs. The third section covers a review of SRB and biological sulfate reduction: the growth, metabolism and distribution of SRB in biological sulfate reduction process. The final section reviews the characterization methods of biofilms: microsensors and microscopy techniques.

Chapter 3 presents materials and methods applied in this research. It includes the design, setup and selection of operational conditions for MABRs. It also describes the fabrication and calibration of O_2, pH, ORP, NH_4^+ and NO_3^- microsensors. The set-up of microsensor measurement is present too. Microscopy observation for the MABs is finally introduced.

Chapter 4 describes the newly developed H_2S microsensor technique, including its fabrication procedure, the factors affecting its performance, and its application in biofilm measurement.

Chapter 5 investigates simultaneous multiple microbial processes, including sulfate reduction, nitrification and denitrification in a piece of MAB.

Chapter 6 examines the effects of operational conditions, the ratio of COD/SO_4^{2-} and COD/NH_4^+-N, on the occurrence of simultaneous sulfate reduction, nitrification and denitrification in the MAB.

Chapter 7 concludes this research and provides recommendations for future studies.

References

Barton, L. L. 1995. Sulfate-reducing bacteria. New Jork: Plenum press.

Casey, E., Glennon, B. and Hamer, G. 1999. Review of membrane aerated biofilm reactors. Resources Conservation and Recycling 27(1-2): 203-215.

Cole, A. C. 2005. Characterization of membrane-aerated biofilms for wasterwater treatment, Univeristy of Minnesota. Doctor of Philisophy thesis.

De la Rosa, C. and Yu, T. 2005. Three-dimensional mapping of oxygen distribution in wastewater biofilms using an automation system and microsensors. Environmental Science & Technology 39(14): 5196-5202.

Freese, L. H. and Stuckey, D. C. 2004. Anaerobic treatment of sulphate-enriched wastewaters. Proceedings of the Institution of Civil Engineers-Water Management 157(4): 187-195.

Hibiya, K., Terada, A., Tsuneda, S. and Hirata, A. 2003. Simultaneous nitrification and denitrification by controlling vertical and horizontal

microenvironment in a membrane-aerated biofilm reactor. Journal of Biotechnology 100(1): 23-32.

LaPara, T. M., Cole, A. C., Shanahan, J. W. and Semmens, M. J. 2006. The effects of organic carbon, ammoniacal-nitrogen, and oxygen partial pressure on the stratification of membrane-aerated biofilms. Journal of Industrial Microbiology & Biotechnology 33(4): 315-323.

Lewandowshi, Z. and Beyenal, H. 2007. Fundamentals of biofilm research. Boca Raton: CRC Press Taylor &Francis Group, p176-192.

Lu, R. and Yu, T. 2002. Fabrication and evaluation of an oxygen microsensor applicable to environmental engineering and science. J. Environ. Eng. Sci. (1): 225-235.

Maier, R. M., Pepper, I. L. and Gerba, C. P. 2000. Environmental Microbiology. Academic Press

Nerenberg, R. 2005. Membrane biofilm reactors for water and wastewater treatment. A Seminar on Advances in Water and Wastewater Treatment, Borchardt.

Okabe, S., Satoh, H. and Watanabe, Y. 1999. *In situ* analysis of nitrifying biofilms as determined by *in situ* hybridization and the use of microsensors. Applied and Environmental Microbiology 65(7): 3182-3191.

Revsbech, N. P. 2005. Analysis of microbial communities with electrochemical microsensors and microscale biosensors. Environmental Microbiology. 397: 147-166.

Santegoeds, C. M., Schramm, A. and de Beer, D. 1998. Microsensors as a tool to determine chemical microgradients and bacterial activity in wastewater biofilms and flocs. Biodegradation 9(3-4): 159-167.

Schreiber, F., Polerechy L. and de Beer, D. 2008. Nitric Oxide Microsensor for High Spatial Resolution Measurements in Biofilms and Sediments. 80(4): 1152-1158

Terada, A., Hibiya, K., Nagai, J., Tsuneda, S. and Hirata, A. 2003. Nitrogen removal characteristics and biofilm analysis of a membrane-aerated biofilm reactor applicable to high-strength nitrogenous wastewater treatment. Journal of Bioscience and Bioengineering. 95(2): 170-178.

Chapter 2

Literature Review

2.1 Membrane aerated biofilm reactors

In MABRs, gas permeable membranes are employed as the substratum for biofilm growth and gas delivery. Gases and liquid substrates for biofilm growth are generally supplied from the opposite sides of the membranes (Figure 1-1). In this section, the types of gas permeable membranes, the types of gases delivered and reactor operational conditions in MABRs, which are believed to be important for the growth and stratification of MABs, are to be reviewed.

The gas permeable membranes used in MABRs are classified into three types: hydrophobic microporous membranes such as polypropylene, dense film membranes such as silicone rubber, and composite membranes which consist of a microporous membrane coated with a thin film of dense material (Casey *et al*., 1999). Table 1 shows the membrane types, examples of membrane materials, configurations and mass transfer characteristics in MABRs.

Different types of gas permeable membranes have different mass transfer characteristics for gases. Casey *et al* (1999) reviewed the following mass transfer characteristics for different types of membranes. The mass transfer through microporous membranes is facilitated by the diffusion through the gas-filled pores. The microporous membranes are inexpensive and can be made very thin. Therefore, their mass transfer resistance could usually be negligible. However, the problems of pore clogging and the catastrophic liquid entry into pores can easily

occur. Also, the low bubble point of the microporous membranes can limit the maximum intra-membrane pressure if bubble formation needed to be prevented. The mass transfer through dense film membranes is due to high permeability of components to be transported. For example, silicone can be used as gas permeable membrane in MABRs because oxygen is highly soluble in silicone. The dense membranes have a much thicker wall and a higher bubble point than microporous membranes, which could allow high intra-membrane gas pressures up to 695 kPa (Wang, 2005). Usually, dense membranes can allow higher intra-membrane gas pressures than microporous membranes. The intra-membrane oxygen pressure is proportional to oxygen supply rate. Composite membranes had the combined properties of the microporous and dense membranes.

Table 2-1 Membrane types, material examples, configurations and mass transfer characteristics in MABRs

Membrane Types	**Examples of membrane material**	**Configurations**	**Mass Transfer Characteristics**
Microporous	Polytetrafluoroethane, polypropylene, polyetherimide, polyethylene	Tubular, flat sheet, hollow fiber, plate and frame; dead end or flow through	Negligible Resistance, Inexpensive, Pore clogging, low bubble point
Dense	Silicone		Good oxygen selection High bubble point
Composite	Silicone with fibrous support		Combination of the microporous and dense type

Tubular and hollow fiber configurations of membrane modules have been studied more frequently than other configurations (*e.g.* flat sheet), which might be due to their larger specific surface area. The specific surface area could reach up to 550 m^2 m^{-3} for tubular dead-end operation and 5180 m^2 m^{-3} for hollow fiber dead-end operation (Casey *et al*., 1999), which is advantageous for biofilm growth. The operation mode of the membrane modules, either dead-end or flow-through, affects the gas utilization rate and reactor's performance. The dead-end operation was reported to decrease significantly the performance and to cause condensate formation in the lumen (Cote *et al*., 1988). With the bubbleless aeration, the gas delivery mode of the dead-end operation could get the 100% gas utilization but might cause uneven gas delivery along the membrane length. The gas delivery mode of flow-through operation could make the gas delivery uniform but the utilization rate of gas substrates could decrease.

In MABRs, the gases through the lumen of the membrane can be oxygen, hydrogen, methane, etc. Oxygen-based (oxygen through the lumen of the membrane) and hydrogen-based (hydrogen through the lumen of the membrane) MABRs have been more extensively studied than other types of gas-based MABRs. Methane-based (methane through the lumen of the membrane) MABRs were used to co-metabolically degrade trichloroethylene (Clapp *et al*., 1999). Current studies on MABRs mainly focused on the reactor performance, except a few that focused on the structure and function of MABs in oxygen-based MABRs.

Hydrogen-based MABRs have been studied for denitrification and sulfate reduction in water and wastewater treatment. Nerenberg (2005) reviewed the

hydrogen-based MABRs for denitrification in drinking water and wastewater treatment. Terada *et al*. (2006a) found from the reactor performance that denitrification and sulfate reduction occurrred simultaneously in a single hydrogen-based MABRs treating synthetic wastewater containing sulfate concentration of 120-150 g m^{-3} S. This study suggested the hydrogen flux control through the gas permeable membrane could be used to suppress the occurrence of sulfate reduction. The relationship between sulfate reduction and ORP in the bulk liquid was also examined in the same study. When ORP in the bulk solution was around 0 mV, sulfate reduction was not observed and when ORP decreased to around -300 mV, sulfate reduction was found to occur preferably over denitrification. For the electron-equivalent fluxes of electron acceptors Se(VI), NO_3^- and SO_4^{2-}, sulfate reduction was found to be the biggest consumer of electrons (89%) and proven to be sensitive to hydrogen pressure, while denitrification was insensitive to hydrogen pressure (Chung *et al*., 2006).

Oxygen-based MABRs have been more widely studied in wastewater treatment (Kappell *et al*., 2005; Shanahan *et al*., 2005; Motlagh *et al*., 2006). An exciting new prospect of oxygen-based MABRs is their capacity of the simultaneous nitrogen and organic carbon removal in a single reactor. For high-strength nitrogenous swine wastewater in an oxygen-based MABR, mean removal percentage of total organic carbon and nitrogen could reach 96% and 83%, respectively (Terada *et al*., 2003). Terada *et al*. (2006b) illustrated the mean removal rates of total organic carbon and nitrogen could reach 99% and 96%, respectively, in a long-term sequencing batch MABR. Wu *et al*. (2006)

demonstrated simultaneous organic carbon removal and nitrification in a MABR which incorporated an activated sludge process. Gonzalez-Brambila *et al*. (2006) studied MABR behaviors under different modes of oxygen supply for the treatment of synthetic wastewater and found all of the modes of oxygen supply in MABRs were more efficient than the traditional suspended cell process. Hibiya *et al*. (2003) found simultaneous nitrification and denitrification for domestic modified wastewater by controlling the vertical and horizontal microenvironment in an oxygen-based MABR.

The operational conditions in MABRs were believed to affect the reactor performance and community structure in MABs (Casey, 2000a; Pankhania *et al*., 1999). Table 2-2 illustrates the membrane types, intra-membrane pressure, reactor's size and hydraulics, wastewater's main composition, reactor performance and related results in MABRs.

The effects of different intra-membrane oxygen pressures on the MABs have been investigated (Casey, 2000b; Wang, 2005; Rishell *et al*., 2004). Intra-membrane oxygen pressures have been demonstrated to have a marked effect on the initial biofilm growth rate, on the acetate removal rate, particularly on the biofilm thickness and biofilm structure (Casey, 2000b). In a multi-population mathematical model, the population stratification and general structure of the concentration profiles for a MAB supplied with pure oxygen were similar to those for a MAB supplied with air (Shanahan *et al*., 2005).

The effects of reactor hydraulics on the reactor performance have also been investigated. Pankhania *et al*. (1999) showed that either completely mixed or

plug-flow operation in an oxygen-based MABR process using hollow fiber gas permeable membranes achieved similar COD removal efficiency. Casey *et al*. (2000a) studied the effect of flow velocities on the performance in MABRs. The flow velocities of 2, 6 and 12 cm s^{-1} were conducted, respectively. The flow velocity had an effect on the mass transfer by the diffusion, on the detachment rate and on the maximum biofilm thickness. The greatest steady state biofilm thickness and the greatest diffusion boundary layer thickness occurred at the lowest velocity, 2 cm s^{-1}. Cole *et al*. (2004) demonstrated that ammonia-oxidizing bacteria didn't exist in a MAB at a low flow velocity of 2 cm s^{-1}, while ammonia-oxidizing bacteria and denitrifying bacteria coexisted in a MAB at a high velocity of 14 cm s^{-1}.

Table 2-2 Operational conditions and reactor performance in oxygen-based MABRs

Membrane	Intra-Membrane Pressure	Reactor's size and Hydraulics	Wastewater (ww)'s main composition	Reactor Performance or some related results	Reference
Hollow fiber microporous membrane	Pure oxygen (99.7% O_2)	Plug flow and completely mixed: HRT=34~60min, V=1.35L	Synthetic ww COD: 144~1135 mg L^{-1} NH_3-N: 6.8-53.4 mg L^{-1}	COD removal: 86% for plug flow 89% for complete-mix	Pankhania *et al.*, 1999
Tubular silicone dense membrane	pO_2: 12.5, 25, 50 KPa	Stirred tank: V=1L	Synthetic ww Acetate: 4300 mg L^{-1}	pO_2 and biofilm thickness is most important for acetate removal	Casey, 2000
Hollow fiber microporous membrane	pO_2: 20 KPa	HRT=1.5day V=0.2L	Artificial swine ww NH_3-N: 3000 mg L^{-1}	TOC removal: 96%, Total nitrogen removal: 83%	Terada *et al.*, 2003
Hollow fiber, Silicone membrane	pO_2: 25, 50,75, 100 KPa	Stirred tank: V=1L Fluid rate:2,6,12 cm s^{-1}	Growth medium saturated with methane	O_2 uptake rate: up to 16g m^{-2} d^{-1} Biofilm growth rate:300 μm d^{-1}	Rishell *et al.*, 2004
Hollow fiber microporous membrane	pO_2: 2.5, 5,7.5 KPa	Completely mixed: V=9.6L, HRT:5.3~13.3h	Synthetic and domestic ww: COD:100~300 mg L^{-1}, NH_3-N: 30~60 mg L^{-1}	COD removal: up to 82.3% NH_3-N removal: 77 to 80%	Wang, 2005
Flat-sheet microporous membrane	pO_2: 21 and 75 KPa	V=3L, HRT: 6h; Fluid rate:2,12 cm s^{-1}	Synthetic ww:COD:100 mg L^{-1}, NH_3-N: 25 mg L^{-1}	pO_2, fluid rate, COD:N is important for nitrogen removal	Cole, 2005

2.2 Biofilm structure and activity

2.2.1 Factors affecting biofilm structure and activity

Biofilm formation and its subsequent development play an important role in the biofilm structure and activity. It has been generally recognized that biofilms develop via three distinctive steps: attachment, growth and detachment (Charcklis and Marshall, 1990; Denkhaus *et al*., 2007; Stewart, 1993). Initially, a single microorganism is associated with a substratum through weak, reversible Van de Waals forces followed by a firm, irreversible attachment. The extent of microbial colonization or attachment might be influenced by the roughness and hydrophobicity of a substratum, by the surface composition and hydrophobicity of a cell, as well as by the hydrodynamic forces and nutrient supply of the bulk solution. In the growth step, the cells grow and aggregate into microcolonies. The extracellular polymeric substances that hold the biofilm together are especially important to the integrity of the biofilm. Further increase in cell numbers by cell division and additional cell recruitment from the environment will result in mature biofilms. Finally, the cells are released into the surrounding environment by the detachment process such as abrasion, erosion, sloughing and predator grazing. Abrasion refers to the continuous removal of small particles from the biofilm at the biofilm-liquid interface, and it occurs due to the collision of particles, *e.g.*, during backwash. Erosion also refers to the continuous removal of small particles from the biofilm at the biofilm-liquid interface, but it is caused by the moving fluid. Erosion is considered as the predominant way of detachment in biofilms receiving low substrate loadings under turbulent conditions. Sloughing refers to the detachment of large fragments of biofilm due to the condition changes within

the biofilm

From the above steps of biofilm formation and development, the biofilm structure and activities are dependent on many particular factors. These factors include substratum, substrate availability and mass transport processes (Wuertz and Falkentoft, 2003). They influence the selection of the prevalent biofilm organisms and in turn reflect their metabolic activity. The following sections review the above factors.

Substratum. Properties of the substratum, such as the type and roughness of substratum, affect the attachment of specific microorganisms (Wuertz *et al.*, 2003). Generally, microorganisms are more easily attach onto the rougher and more hydrophobic substratum. Xiaoxia *et al*. (2006) demonstrated that increasing surface hydrophobicity of the substratum enhanced the attachment of two kinds of anaerobic SRB (*Desulfovibrio* and *Desulfuricans*) and one kind of aerobe (*Pseudomonas*) to the surface. Cao *et al*. (2006) found the specific functional structure of the substratum surface determined the extent of attachment. Silva *et al*. (2006) studied the adhesion of SRB and methanogenic archaea on different support materials of biofilms growing in anaerobic differential reactors. In this study, SRB was found to grow more dominantly on polyurethane foam and vegetal carbon than low-density polyethylene and alumina-based ceramics.

Substrate. Substrate type, concentration and kinetics also play important roles in biofilm structure and activity (Wuertz and Falkentoft, 2003). Cole (2005) demonstrated COD and NH_4^+ concentration had a marked effect on the activity of nitrification and denitrification. Fry *et al*. (1997) studied the changes of microbial structure in anaerobic biofilms. They found that SRB and methanogens co-existed

regardless of sulfate availability as electron acceptors. Esterl *et al*. (2003) described the effect of substrate concentration and fluid flow on biofilm structure. The biofilm structure was considered to be affected by two fluid-dynamic mechanisms: the flow-induced transport of nutrients and the flow-induced mechanical stress. The flow-induced transport of nutrients is represented by Damkohler number, which is defined as the ratio between the maximum conversion rate of the biofilm and the maximum mass transfer rate (equal to the mass transfer coefficient times the inflow substrate concentration). When the maximum conversion rate is much larger than the maximum mass transfer rate, the substrate transport by convection and diffusion is the conversion limiting process. In this case, the biofilm growth rate and biofilm structure strongly depend on the flow-induced mechanical stress. The biofilm structure in this case can be described as scarcity due to the substrate limitation. When the maximum mass transfer rate exceeds the maximum conversion rate, the microorganisms have enough substrate and the biofilm growth rate doesn't depend on flow-induced mechanical stress. Generally, the biofilms will develop into a loose and slack structure at lower flow-induced mechanical stress and a compact and dense structure at higher flow-induced mechanical stress.

Different substrate concentrations might grow or colonize different microbial populations. Morgenroth (2003) and Bishop (2003) found faster-growing heterotrophs were found to be dominant at the biofilm surface with high substrate concentrations, whereas slower-growing autotrophs were found to be closer to the solid substratum where the substrate concentration was low. It is explained that slower-growing autotrophs can balance their need with their slower

replacement for nutrients.

2.2.2 Structure and activity in conventional biofilms

Previous studies on conventional biofilms have revealed that the biofilms were quite heterogeneous (de Beer *et al*., 1994; De la Rosa and Yu, 2005). Two conceptual models about the heterogeneous biofilms existed (Lewandowshi and Beyenal, 2007; Wuertz *et al*., 2003). The first conceptual model of heterogeneous biofilms used microcolonies as the building blocks of biofilm. The second conceptual model of heterogeneous biofilms considered heterogeneous biofilm as a collection of layers of different densities and activities, in which the heterogeneous biofilm was called stratified biofilm. The conceptual model of stratified biofilm used discrete layers as the building blocks of biofilm and it became more popular in wastewater biofilms. According to the model of stratified biofilm, the overall activity of a heterogeneous biofilm was equal to the sum of the activities of the individual layers. This model of stratified biofilm was considered to have the capability to bridge the micro-scale and macro-scale measurement and contribute to solving the fundamental problems in biofilm engineering (Lewandowshi and Beyenal, 2007): quantitatively relating biofilm activity at the micro-scale to the performance of biofilm reactors at the macro-scale.

The stratification of conventional biofilms has been demonstrated (Yu, 2000). The active layer of conventional biofilms was generally considered to be present in the outer oxic region near the biofilm surface (bulk liquid – biofilm interface) (Casey *et al*., 1999). Yu and Bishop (1998) studied the stratification of

microbial metabolic processes and redox potential change in conventional wastewater biofilms. The results demonstrated that the aerobic oxidation took place only in a shallow layer near the biofilm surface, and the sulfate reduction occurred in the deeper anaerobic zone. A sharp decrease of redox potential from a positive potential to a negative potential was also discovered within a very narrow band of 50 μm near the interface between the aerobic zone and the sulfate reduction zone. Lydmark *et al*. (2006) studied vertical distribution of nitrifying populations in bacterial biofilms growing on a full-scale nitrifying trickling. Different vertical distribution patterns of *Nitrosomonas europaea* and N*itrosomonas communis* were shown: a smaller population of *Nitrosomonas europaea* was present only at the upper layer, while a population of *Nitrosomonas communis* increased with depth. In the stratified conventional biofilms, the ammonia-oxidizing zone was demonstrated to be located in the outer oxic regions (Okabe *et al*., 1999), and the sulfate-reducing zone was found in the inner anoxic regions (Okabe *et al*., 2003). These studies support the concept of stratification of the microbial metabolic processes in biofilms.

In a mushroom-shaped heterogeneous biofilm, concentration gradients in the water channels were considered to be quite different from those in the adjacent biofilm (de Beet *et al.*, 1994). In three-dimensional oxygen distribution maps using a microsensor and automation system, De la Rosa and Yu (2005) showed different degrees of the heterogeneity along the depth of wastewater biofilms (growing on a disk of a rotating biological reactor). This study demonstrated the depletion of oxygen at the biofilm surface and the presence of oxygen in deep

sections of biofilms, which indicated that oxic microniches could occur in the anoxic layer and anoxic microniches in the oxic layer.

Stewart (2003) introduced mathematic models used to calculate the diffusion of solutes in a heterogeneous biofilm. Penetration depth and the concentration of a metabolic product in the depths of a biofilm could be calculated using this model. Eberl et al. (2006) and Eberl (2003) described mathematic modeling in biofilm research.

2.2.3 Structure and activity in MABs

Studies of the internal structure and activity within the MABs could explain the pollutant removal behaviors and provide real-time concentration profiles of substrates and microbial processes to model builders. Due to the different diffusion mechanisms of gas and liquid substrates between MABs and conventional biofilms (Figure 1-1) (Nerenberg, 2005), the stratification of microbial processes within MABs should be different from that within conventional biofilms. Nevertheless, studies of conventional biofilms do provide help and guidance in developing experiments to better characterize MABs. The following two paragraphs review experimental and model studies on the structure and activity in MABs, respectively.

Up to now, most experimental studies on the structure and activity in MABs have focused on nitrification and denitrification in oxygen-based MABs. Cole *et al*. (2004) studied the stratification of activity and bacterial community structure within oxygen-based MABs, and demonstrated the highest respiratory activity occurred in the middle of the biofilms. In the same study, ammonia-

oxidizing bacteria (AOB) and denitrifying bacteria were found to coexist within a single piece of MAB under appropriate conditions. LaPara *et al*. (2006) studied the effects of organic carbon, ammonia-nitrogen, and oxygen partial pressure on the stratification of MABs. Nitrifying and denitrifying bacteria in this study were found not to grow simultaneously when organic concentrations became too high or ammonia concentrations became too low. Matsumoto *et al*. (2007) studied the community structure of nitrifying bacteria in a MAB. They demonstrated that the oxic part of the biofilm was dominated by AOB and nitrite oxidizing bacteria (*Nitrobacter sp*.). Another type of nitrite oxidizing bacteria, *Nitrospira sp.*, was abundant at the oxic-anoxic interface. In this study, the model prediction regarding AOB and *Nitrobacter sp.* distribution was consistent with the experimental counterpart. AOB cluster size distribution was measured in this study and showed that colonies are slightly larger adjacent to the membrane than at the inner part of the biofilm.

A pseudo-steady-state model focusing on a single-population MAB was built to predict substrate limitation regimes and the location of the active biomass layer (Casey *et al*., 2000b). The substrate limitation regimes include endogenous layer, growth layer and oxygen-depleted layer. This model shows the location of an active layer within the stratified MAB during its development. Gonzalez-Brambila *et al*. (2006) developed homogeneous and heterogeneous dynamic models to predict the performance of MAB for different modes of supplying oxygen to the biofilm. In this study, the heterogeneous model was proven to yield good prediction for the observed experimental results. Shanahan and Semmens (2004) described a model about multi-population MABs including aerobic

heterotrophs, nitrifiers, denitrifiers, and acetoclastic methanogens from the membrane surface to biofilm surface. In this study, the concentration profiles of multiple substrates were determined by diffusion and reaction using Monod kinetics. These results could demonstrate the microenvironments and microbial stratification in a MAB, and explain the ability of a MAB to simultaneously remove organic carbon and nitrogen. This model was promising, but it has not been validated by comparison to experimental data due to the limited quantity of data available on the MAB behaviors.

2.3 SRB and biological sulfate reduction

Sulfate can be found in domestic sewage and many industrial wastewaters e.g. from molasses fermentation, paper and pulp mills, citric acid plants and alcohol distilleries (Freese and Stuckey, 2004). In the treatment of sulfate-enriched wastewater, SRB are very important in the mineralization of organic matter, and it can compete with methanogens or denitrifying bacteria to utilize the organic matter as the electron donor. This study demonstrated SRB were predominant if the ratio of COD/SO_4^{2-} was 1~2 while methanogens were predominant if the ratio of COD/SO_4^{2-} was greater than 2. In an anaerobic continuous bioreactor running at 35 ℃, pH 7.8 and 2.5 days residence time, a high concentration of sulfate was demonstrated to be toxic for *Desulfobacterium* and *Desulfobulus* (Icgen and Harrison, 2006). In this study, the *Desulfococcus* group was found to be the most dominant group of SRB in the feed stream containing 15 kg m^{-3}sulfate (terminal electron acceptor) and 29.4 kg m^{-3}ethanol (carbon source and electron donor).

Although SRB could also utilize hydrogen as an electron donor to drive the reduction of sulfate (Terada *et al*., 2006a), sulfate reduction was not usually considered as a chemoautotrophic process. Sulfate reduction was generally considered as a chemoheterotrophic process because most SRB could obtain carbon from low-molecular-weight compounds, some aromatic compounds and longer chain fatty acids (Maier *et al*., 2000). Since relatively large amounts of sulfate were required for dissimilatory SRB, massive quantities of sulfide, the main end product of sulfate reduction, would be present in their immediate vicinity:

$$SO_4^{2-} \rightarrow SO_3^{2-} \rightarrow S_3O_6^{2-} \rightarrow S_2O_3^{2-} \rightarrow S^{2-}$$ (Barton, 1995) (Eq.2-1)

Taking methanol as an example, the overall reaction for the utilization of methanol is as follows (Maier *et al*., 2000):

$$4CH_3OH + 3SO_4^{2-} \longrightarrow 4CO_2 + 3S^{2-} + 8H_2O$$ (Eq.2-2)

The relative distribution of sulfide species, H_2S, HS^- and S^{2-} is dependent on the pH of the environment (Figure 2-1) (Sawyer *et al*., 2003). Figure 2-1 shows most of the sulfide will be present in the form of H_2S and HS^- if pH levels are between 5 and 9. The massive quantities of H_2S can be corrosive to concrete sewers, malodorous and toxic to humans (Sawyer *et al*., 2003).

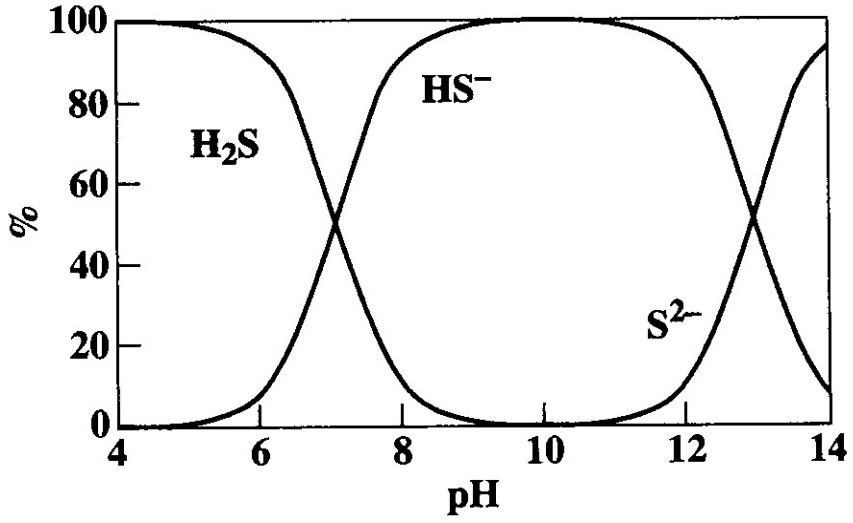

Figure 2-1 Effect of pH on relative distribution of sulfide species in water (a 10^{-3} molar solution)

The presence of H_2S is dependent on not only pH but also pE or the redox potential (pE=-log $\{e^-\}$). The pH-pE diagram for the S-O_2-H_2O system at total dissolved S concentration of 0.1 mol L^{-1} is shown in Figure 2-2 (Kehew, 2001). Figure 2-2 indicates that the predominant form of sulfur in most natural waters would be sulfate. Under extremely reduced conditions, H_2S and HS^- might be predominant. We will rarely encounter natural waters where S^{2-} is dominant. S is present only within a very narrow range of pE and pH in the natural waters.

There are several possible fates of H_2S and HS^-: 1) H_2S or HS^- could be taken up by chemoautotrophs or photoautotrophs and reoxidized by electron acceptors, such as oxygen or nitrate; 2) H_2S could volatilize; 3) H_2S or HS^- could react with metals to form metal sulfide.

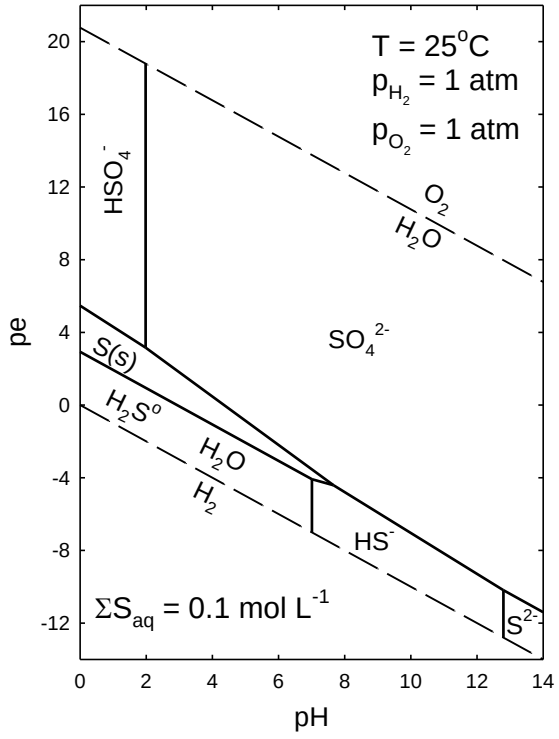

Figure 2-2 pE-pH diagram of sulfur species

Khanal and Huang (2003) studied the use of ORP as a reliable parameter to regulate the oxygen dosing for sulfide toxicity control during anaerobic treatment of high sulfate wastewater. The sulfide could react with heavy metals (De Lima *et al*., 2001; Beyenal and Lewandowski, 2004a; Beyenal *et al*., 2004b). A sulfate-reducing consortium dominated by *Desulfomicrobium norvegicum* was used to remove toxic metals and sulfide from the solution as insoluble sulfides (Boothman *et al*., 2006). Anaerobic sulfide oxidation with nitrate was also studied (Kamp *et al*., 2006). Okabe *et al*. (2002) demonstrated the addition of nitrite and nitrate forced sulfate reduction zones deeper in the agar gel and significantly reduced the *in situ* sulfide production levels. The *in situ* sulfide production

quickly recovered to the previous levels when nitrite and nitrate were removed. According to Okabe *et al.* (2002), the addition of nitrite and nitrate was found not to kill SRB but to induce the competition of nitrifying bacteria and SRB. It also enhanced the oxidation of produced sulfide in the agar gel.

Beyenal and Lewandowski (2001) studied the factors limiting H_2S production in a two-species biofilm containing SRB and non-SRB. The extent of biofilm heterogeneity was demonstrated to directly correlate with the flux of H_2S from cell clusters. At low flow velocities, H_2S production rate was limited by the delivery rate of sulfate ions to the biofilm. At higher flow velocities (> 2 cm s^{-1}), the H_2S production rate was limited by metabolic reactions in the biofilm.

Barton (1995) reported the effects of environmental factors such as pH, temperature, salts and oxygen on the growth of SRB. SRB grew better under slightly alkaline conditions over a relatively restricted pH range (7.0-7.8) and could tolerate pH values ranging from 5.5-9.0. The temperature dependence for sulfate reduction was variable. Mesophilic SRB grew best between 28 ℃ and 38 ℃, and the optimum growth temperature for thermophilic SRB ranged from 54 ℃ to 70 ℃. Most of the halophilic SRB isolated were marine or slightly halophilic microorganisms (with optimum salinity 1-4% NaCl). As for the effect of oxygen on the growth of SRB, this study demonstrated that SRB remained viable for hours or even days when exposed to molecular oxygen and several genera of SRB such as *Desulfovibrio, Desulfobulbus, Desulfobacterium* and *Desulfococcus* was detected to have the capabilities of aerobic respiration.

In recent years, SRB were increasingly perceived as microaerophiles, rather than obligate anaerobes (Barton, 1995). Okabe *et al*. (1999) demonstrated

the abundance of SRB, especially *Desulfobulbus spp.*, was higher in the oxic zone near the biofilm surface than in the neighboring anoxic zones in an aerobic mixed-population biofilm grown in a fully submerged rotating disk reactor, and their activity was sustained in the oxic zone of the surface of biofilm. A versatile metabolism of SRB with nitrate or oxygen as electron acceptor could help to explain the higher abundance of SRB in the oxic zone of the surface of biofilm, but it was also likely that SRB present in the surface of the biofilm originated from the wastewater instead of being developed in the biofilm.

Okabe *et al*. (2003) studied SRB community structure and their contribution to carbon mineralization in a wastewater biofilm growing under microaerophilic conditions. This study showed *Desulfobulbus spp.* was an important member of SRB populations and the main contributor to the oxidation of propionate to acetate in this biofilm. Microsensor measurements showed that a high sulfate-reducing activity was localized in a narrow zone located just below the oxic/anoxic interface when the biofilm was cultured in a synthetic medium and a broad sulfate-reducing zone was found in the entire anoxic strata when the biofilm was cultured in the supernatant of the primary settling tank effluent.

Previous studies on SRB and biological sulfate reduction mainly focused on conventional biofilms. The behavior of the sulfate reduction process in oxygen-based MABs is to be discovered and explored to expand the understanding of the structure and activity of MABs. This is one of the objectives of this dissertation.

2.4 Analytical methods for biofilm studies

Although the heterogeneity of biofilms and their complex function offered research opportunities in different fields, the analysis of a biofilm was a scientific challenge and required interdisciplinary cooperation. With the development of analytical tools in biofilm research, more and more information on the structure and activity of the biofilms were discovered. The methods for the biofilm activity and the biofilm components in water and wastewater treatment have been reviewed by Lazarova and Manem (1995). This review focused on the studies of conventional methods for biofilm characterization and activity analysis, such as the characterization of biofilm mass, biofilm density and total protein. The parameters measured by these methods are not sufficient to describe the *in situ* activity of biofilm at microscale. Moreover, the conventional approaches to the investigation of biofilm communities "don't allow exact determination of the localization of specific bacterial cells" and "pay little contribution to the understanding of actual microbial ecology" (Aoi, 2002).

In recent years, analytical methods have been developed towards the microscale and *in situ* measurement of bioflms (George *et al*. 2006). Moreover, the combination of several microscale and *in situ* measurements for the biofilm structure and activity has become more and more popular (Aoi, 2002). Denkhaus *et al*. (2007) summarized the approaches to biofilm analysis including microscopical, microbiological, molecular biological, chemical and physical methods with respect to their application in the biofilm research fields of interest.

This section will review the advanced methods for the *in situ* measurement of microbial activity and observation of biofilm structure at microscale:

microsensor techniques and microscopy techniques.

2.4.1 Microsensor techniques

Microsensor techniques have been used for biofilm research due to such advantages as the *in situ* measurements of microbial activities in microbial communities with minimal disturbance and high spatial and temporal resolution. They allow for *in situ* studies of intact biofilms.

Two types of microsensors have been used in the studies of microbial communities: electrochemical microsensors and fiberoptic microsensors. The electrochemical microsensors can be subdivided into potentiometric and amperometric microsensors. Revsbech (2005) summarized electrochemical microsenors used to analyze the microenvironment in terms of transport processes and micro-distribution of chemistry in microbial communities. Several chemical parameters such as O_2, H_2S, pH, NO_3^-, NH_4^+ and ORP, and physical parameters such as diffusivity in microbial communities have been measured using corresponding electrochemical microsenors. Kuhl and Jared (2005) reviewed the optical microsensors for the analysis of microbial communities. Diffusivity and flow, distribution of photosynthetic microbes and activity of oxygenic photosynthesis were measured by connecting fiberoptic microsensors to sensitive fluorometers. Steep gradients of light intensity and spectral composition were measured by connecting fiberoptic microsensors to sensitive light meters. In combination with microsensors for chemical species, the fiberoptic microsensors were used to analyze photosynthesis regulation and the photobiology of microbial phototrophs in intact samples.

The most important part of the microsensors is the sensing tip. The spatial resolution of the measurements is roughly equal to twice of the tip diameter of the sensor (Lewandowski and Beyenal, 2007). Different research areas might have different tip diameter requirement. For biofilm measurements, the principle of an acceptable tip size of the microsensor is that the tip is small enough not to damage biofilm structure and strong enough to survive moderate abuse by the operator. The technical difficulties in making fiberoptical microsensors with small tips inhibit their application in biofilm studies, although fiberoptic microsensors have some advantages over electrochemical sensors: freedom from electromagnetic interference, internal optical reference, compactness and geometric versatility. Currently, the majority of microsensors used in biofilm research are electrochemical microsensors. The electrochemical microsensors based on different working principles have their own advantages. For example, amperometric microsensors are believed to have better selectivity and longer lifetime while potentiometric microsensors are easier to make (Lewandowski and Beyenal, 2007).

Amperometric microsensors measure the current resulting from the electrode reactions, which was proportional to electroactive reactants' concentration. The equation of current and concentration of interest can be determined by Faraday's law and Fick's law (Lewandowski and Beyenal, 2007).

$$i = -nFAD\left(\frac{dC}{dx}\right) \qquad \text{(Eq.2-3)}$$

where i is steady-state limiting current; n is number of electrons involved in the reaction; F is Faraday constant ($C \cdot mol^{-1}$); A is the area of working electrode (cm^2);

D is diffusion coefficient in cm^2/s, dC/dx is bulk concentration gradient (mol/cm^4).

When the amperometric microsensor polarizes at over-potential voltage, the current (*i.e.*, limiting current) can be described by the following equation (Lewandowski and Beyenal, 2007):

$$i = -nFAD(\frac{C_{bulk}}{\delta}) \qquad \text{(Eq.2-4)}$$

where δ is thickness of diffusion layer. C_{bulk} is concentration of the analyte of interest in bulk solution. For a specific microelectrode, the terms "nFAD/δ" in equation 4 is constant and can be determined by a calibration process.

The amperometric microsensors have been applied for measurement of oxygen, H_2S, hydrogen peroxide concentrations and mass transport rates. Microbiosensors using biological material immobilized on sensing tips to modify the chemical signal are also based on the amperometric measurement principle. Examples of successfully miniaturized biosensors include glucose, methane, nitrate and nitrous oxide microsensors, but only glucose microsensors could be constructed with a small tip diameter (Lewandowski and Beyenal, 2007)..

Amperometric oxygen microsensor techniques have been developed to be the most mature and frequently used in biofilm research. Compared with separate cathode oxygen microsensor (working and reference electrode separated), the fabrication of combined amperometric oxygen microsensor (working, guard and reference electrode integrated in one body) is more sophisticated but the latter is less subject to interference, which would benefit the complex *in situ* measurement, especially the *in situ* measurement of biofilms (Lu and Yu 2002). Oxygen

microsensors have been widely used for one dimensional oxygen concentration profiles in the biofilms (Ramsing *et al*. 1993; Yu and Bishop 1998; Schulz and de Beer 2002) and could even be used for the three-dimensional oxygen mapping in biofilms due to its long lifetime and robustness (De la Rosa and Yu 2005). De La Rosa and Yu (2006) described the development of an automation system to measure the three-dimensional oxygen distribution in wastewater biofilms using the combined amperometric oxygen microsensors. The three-dimensional profile showed that the DO concentration in the biofilm sample was highly heterogeneous and it revealed "pockets" of dissolved oxygen in deep sections of the biofilm sample.

Amperometric microsensors without membrane have been used to characterize local mass transport with respect to local mass transport coefficient, local diffusivity and local flow velocity in biofilms. Horizontal distribution of local mass transport coefficient and local relative effective diffusivity in biofilms has been demonstrated by Lewandowski and Beyenal (2007).

Amperometric H_2S microsensors have been used for the studies of sulfate reduction and sulfur oxidation in microbial communities. Jeroschewski *et al*. (1996) first reported a combined amperometric H_2S microsensor (working, guard and reference electrode integrated in one body) for aquatic environments. This combined amperometric H_2S microsensor was used to study the activity of SRB in an acidic lake sediment (Kuhl *et al*., 1998) and sulfur-oxidizing bacteria in the microbial community on corroding concrete in sewer systems (Okabe *et al*., 2007).

The potentiometric microsensors measure membrane potential, which is frequently governed by the thermodynamic properties of the system and

determined as a function of specific ion concentration; usually, the electrode area, mass transfer, electrode geometry do not affect the potential directly (Bard and Faulkner, 2001). For a liquid ion-exchange (LIX) ion-selective microsensor, the membrane potential is composed of the potential drops across all interfaces in the system (shown in Eq.2-5).

$$E_{cell} = E_{int} - E_{ref} + E_{1-j} + E_{LIX} \qquad \text{(Eq.2-5)}$$

where E_{cell} is cell potential; E_{int} is the potential drop across the internal reference electrode; E_{ref} is potential drop across the external reference electrode; $E_{l\text{-}j}$ is the potential drop across the liquid junction; E_{LIX} is the potential drop across the ion-selective membrane.

E_{int} and E_{ref} are known and will not change because the internal solution in each reference electrode has a fixed composition. $E_{l\text{-}j}$ is constant if the bridge is properly designed. As a result, E_{LIX} is the only variable potential drop in a LIX microsensor system (Lewandowshi and Beyenal, 2007).

Ideally, the cell potential, E_{cell}, of a LIX microsensor system can be given by the Nernst equation (Eq.2-6):

$$E_{cell} = E_{LIX} = E_0 + \frac{2.303RT}{nF} log a_i \qquad \text{(Eq.2-6)}$$

where E_0 is reference potential; R is gas constant, T is absolute temperature; n is charge number of the measured ion in the sample solution; F is Faraday constant; a_i is the activity of the measured ion in the sample solution.

The potentiometric response of a LIX microsensor to concentrations of the ion of interest in the external solution can be determined experimentally. Therefore, the cell potential, i.e., potentiometric response of a LIX microsensor,

versus logarithms of the ionic concentrations in a series of standard solutions can be plotted as a straight-line calibration curve. Since the cell potential can be measured experimentally, the concentration of the ion of interest in the unknown sample solution can be read off from the calibration curve.

Ion-selective sulfide microsensors were first reported by Revsbech and Jorgensen (1986) and later used to study sulfate reduction and sulfide oxidation in biofilms (Kuhl and Jorgensen, 1992; Yu *et al*., 1998; Okabe *et al*., 1999). Lewandowski and Beyenal (2007) compared the ion-selective sulfide microsensor and combined amperometric H_2S microsensor to study the activity of SRB and sulfide oxidizing bacteria. They concluded that whenever there was a choice of using an amperometric or a potentiometric microsensor in a biofilm study, using the amperometric microsensor was advantageous.

In the studies of ion-selective pH microsensors, liquid ion-exchange (LIX) pH microsensor was preferentially used to measure the high spatial resolution in biofilms over the glass membrane pH microsensors (Santegoeds *et al*., 1998). An ORP microsensor, made of a platinum wire fused into a glass and then plated with gold at the tip, was developed and used in the biofilm studies (Yu and Bishop, 1998). Lee *et al*. (2006) described the fabrication of microsensor arrays with four-probe glass electrodes for *in situ* ORP measurement in environment samples such as biofilms. The tip diameter of individual microsensors was approximately 200 nm. The microsensor arrays exhibited a very fast response time (from a few milliseconds to 30 second) and proved to be extraordinarily stable (variability on the order of 2 mV over a 4-day test period). LIX-type ammonia, nitrite and nitrate were used for the activities of nitrifying and

denitrifying bacteria in biofilms treating industrial wastewater (Satoh *et al*., 2006) and MABs growing in synthetic wastewater (Satoh *et al*., 2004).

2.4.2 Microscopy techniques

Microscopic techniques, such as scanning electron microscopy (SEM) and confocal laser scanning microscopy (CLSM), have been used to observe the biofilm structure (Lee *et al*., 2007; Ivnitsky *et al*., 2007; Pang and Liu, 2007). There are a few reviews on microscopic methods (Caldwell *et al*., 1992; Costerton *et al*., 1994). Wolf *et al*. (2002) reviewed microscopic methods such as SEM and CLSM for biofilm examination and monitoring. The advantages and disadvantages of these methods or techniques were summarized in this review. Lawrence and Neu (2004) reviewed the selected studies illustrating the application of the microscale approach and laser microscopy techniques in river biofilms.

SEM can be used to examine the surface topology of biofilms by imaging microorganisms deposited on surfaces at high magnification. As a traditional method used in biofilm research, it has been of special importance in elucidating biofilm structure in spite of its drawbacks: fixation and dehydration procedures in sample preparation may cause biofilm shrinkage and damage (Eighmy *et al*., 1983; Wolf *et al*., 2002).

Fowler and Robertson (1991) used SEM to study the hydraulic residence time of immobilized cells. Rothemund *et al*. (1994) reported the combined use of SEM, microsensors and oligonucleotide probes for structure-function studies and *in situ* identification of microorganisms on membrane-bound biofilms. Jass *et al*.

(1995) employed SEM, in combination with epifluorescence microscopy, for monitoring the formation of *Pseudomonas fluorescens* and *Pseudomonas putida* biofilms on silastic rubber in a modified Robbins device. *P. putida* were found to adhere as single cells or microcolonies, whereas *P. fluorescens* formed confluent and dense biofilms.

CLSM can examine non-destructively successive focal planes of living, and hydrated biofilms (Denkhaus *et al*., 2007). In addition, it can control the depth of field and eliminate the out-of-focus image-degrading objects in the field of review (Lewandowski and Beyenal, 2007). However, CLSM has some drawbacks, such as the slow scanning action of the laser for high quality images and the autofluorescence of samples may overlap that of fluorescence probes. CLSM is also not suitable for the analysis of very thick and opaque biofilms. Nevertheless, the CLSM could be used for the systematic study of very different biofilms.

CLSM has played a significant role for the characterization of biofilm structure. It can provide *in situ* information about the three-dimensional depiction of the biofilm. The CLSM has been used to verify that the biofilm structure is quite heterogeneous (Costerton *et al*., 1994). Rodriguez and Bishop (2007) used CLSM images to analyze the three-dimensional structure of soil biofilms. In this study, a heterogeneous soil biofilm was observed with a large variety of biological aggregate structures and growth patterns, including cluster-and-protusion type structures, cell aggregate bridging and a thick bioweb-type growth. The values of cell diameter, biovolume, biosurface area and biothickness were also obtained by the CLSM images in the same study. Merod *et al*. (2007) created a novel program Auto PHLIP-ML to automatically determine the three-dimensional biofilm

structure using CLSM images. Lee *et al*. (2007) and Ivnitsky *et al*. (2007) investigated the change of structure and microbial communities of biofilms growing on membrane surface under various operating conditions using CLSM and image analysis techniques.

In combination with microsensors, microscopy techniques can provide more information on biofilm structure and activity. The application of microscopy in combination with microsensors enables the studies of the relationship between biofilm structure and different physical and chemical parameters in biofilms. Using CLSM, oxygen microsensor and fluorescent chemical probes, Costerton *et al*. (1994) developed a mushroom-shaped structure of heterogeneous biofilms and demonstrated the coexistence of different microenvironments, such as aerobic and anaerobic environments in a single biofilm. Using CLSM and microsensors, local diffusion coefficients and mass transfer phenomena in biofilms were also examined (de Beer *et al*., 1994; de Beer and Stoodley 1995; Lewandowski and Beyenal, 2007). The diffusivity in cell cluster was demonstrated to be much higher than that in void, indicating that the substances, such as carbon substrates, nutrients and oxygen, easily transported in voids but not easily penetrated into bacterial cell clusters (de Beer *et al*., 1997). Mass transport limitations in biofilms were found to be not only dependent on biofilm thickness but also on biofilm structure with regard to biofilm porosity and biofilm density (de Beer *et al*., 1994).

References

Aoi, Y. 2002. *In situ* Identification of microorganisms in biofilm communities.

Journal of Bioscience and Bioengineering 94(6): 552–556.

Aoi, Y., Shiramasa, Y., Kakimoto, E., Tsuneda, S., Hirata, A. and Nagamune, T. 2005. Single-stage autotrophic nitrogen-removal process using a composite matrix immobilizing nitrifying and sulfur-denitrifying bacteria. Applied Microbiology and Biotechnology 68(1): 124-130.

Bard, A. J. and Faulkner, L. R. 2001. Electrochemical methods - fundamentals and applications.

Barton, L. L. 1995. Sulfate-reducing bacteria. New Jork: Plenum press

Beyenal, H. and Lewandowski, Z. 2001. Mass-transport dynamics, activity, and structure of sulfate-reducing biofilms. Aiche Journal 47(7): 1689-1697.

Beyenal, H. and Lewandowski, Z. 2004a. Dynamics of lead immobilization in sulfate reducing biofilms. Water Research 38(11): 2726-2736.

Beyenal, H., Sani, R. K., Peyton, B. M., Dohnalkova, A. C., Amonette, J. E. and Lewandowski, Z. 2004b. Uranium immobilization by sulfate-reducing biofilms. Environmental Science & Technology 38(7): 2067-2074.

Bishop, P. L. 2003. The effect of biofilm heterogeneity on metabolic processes. In W. S., B. P. and P.Wilderer (Eds.). Biofilms in Wastewater Treatment: An Interdisciplinary Approach. London, IWA Publishing: 125-142.

Boothman, C., Hockin, S., Holmes, D. E., Gadd, G. M. and Lloyd, J. R. 2006. Molecular analysis of a sulphate-reducing consortium used to treat metal-containing effluents. Biometals 19(6): 601-609.

Caldwell, D. E., Korber, D. R. and Lawrence, J. R. 1992. Confocal laser microscopy and digital image-analysis in microbial ecology. Advances in Microbial Ecology. 12: 1-67.

Cao, T., Tang, H., Liang, X., Wang, A., Auner, G. W., Salley, S. O. and Ng, K. Y. S. 2006. Nanoscale investigation on adhesion of E. coli to surface modified silicone using atomic force microscopy. Biotechnology and Bioengineering. 94(1): 167.

Casey, E., Glennon, B. and Hamer, G. 1999. Review of membrane aerated biofilm reactors. Resources Conservation and Recycling 27(1-2): 203-215.

Casey, E., Glennon, B. and Hamer, G. 2000a. Biofilm development in a membrane-aerated biofilm reactor: Effect of flow velocity on performance. Biotechnology and Bioengineering 67(4): 476-486.

Casey, E., Glennon, B. and Hamer, G. 2000b. Biofilm development in a membrane-aerated biofilm reactor: effect of intra-membrane oxygen pressure on performance. Bioprocess Engineering 23(5): 457-465.

Charcklis, W. G. and Marshall, K. C. 1990. biofilms. New York: Wiley-Interscience

Chung, J., Nerenberg, R. and Rittmann, B. E. 2006. Bioreduction of selenate using a hydrogen-based membrane biofilm reactor. Environmental Science & Technology 40(5): 1664-1671.

Clapp, L. W., Regan, J. M., Ali, F., Newman, J. D., Park, J. K. and Noguera, D. R. 1999. Activity, structure, and stratification of membrane-attached methanotrophic biofilms cometabolically degrading trichloroethylene. Water Science and Technology 39(7): 153-161.

Cole, A. C. 2005. Characterization of membrane aerated biofilms for wasterwater treatment, Univeristy of Minnesota. Doctor of Philosophy.

Cole, A. C., Semmens, M. J. and LaPara, T. M. 2004. Stratification of activity and bacterial community structure in biofilms grown on membranes transferring oxygen. Applied and Environmental Microbiology 70(4): 1982-1989.

Costerton, J. W., Lewandowski, Z., De beer, D., Caldwell, D., Korber, D. and James, G. 1994. Biofilms, the customized microniche. Journal of Bacteriology. 176(8): 2137-2142.

Cote, P., Bersillon, J. L., Huyard, A. and Faup, G. 1988. Bubble-free Aeration Using Membrane-Process Analysis. Journal Water Pollution Control Federation 60(11): 1986-1992.

de Beer, D. and Stoodley, P. 1995. Relation between the structure of an aerobic biofilm and transport phenomena. Water Science and Technology. 32(8): 11-18.

de Beer, D., Stoodley, P. and Lewandowski, Z. 1997. Measurement of local diffusion coefficients in biofilms by microinjection and confocal microscopy. Biotechnology and Bioengineering. 53(2): 151-158.

de Beer, D., Stoodley, P., Roe, F. and Lewandowski, Z. 1994. Effects of biofilm structures on oxygen distribution and mass transport. Biotechnology and Bioengineering. 43(11): 1131-1138.

De la Rosa, C. and Yu, T. 2005. Three-dimensional mapping of oxygen distribution in wastewater biofilms using an automation system and microsensors. Environmental Science & Technology 39(14): 5196-5202.

De La Rosa, C. and Yu, T. 2006. Development of an automation system to evaluate the three-dimensional oxygen distribution in wastewater biofilms using microsensors. Sensors and Actuators, B: Chemical. 113(1): 47.

De Lima, A. C. F., Goncalves, M. M. M., Granato, M. and Leite, S. G. F. 2001. Anaerobic sulphate-reducing microbial process using UASB reactor for heavy metals decontamination. Environmental Technology 22(3): 261-270.

Denkhaus, E., Meisen, S., Telgheder, U. and Wingender, J. 2007. Chemical and physical methods for characterisation of biofilms. Microchimica Acta 158(1-2): 1-27.

Eberl, H., Morgenroth, E., Noguera, D., Picioreanu, C., Rittmann, B., Loosdrecht, M. v. and Wanner, O. 2006. Mathematical Modeling of Biofilms. London: IWA Publishing.

Eberl, H. J. 2003. What do biofilmss models., mechanical ducks, and artificial life have in common? Mathematical modeling in biofilm research. In W. S., B. P. and P.Wilderer (Eds.). Biofilms in Wastewater Treatment: An Interdisciplinary Approach London, IWA Publishing: 8-28.

Eighmy, T. T., Maratea, D. and Bishop P. L. 1983. Electron microscopic examination of wastewater biofilm formation and structuralcomponents. Appl Environ Microbiol 45(6): 1921–1931

Esterl, S., Hartmann, C. and Delgado, A. 2003. On the influence of fluid flow in a packed-bed biofilm reactor. In S. Wuertz, P. Bishop and P.Wilderer (Eds.). Biofilms in Wasterwater Treatment: An interdisciplinary Approach. London, IWA Publishing: 88-114.

Fowler, J.D. and Robertson, C.R. 1991. Hydraulic permeability of immobilized bacterial-cell aggregates. Applied and Environmental Microbiology. 57 (1): 102-113

Freese, L. H. and Stuckey, D. C. 2004. Anaerobic treatment of sulphate-enriched wastewaters. Proceedings of the Institution of Civil Engineers-Water Management 157(4): 187-195.

Fry, N., Raskin, l., Sharp, R., Alm, E., Mobarry, B. and Satahl, D. 1997. *In situ* ananlyses of microbial populations with molecular probes. In S. J. and D. M. (Eds.). Bacteria as Multicellular Organisms. New York, Oxford University Press: 292-336.

George, R. P., Muraleedharan, P., Dayal, R. K. and Khatak, H. S. 2006. Techniques for biofilm monitoring. 24(1-2): 123-150.

Gonzalez-Brambila, M., Monroy, O. and Lopez-Isunza, F. 2006. Experimental and theoretical study of membrane-aerated biofilm reactor behavior under different modes of oxygen supply for the treatment of synthetic wastewater. Chemical Engineering Science 61(16): 5268-5281.

Hibiya, K., Terada, A., Tsuneda, S. and Hirata, A. 2003. Simultaneous nitrification and denitrification by controlling vertical and horizontal microenvironment in a membrane-aerated biofilm reactor. Journal of Biotechnology 100(1): 23-32.

Ivnitsky, H., Katz, I., Minz, D., Volvovic, G., Shimoni, E., Kesselman, E., Semiat, R. and Dosoretz, C. G. 2007. Bacterial community composition and structure of biofilms developing on nanofiltration membranes applied to wastewater treatment. Water Research. 41(17): 3924-3935.

Jang, A., Bishop, P. L., Okabe, S., Lee, S. G. and Kim, I. S. 2003. Effect of dissolved oxygen concentration on the biofilm and *in situ* analysis by fluorescence *in situ* hybridization (FISH) and microelectrodes. Water Science and Technology. 47(1): 49-57.

Jang, A., Yoon, Y. H., Kim, I. S., Kim, K. S. and Bishop, P. L. 2003. Characterization and evaluation of aerobic granules in sequencing batch reactor. Journal of Biotechnology 105(1-2): 71-82.

Jass, J., Costerton, J.W., Lappinscott, H.M. 1995. Assessment of a chemostat-coupled modified robbins device to study biofilms. Journal of Industrial Microbiology. 15 (4): 283-289

Jeroschewski, P., Steuckart, C. and Kuhl, M. 1996. An amperometric microsensor for the determination of H2S in aquatic environments. Analytical Chemistry 68(24): 4351-4357.

Kamp, A., Stief, P. and Schulz-Vogt, H. N. 2006. Anaerobic sulfide oxidation with nitrate by a freshwater Beggiatoa enrichment culture. Applied and Environmental Microbiology 72(7): 4755-4760.

Kappell, A. S., Semmens, M. J., Novak, P. J. and LaPara, T. M. 2005. Novel application of oxygen-transferring membranes to improve anaerobic wastewater treatment. Biotechnology and Bioengineering 89(4): 373-380.

Kehew. 2001. The geochemistry of Natural waters: Redox reactions and processes – II. Retrieved by June 2012. http://www.sci.uidaho.edu/geol464_564/Powerpoint/Lecture_9_468_568nc.pdf

Khanal, S. K. and Huang, J. C. 2003. Anaerobic treatment of high sulfate wastewater with oxygenation to control sulfide toxicity. Journal of Environmental Engineering-Asce 129(12): 1104-1111.

Kuhl, M. and Jared, R. L. 2005. Optical Microsensors for Analysis of Microbial Communities. In (Eds.). Methods in Enzymology. Academic Press. Volume 397: 166.

Kuhl, M. and Jorgensen, B. B. 1992. Microsensor measurements of sulfate reduction and sulfide oxidation in compact microbial communities of aerobic biofilms. Applied and Environmental Microbiology 58(4): 1164-1174.

Kuhl, M., Steuckart, C., Eickert, G. and Jeroschewski, P. 1998. A H_2S microsensor for profiling biofilms and sediments: application in an acidic lake sediment. Aquatic Microbial Ecology 15(2): 201-209.

LaPara, T. M., Cole, A. C., Shanahan, J. W. and Semmens, M. J. 2006. The effects of organic carbon, ammoniacal-nitrogen, and oxygen partial pressure on the stratification of membrane-aerated biofilms. Journal of Industrial Microbiology & Biotechnology 33(4): 315-323.

Lawrence, J. R. and Neu, T. R. 2004. Microscale Analyses of the formation and nature of microbial biofilm communities in river systems. Reviews in Environmental Science and Biotechnology. 2: 85-97.

Lazarova, V. and Manem, J. 1995. Biofilm characterization and activity analysis in water and waste-water treatment. Water Research. 29(10): 2227-2245.

Lee, J. H., Jang, A., Bhadri, P. R., Myers, R. R., Timmons, W., Beyette, F. R., Bishop, P. L. and Papautsky, I. 2006. Fabrication of microsensor arrays for

in situ sensing of oxidation reduction potentials. Sensors and Actuators B-Chemical 115(1): 220-226.

Lee, W. N., Chang, I. S., Hwang, B. K., Park, P. K., Lee, C. H. and Huang, X. 2007. Changes in biofilm-architecture with addition of membrane fouling reducer in a membrane bioreactor. Process Biochemistry. 42(4): 655-661.

Lewandowski, Z. and Beyenal, H. 2007. Fundamentals of biofilm research. Boca Raton: CRC Press

Lu, R. and Yu, T. 2002. Fabrication and evaluation of an oxygen microsensor applicable to environmental engineering and science. J. Environ. Eng. Sci. (1): 225-235.

Lydmark, P., Lind, M., Sorensson, F. and Hermansson, M. 2006. Vertical distribution of nitrifying populations in bacterial biofilms from a full-scale nitrifying trickling filter. Environmental Microbiology 8(11): 2036-2049.

Maier, R. M., Pepper, I. L. and Gerba, C. P. 2000. Environmental Microbiology. Academic Press

Matsumoto, S., Terada, A., Aoi, Y., Tsuneda, S., Alpkvist, E., Picioreanu, C. and Loosdrecht, M. C. M. v. 2007. Experimental and simulation analysis of community structure of nitrifying bacteria in a membrane-aerated biofilm. Water Science & Technology 55(8-9): 283-290.

Merod, R. T., Warren, J. E., McCaslin, H. and Wuertz, S. 2007. Toward automated analysis of biofilm architecture: Bias caused by extraneous confocal laser scanning microscopy images. Applied and Environmental Microbiology. 73(15): 4922-4930.

Morgenroth, E. 2003. Detachment: an often-overlooked phenomenon in biofilm research and modeling. In W. S., B. P. and P.Wilderer (Eds.). Biofilms in Wasterwater Treatment: An interdscilinary Approach. London, IWA Publishing: 264-288.

Motlagh, A. R. A., Voller, V. R. and Semmens, M. J. 2006. Advective flow through membrane-aerated biofilms - Modeling results. Journal of Membrane Science 273(1-2): 143-151.

Nerenberg, R. 2005. Membrane biofilm reactors for water and wastewater treatment. A Seminar on Advances in Water And Wastewater Treatment, Borchardt.

Ohandja, D. G. and Stuckey, D. C. 2007. Biodegradation of PCE in a hybrid membrane aerated biofilm reactor. Journal of Environmental Engineering-Asce 133(1): 20-27.

Okabe, S., Odagiri, M., Ito, T. and Satoh, H. 2007. Succession of sulfur-oxidizing bacteria in the microbial community on corroding concrete in sewer systems. Applied and Environmental Microbiology 73(3): 971-980.

Okabe, S., Santegoeds, C. M., Watanabe, Y. and de Beer, D. 2002. Successional development of sulfate-reducing bacterial populations and their activities in an activated sludge immobilized agar gel film. Biotechnology and Bioengineering 78(2): 119-130.

Okabe, S., Satoh, H. and Watanabe, Y. 1999. *In situ* analysis of nitrifying biofilms as determined by *in situ* hybridization and the use of microsensors. Applied and Environmental Microbiology 65(7): 3182-3191.

Okabe, S., Ito, T. and Satoh, H. 2003. Sulfate-reducing bacterial community structure and their contribution to carbon mineralization in a wastewater biofilm growing under microaerophilic conditions. Applied Microbiology and Biotechnology 63(3): 322-334.

Okabe, S., Ito, T., Sugita, K. and Satoh, H. 2005. Succession of internal sulfur cycles and sulfur-oxidizing bacterial communities in microaerophilic wastewater biofilms. Applied and Environmental Microbiology 71(5): 2520-2529.

Pang, C. M. and Liu, W. T. 2007. Community structure analysis of reverse osmosis membrane biofilms and the significance of Rhizobiales bacteria in biofouling. Environmental Science & Technology. 41(13): 4728-4734.

Pankhania, M., Brindle, K. and Stephenson, T. 1999. Membrane aeration bioreactors for wastewater treatment: completely mixed and plug-flow operation. Chemical Engineering Journal 73(2): 131-136.

Ramsing, N. B., Kuhl, M. and Jorgensen, B. B. 1993. Distribution of Sulfate-Reducing Bacteria, O_2, and H_2S in Photosynthetic Biofilms Determined by Oligonucleotide Probes and Microsensors. Applied and Environmental Microbiology 59(11): 3840-3849.

Revsbech, N. P. 2005. Analysis of microbial communities with electrochemical microsensors and microscale biosensors. Environmental Microbiology. 397: 147-166.

Revsbech, N. P. and Jorgensen, B. B. 1986. Microsensors - their use in microbial ecology. Advances in Microbial Ecology 9: 293-352.

Rishell, S., Casey, E., Glennon, B. and Hamer, G. 2004. Characteristics of a methanotrophic culture in a membrane-aerated biofilm reactor. Biotechnology Progress 20(4): 1082-1090.

Rodriguez, S. J. and Bishop, P. L. 2007. Three-dimensional quantification of soil biofilms using image analysis. Environmental Engineering Science. 24(1): 96-103.

Rothemund, C., Camper, A., Wilderer, P. 1994. Biofilms growing on gas-permeable membranes. Water Science and Technology. 29 (10-11): 447-454

Santegoeds, C. M., Schramm, A. and de Beer, D. 1998. Microsensors as a tool to determine chemical microgradients and bacterial activity in wastewater biofilms and flocs. Biodegradation 9(3-4): 159-167.

Satoh, H., Ono, H., Rulin, B., Kamo, J., Okabe, S. and Fukushi, K. I. 2004. Macroscale and microscale analyses of nitrification and denitrification in biofilms attached on membrane aerated biofilm reactors. Water Research 38(6): 1633-1641.

Satoh, H., Yamakawa, T., Kindaichi, T., Ito, T. and Okabe, S. 2006. Community structures and activities of nitrifying and denitrifying bacteria in industrial wastewater-treating biofilms. Biotechnology and Bioengineering 94(4): 762-772.

Sawyer, C. N., Mccarty, P. L. and Parkin, G. F. 2003. Chemistry for Environmental Engineering and Science. McGraw-Hil Companies, Inc

Schulz, H. N. and de Beer, D. 2002. Uptake rates of oxygen and sulfide measured with individual Thiomargarita namibiensis cells by using microsensors.

Applied and Environmental Microbiology 68(11): 5746-5749.

Shanahan, J. W., Cole, A. C., Semmens, M. I. and LaPara, T. M. 2005. Acetate and ammonium diffusivity in membrane-aerated biofilms: improving model predictions using experimental results. Water Science and Technology 52(7): 121-126.

Shanahan, J. W. and Semmens, M. I. 2004. Multipopulation model of membrane-aerated biofilms. Environmental Science & Technology 38(11): 3176-3183.

Silva, A. J., Hirasawa, J. S., Varesche, M. B., Foresti, E. and Zaiat, M. 2006. Evaluation of support materials for the immobilization of sulfate-reducing bacteria and methanogenic archaea. Anaerobe 12(2): 93-98.

Stewart, P. S. 2003. Diffusion in biofilms. Journal of Bacteriology 185(5): 1485-1491.

Terada, A., Hibiya, K., Nagai, J., Tsuneda, S. and Hirata, A. 2003. Nitrogen removal characteristics and biofilm analysis of a membrane-aerated biofilm reactor applicable to high-strength nitrogenous wastewater treatment. Journal of Bioscience and Bioengineering 95(2): 170-178.

Terada, A., Kaku, S., Matsumoto, S. and Tsuneda, S. 2006a. Rapid autohydrogenotrophic denitrification by a membrane biofilm reactor equipped with a fibrous support around a gas-permeable membrane. Biochemical Engineering Journal 31(1): 84-91.

Terada, A., Yamamoto, T., Tsuneda, S. and Hirata, A. 2006b. Sequencing batch membrane biofilm reactor for simultaneous nitrogen and phosphorus

removal: Novel application of membrane-aerated biofilm. Biotechnology and Bioengineering 94(4): 730-739.

Wang, S. (2005). Study on Carbon and Nitrogen Removal by Membrane Aerated Bioreactor, Tsinghua University. Msc.

Wolf, G., Crespo, J. G. and Reis, M. A. M. 2002. Optical and spectroscopic methods for biofilm examination and monitoring Reviews in Environmental Science and Biotechnology. 1: 227.

Wu, C. Y., Ushiwaka, S., Horli, H. and Yamagiwa, K. 2006. Boosting nitrification by membrane-attached biofilm. Water Science and Technology 54(9): 121-128.

Wuertz, S. and Falkentoft C.M. 2003. Modeling and simulation: introduction. In Wuertz, S., Bishop, P. and Wilderer, P. (Eds.). Biofilms in wastewater treatment: an interdisplinary approach. London: IWA publishing, Alliance House.

Wuertz, S., Bishop, P. and Wilderer, P. 2003. Biofilms in wastewater treatment: an interdisplinary approach. London: IWA publishing, Alliance House.

Xiaoxia, S., Peng, T. Y. and Olavi, P. S. 2006. Direct force measurement of bacteria adhesion on metal in aqueous media. Water Sci Technol. 54(9): 17-25.

Yu, T. 2000. Stratification of microbial process and redox potential changes in biofilm. University of Cincinnati. Doctor of Philosophy theses

Yu, T. and Bishop, P. L. 1998. Stratification of microbial metabolic processes and redox potential change in an aerobic biofilm studied using microelectrodes. Water Science and Technology. 37(4-5): 195-198.

Yu, T., Bishop, P. L., Galal, A. and Mark, H. B. 1998. Fabrication and evaluation of a sulfide microelectrode for biofilm studies. In Akmal, N., Usmani, A.M. (Eds.). Polymers in Sensors: Theory and practice. Washington D.C.: Oxford University Press. 231-247

Chapter 3

Materials and Methods

In this research, MABR 1 and MABR 2 were designed and operated for almost one year. Six types of microsensors were fabricated and applied in the measurements of MABs. This chapter introduces the design and operational conditions of MABRs, chemical analyses for influent and effluent water, fabrication and calibration of microsensors, set-up for microsensor measurements and SEM observation for the MABs.

3.1 Biofilm reactors-MABRs

3.1.1 Membranes and membrane modules

Four types of gas permeable membranes were used in this study: hollow fiber microporous membrane (pore size: 0.1 μm, Inner Diameter (ID)/Outside Diameter (OD): 0.6/1.3 mm, polyvinylidene fluoride; Pall Corporation, USA), silicone tubing dense membrane (ID/OD: 3.5/4.3 mm, silicone; Dow Corning, Canada), flat sheet microporous membrane (pore size: 0.12×0.04 μm, 25 μm thick, polypropylene; Celgard, NC, USA) and flat sheet dense membrane (76.2 μm thick, silicone; Specialty Silicone Products, USA). Two membrane modules, consisting of hollow fiber microporous membrane and silicone tubing dense membrane, respectively, were fabricated with similar procedures. In the hollow fiber microporous membrane module, a few microporous hollow fibers were arranged in parallel and inserted into a tube. The connections between the hollow fibers and

tube were glued using epoxy. In the silicone tubing membrane module, a few silicone tubing membranes were arranged in parallel and inserted into a tube. The connections between the silicone tubing membranes and tube were glued using epoxy.

3.1.2 Biofilm reactors

Two biofilm reactors, MABRs, were designed, fabricated, and operated under well-defined operational conditions. Figure 3-1 shows the schematic diagram of the MABR 1, which contains a hollow fiber microporous membrane module and a silicone tubing membrane module.

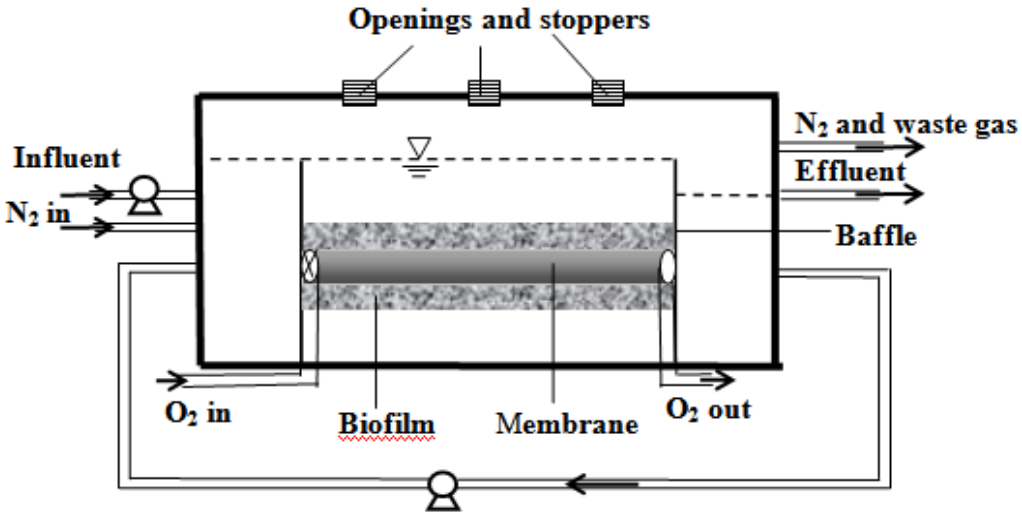

Figure 3-1 Schematic diagram of MABR 1

Figure 3-2 shows the schematic diagram of the MABR 2, which contains flat sheet microporous membrane and flat sheet dense silicone membrane. MABs were grown on the hollow fiber microporous membranes and silicone tubing dense membranes in MABR 1, as well as the flat sheet microporous membrane

and flat sheet dense silicone membrane in MABR 2. Both reactors were rectangular and tightly closed flow cells. They were constructed using acrylic plastics. The top of the two reactors had openings for operational view and *in situ* measurements. During normal operation, the openings were tightly closed using rubber stoppers.

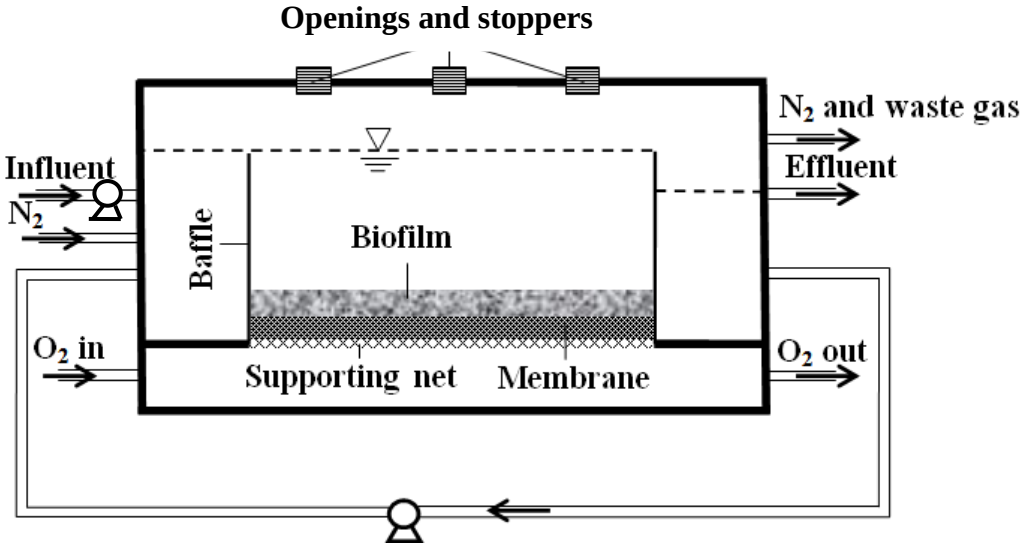

Figure 3-2 Schematic diagram of MABR 2

MABR 1 consisted of two acrylic plastic sections bolted together. The bottom section had a rectangular liquid chamber (cavity size: 25 cm long × 10 cm wide × 5.3 cm deep). Two membrane modules, containing the hollow fiber microporous membrane sheet (16 cm long × 4 cm wide) and the silicone tubing dense sheet (16 cm long × 4 cm wide), respectively, were fixed horizontally onto the bottom section of the reactor, attaching onto a baffle each side. The top section (25 cm long × 10 cm wide × 1 cm thick), or the lid, with six openings in, was air-tightly sealed with the bottom section using a silicone gasket. The effective volume of the reactor was 1.2 L. Oxygen was supplied from a cylinder

(Cat.# OX 2.6-T, Praxair, Canada). The oxygen pressure was controlled at 50 kPa by a regulator (Cat.# PRX 312-1331-540, Praxair, Canada). Oxygen flowed separately through the hollow fiber membrane module and silicone tubing membrane module at the same flow rate, which was controlled by a flow meter (Ser. #: 066619, Cole Parmer, Canada). Nitrogen gas was supplied from a cylinder (Cat.# NI 4.8-T, Praxair, Canada). The nitrogen pressure was controlled at 50 kPa by a regulator (Cat.# PRX 312-1331-580, Praxair, Canada). Nitrogen was purged into the influent of synthetic wastewater to ensure the synthetic wastewater was oxygen-free, and that the oxygen gas in the bulk liquid of reactor came from membrane side not from synthetic wastewater. The flow rate of nitrogen was controlled by a flow meter (Ser. #: 066620, Cole Parmer, Canada). The above flow meters for oxygen and nitrogen were calibrated using a wet test meter. Synthetic wastewater was pumped into the reactor using a pumping system (pump head: Model #: 7013-20; pump driver: Model #: 7553-80, Cole Parmer, Canada), and was recycled using another pumping system (pump head: Model #: 7017-20; pump driver: Model #: 7553-70, Cole Parmer, Canada). The influent and recycle rate of the synthetic wastewater were controlled by a speed controller (Masterflex, Cole Parmer, Canada). Figure 3-3 shows a photographic illustration of MABR 1.

Figure 3-3 Photographic illustration of MABR 1

MABR 2 consisted of three acrylic plastic sections bolted together. The upper section had a rectangular liquid chamber (cavity size: 30 cm long × 9 cm wide × 3.5 cm deep) with six openings at the top. The lower section contained two gas channels, each of which was 30 cm long, 3 cm wide and 1.0 cm deep. The middle section, supporting board, had two cavities, each of which was 30 cm long × 3 cm wide × 0.5 cm deep. The flat sheet microporous membrane and flat sheet dense membrane were placed on the supporting material in each gas channel, respectively. While assembling the reactor, silicone gaskets were placed between two pieces to provide an air-tight seal. The working liquid volume of the reactor was 1.1 L. Oxygen was supplied from a cylinder (Cat.# OX 2.6-T, Praxair, Canada) and the oxygen pressure was controlled at 50 kPa by a regulator (Cat.# PRX 312-1331-540, Praxair, Canada). Oxygen flowed separately through the flat sheet microporous membrane and flat sheet silicone membrane at the same flow

rate over each gas channels, which was controlled by a flow meter (Ser. # 066619, Cole Parmer). Nitrogen gas was supplied from a cylinder (Cat.# NI 4.8-T, Praxair, Canada), and the pressure was controlled at 50 kPa by a regulator (Cat.# PRX 312-1331-580, Praxair, Canada). Nitrogen was purged into the influent of synthetic wastewater to ensure the synthetic wastewater was oxygen-free, and that the oxygen gas in the bulk liquid of the reactor came from the membrane side not from synthetic wastewater. The flow rate of nitrogen was controlled by a flow meter (Ser. # 066620, Cole Parmer). The flow meters were calibrated using Wet Test Meter. Synthetic wastewater was pumped into the upper section of the reactor using pumping system (pump head: Model #: 7013-20; pump driver: Model #: 7553-80, Cole Parmer, Canada), and it was recycled using another pumping system (pump head: Model #: 7017-20; pump driver: Model #: 7553-70, Cole Parmer, Canada). The influent and recycle rate of the synthetic wastewater were controlled by a speed controller (Masterflex, Cole Parmer, Canada). Figure 3-4 shows the photographic illustration of MABR 2.

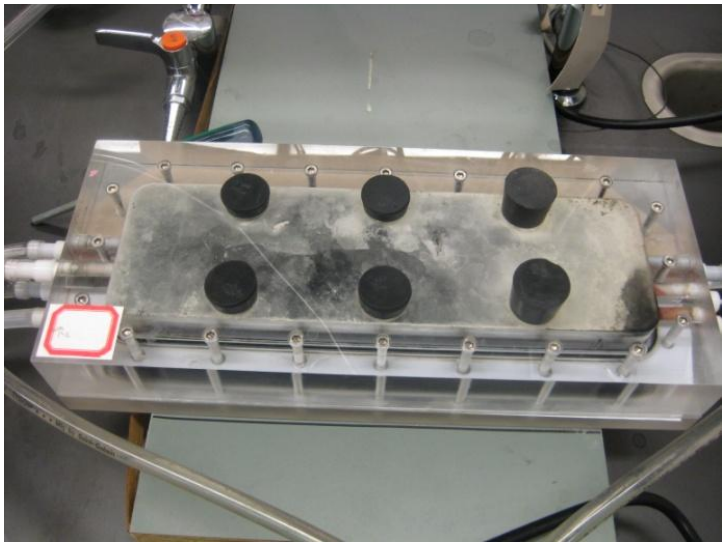

Figure 3-4 Photographic illustration of MABR 2

The two reactors had similar start up procedures. The reactors were inoculated with activated sludge collected from the anaerobic digester at Gold Bar Wastewater Treatment Plant in Edmonton. To initiate the formation of MABs, the reactors were filled with nitrogen bubbled DI water and seeded with the sludge. DI water was used instead of synthetic wastewater because some starved bacteria are more adhesive than their well-fed counterparts (Dawson *et al.*, 1981; Kjelleberg & Hermansson, 1984). On the first day, the reactor was operated in batch mode with recycling rate of 100 mL·min^{-1}. Oxygen was supplied at 10 mL·min^{-1} and 50 kPa from the membrane. On the second day, a base film of cells formed on the membranes. Then, the reactor was switched from batch to continuous flow mode. The synthetic wastewater (composition of which is shown in Table 3-1) continuously flowed into the reactor. The recycling rate increased to 200 mL·min^{-1} and the oxygen supply increased to 20 mL·min^{-1} and 50 kPa.

Table 3-1 Composition of synthetic wastewater in MABR 1 and MABR 2

Constituents	Concentration (mg·L^{-1})
Dextrose	250 (as COD)
KH_2PO_4	5 (as P)
NH_4Cl	20 (as NH_4^+-N)
Na_2SO_4	250 (as SO_4^{2-})
$MgCl_2 \cdot 6H_2O$	12.86
$FeSO_4 \cdot 7H_2O$	2.57
$CoCl_2 \cdot 6H_2O$	0.26
$CaCl_2 \cdot 2H_2O$	0.77
$CuSO_4 \cdot H_2O$	0.26
$MnCl_2 \cdot 4H_2O$	0.26
$ZnSO_4 \cdot 7H_2O$	0.26
Yeast Extract	1
$NaHCO_3$	To adjust pH

The two reactors were operated for around one year with the help of a Master of Science student, Sabinus Okafor, in the Department of Civil and Environmental Engineering at University of Alberta. Initially, the two reactors were operated at the same conditions. Oxygen supply of 20 mL·min^{-1} at pressure of 50 kPa was provided from the membrane side. 50 mL·min^{-1} nitrogen gas was purged into the influent of synthetic wastewater. NO_3^- was absent in the influent. The influent flow rate of synthetic wastewater was maintained around 2 mL·min^{-1}. The recirculation rate was around 200 mL·min^{-1}. The hydraulic retention time was maintained at 5.6 h.

Note that initially, these two reactors were designed to investigate the possible difference of biofilm structures between biofilms growing on different membranes. Because one of the membranes in MABR 2 was damaged during the microsensor measurements, only MABR 1 was eventually used to conduct this research. To provide future reference for the readers who are interested in the reactor design the design of the two MABRs was introduced here.

Once the MABs were well developed, the chemical gradients in the biofilms were measured using microsensors. Thereafter, some substrate concentrations were changed, which is described in Chapter 6. Other operating parameters were kept the same.

3.2 Chemical analyses

Bulk reactor conditions were monitored regularly. Dissolved Oxygen (DO) concentration, NH_4^+ concentration, pH and ORP in the influent and effluent were measured using commercial electrodes and meters after collecting the samples. For DO measurements, an oxygen membrane electrode (Model: Orion 97-08, Thermo Electron Corporation) with a DO meter (Model: 50B, YSI Inc., USA) was used. An ammonia electrode (Cat.# 13-620-509, Accumet, Fisher Scientific) with a pH meter (AR 15, Accumet, Fisher Scientific) was involved for ammonia measurements. For pH measurements, a pH electrode (Cat.# 13-620-108, Accumet, Fisher Scientific) with a pH meter (AR 15, Accumet, Fisher Scientific) was used. An ORP electrode (Cat.# 13-620-81, Accumet, Fisher Scientific) with a pH meter (AR 25, Fisher Scientific) was used for ORP measurements. COD was analyzed according to the standard methods (APHA *et al*., 1999) using Digital Reactor Block 200 digester (Model: DRB 200, Hatch). The concentration of SO_4^{2-}, NO_2^- and NO_3^- in the influent and effluent were determined periodically using ion chromatography (Model: ICS-2000, Dionex). The samples for SO_4^{2-}, NO_2^- and NO_3^- were filtered with a 0.45 μm membrane filters before analysis.

3.2 Microsensors

Microsensors employed in this research are electrochemical sensors and can be divided into two groups: amperometric microsensors and potentiometric microsensors.

3.2.1 Amperometric microsensors

In this research, the amperometric microsensors include combined oxygen microsensors and combined H_2S microsensors. Both of the combined microsensors consist of a working electrode with a glass shaft, a guard electrode, a reference electrode, an outer casing, electrolyte, and gas permeable silicone membrane. The detailed fabrication procedures of the combined H_2S microsensor are shown in Chapter 4. This section introduces the fabrication approach of combined oxygen microsensor, which is based on the procedures described by Lu and Yu (2002).

Fabrication

Step 1: Preparing a working cathode. This step included three parts: the preparation of a glass shaft, the preparation of the tip of Pt wire and the assembly of the working cathode.

A glass shaft was prepared as follows. White glass tubing (ID / OD: 3.0 / 4.0 mm; Schott 8350, Schott-Rohrglas GmbH, Germany) and green glass tubing (ID / OD: 2.69 / 3.33 mm; Schott 8533, Schott Glas Export GmbH, Germany) were used for the glass shaft. The green and white tubings were pulled, cut and jointed in the following manners: Firstly, the cleaned glass tubing, either the green or the white one, was heated at the middle section over a CH_4 gas burner. When the heated portion became very soft, the glass tubing was taken out of the flame and immediately pulled horizontally by both hands. The middle section of the white glass tubing was pulled until its outer diameter became smaller than the inner diameter of green glass tubing, while the middle section of the green glass

tubing was pulled until its inner diameter was slightly bigger than the diameter of the Pt wire (99.99%, diameter: 0.1 mm, Sigma-Aldrich Company, Canada). Secondly, the pulled part of the white glass tubing was cut so that the pulled ends were about 2 cm in length. The pulled part of the green glass tubing was cut in half and then the two un-pulled ends were cut so that they were slightly longer than or just fit for the pulled end of the white glass tubing. Subsequently, the glass shaft was made by vertically inserting the pulled end of the white glass tubing into the un-pulled end of the green tubing and melting them together by appropriately rolling them over a horizontal frame of butane burner (Model #: ST1000TS, Micro Torch, USA).

Then the tip of a piece of Pt wire was tapered in the following manners. One end of a piece of Pt wire (about 6 cm long) was welded to one end of a piece of Ag wire (about 8 cm long, 99.99+%, diameter: 0.25 mm; Sigma-Aldrich, Canada), referred to as Ag-Pt wire. The introduction of Ag wire made the handling easier and decreased the cost of the metal wire because the Ag wire was thicker and cheaper than the Pt wire. The Ag wire of the Ag-Pt wire would not come into contact with the electrolyte and would not undergo redox reactions, but it can pass the electron. The Ag wire end of the Ag-Pt wire was connected with one end of a graphite rod via an adjustable power supply containing two transformers (transformer 1: primary: 115V, secondary: 12.6V, 10A, Model #:167S12, Hammond Manufacturing, Ont., Canada; transformer 2: Type 116, the Superior Electric Company, USA), while the Pt wire end of the Ag-Pt wire and the other end of the graphite rod were placed in the 1 M alkaline KCN solution to

etch the Pt wire end. During the etching process, the Ag-Pt wire was moved up and down continuously. Meanwhile, the voltage was decreased slowly from 4 V to 1 V. This process might be repeated several times until the tapered tip diameter became small. The tip diameter of the Pt wire was checked under a vertical microscope with a built-in scale (Model: Axioskop 2 Plus, Carl Zeiss) after cleaning the etched Pt wire by immersing it into three beakers of DI water in series.

Finally, the working cathode was assembled according to the following procedure. The etched Ag-Pt wire with a tip diameter of 3-5 μm was gently inserted into the glass shaft from the end of the white glass tubing. The Ag wire end was extended out of the white glass tubing, and the etched Pt wire end was stayed in the green capillary about 4-5 cm. The tip was again checked under the microscope to confirm that it was not broken or bent during the insertion. Then the capillary end of the glass shaft with the Pt wire in it was hung using a small clip mounted on the micromanipulator (Model: M3301R, World Precision Instruments Inc., USA). An illuminator (KL 1500 LCD, Carl Zeiss) was used for clear observation. The following process was monitored under a horizontal stereomicroscope (Model: Stemi SV11, Carl Zeiss, Germany): First, by adjusting the micromanipulator, the capillary part was placed in the center of a W-shaped heating loop, which was connected with a power supply. Second, the tip of the Pt wire inside the glass shaft was placed 1.5-2.0 cm above the heating loop. Then, the heating loop was gradually heated, and the glass capillary was gently moved up and down. Once the glass capillary was very close to the Pt wire (at about 0.5-

1.0 cm above the heating loop) due to the melting of the glass shaft, the voltage was suddenly increased (doubled). Thereafter, the tip of the Pt wire was coated with the melted glass shaft, and the whole glass shaft fell into a beaker underneath, with tissue paper around the inside. In order to expose a surface for electrode reaction, the glass coating over the tip of the Pt wire was removed by using a pair of micro-dissecting tweezers (Cat. #: RS-4905, Roboz Surgical Instrument Co., USA). This step was conducted under a vertical microscope and required careful hand-eye coordination.

Step 2: Gold- plating of the tip of the working cathode. An Ag-Pt wire was prepared by soldering a piece of Ag wire (99.99%; diameter: 0.25 mm, Sigma-Aldrich) with a short piece of Pt wire (99.99%; diameter: 0.1 mm, Sigma-Aldrich). The Ag-Pt wire was then inserted into a Pasteur pipette (Cat.# 13-678-20C, Fisher Scientific), with the end of Ag wire out of the large end and the end of Pt wire inside the small end (*i.e.*, tip). The end of Ag wire was glued with the Pasteur pipette using epoxy. 0.1 M $AuCl_3$ solution ($HAuCl_4 \cdot 3H_2O$; G54-1, Fisher Scientific) was sucked into the tip of the Pasteur pipette so that the end of Pt wire was immersed in the $AuCl_3$ solution. Then, the Pasteur pipette was horizontally fixed on a manipulator (Model: M3301R, World Precision Instruments Inc., USA) and the working cathode was horizontally fixed on the stage of a microscope (Model: Axioskop 2 plus, Carl Zeiss). The naked tip of working cathode was plated with gold as follows: the negative pole of a 1.5 V battery was connected to the Ag wire in the working cathode shaft, and the positive pole of the same battery was connected to the Ag wire in a Pasteur

pipette. Then, the Pasteur pipette was advanced through the movement of the manipulator so that the naked tip of working cathode was immersed into the $AuCl_3$ solution and left there until a thin layer of gold around the naked tip was achieved.

Step 3 Preparing a guard cathode. A piece of white glass tubing was pulled until its inner diameter became very small and then cut into capillary sections about 8 cm long. A piece of Ag wire (99.99%; diameter: 0.127 mm; Cat.# 265551, Sigma-Aldrich) of 20 cm long was inserted in the glass capillary section. Two ends of the Ag wire extended out of the capillary. Then, two ends of the capillary were sealed with epoxy (5 minute Permapoxy, Permatex Canada Inc., Ontario). After the epoxy completely dried, one of the exposed ends of the Ag wire was etched until a tapered tip (1-5 μm in diameter) was obtained. The etching process of the Ag wire was the same as that described in the preparation of the working cathode.

Step 4 Preparing a reference electrode - Ag/AgCl. Two pieces of Ag wire (99.99%; diameter: 0.25mm, Sigma-Aldrich), which were connected to the negative and positive pole of a 1.5 V battery, respectively, were partially (about half of the length) immersed in 1 M HCl solution in a small beaker. After a few minutes, the immersed section of the Ag wire connected with the positive pole would turn brown due to the formation of AgCl. Then, the brown section was immersed in DI water to rinse. After drying, the Ag/AgCl wire could later serve as the reference electrode.

Step 5 Preparing an outer casing. The fine section (close to the joint) of a cleaned Pasteur pipette (Cat.# 13-678-20C, Fisher Scientific) was first pulled horizontally by hand until an inner diameter of about 0.5 mm was obtained. This procedure was similar to that used for pulling the white glass tubing. Then, the pulled end was vertically pulled again to reach a small capillary. This procedure was similar to that used for coating the working cathode. The suitable length of the tapered outer casing tip could be adjusted by a microdissecting tweezer at a later stage.

Step 6 Assembling an oxygen microsensor. Before assembling the oxygen microsensor, the tip of the working cathode was checked if the gold was still there under a microscope (Model: Axioskop 2 Plus, Carl Zeiss). The tapered outer casing was horizontally fixed by a spring clip on the microscope stage. A pair of microdissecting tweezers was used to cut the capillary of the outer casing, letting the capillary's inner diameter be about 20-30 μm. Then the shaft of the working cathode was gently inserted (avoid the gold falling off) from the large end into the capillary of outer casing. The distance between the tip of working cathode and the outer casing was maintained about 30-40 μm. The working cathode was then fixed by another spring clip on the microscope stage and the guard cathode was inserted along the working cathode into the capillary section of the outer casing. The tip of the guard cathode was located behind the tip of the working cathode. The distance between the tip of the working cathode and guard cathode was about 150-300 μm within the tip. Subsequently, the reference anode was horizontally

inserted into the outer casing until it was located in the middle of the outer casing's large section.

To prepare the silicone membrane inside the microsensor tip, another Pasteur pipette covered with silicone (Medical Adhesive Silicone Type A, Dow Corning, USA) at its tip was horizontally mounted on a micromanipulator. Then the Pasteur pipette was advanced toward the tip of outer casing through the movement of the manipulator so that the tip of outer casing inserted into the silicone until a silicone membrane (10-20 μm long) was obtained there. Afterwards, epoxy was applied to fix the working cathode, guard cathode and reference anode onto the large end of the outer casing (open space between three electrodes and the outer casing was required for injecting electrolyte and pouring glass beads at later steps). The open end of the glass shaft of working cathode was also sealed using the epoxy. Let the epoxy and silicone membrane air dry for at least one night.

Before injecting the electrolyte solution, DI water was heated over a gas burner for removing possible bubbles at a later step. Then, a little fresh electrolyte solution (a mixture of 0.2 M $KHCO_3$, 0.3 M K_2CO_3, 1.0 M KCl and a little thymol) was slowly injected into the fine section along the wall of the outer casing using a 1 mL syringe (Cat.# 309597, Becton Dickinson & Co., USA) with a filter device (Puradisc 25pp, 0.2 μm; Cat.# 5-713-401, Fisher Scientific). When the fine section of the outer casing was filled with the electrolyte, it was checked under the vertical microscope to see if there were any air bubbles. If bubbles were present, the tip region was dipped into the above-mentioned boiling DI water

several times until the air bubbles disappeared. Thereafter, a very small quantity of glass beads (diameter: 20-40 μm, filter aid 400, 3M Empore, USA) were added into the tip region of the outer casing from the open space. The glass beads were used to keep the possible deposition of particles from the tip area. Subsequently, more electrolyte solution was injected until the outer casing was full. Epoxy was immediately applied to seal the outer casing completely and dried in the air.

Calibration

Before calibration, the oxygen microsensor was polarized at a potential of -0.8 V by immersing its tip in a custom-made calibration chamber filled with DI water and connecting the electrodes to a picoammeter (PA2000, Unisense, Denmark). The connection order was shown as follows: firstly connect the reference anode to the reference terminal, second connect the working cathode to the input terminal, and finally connect the guard cathode to the guard terminal. During the polarization process, the signal was initially very high and dropped very quickly within the first few minutes. Then the rate of signal decrease became smaller and smaller until a stable zero current was achieved, which fluctuated within ±1 pA.

Considering the measuring range in this study, the calibration was conducted using three points: nitrogen gas (0% oxygen), compressed air (21% oxygen, DO: 8.36 mg L^{-1}) and pure oxygen (100 % oxygen, DO: 40 mg L^{-1}). The calibration curves of the oxygen microsensor were illustrated in Figure 3-5. This microsensor was very stable (1 pA per 10 min) and had good sensitivity (25 pA mg^{-1} L of DO) and fast response time (<1 second).

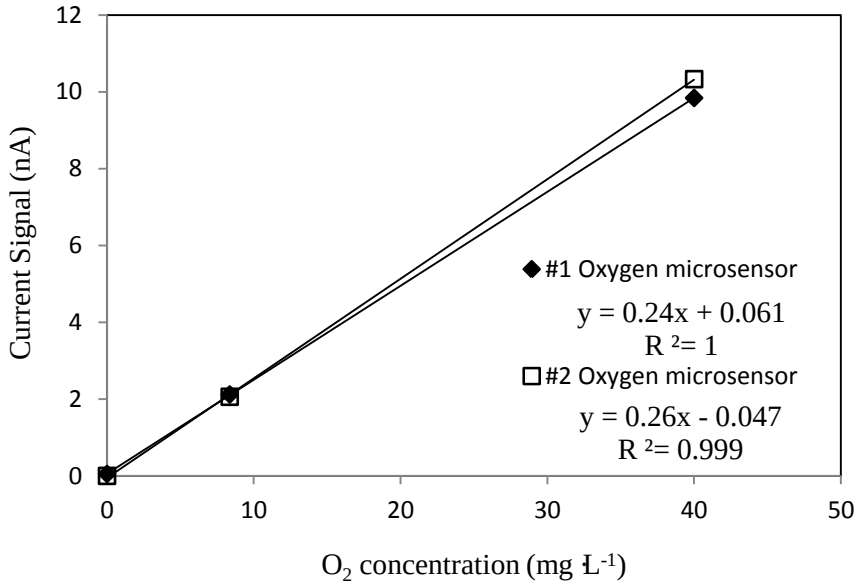

Figure 3-5 Calibration curves of oxygen microsensors

3.2.1 Potentiometric microsensors

In this research, the potentiometric microsensors include ammonia, nitrate, pH and ORP microsensors. Among them, the first four microsensors are based on LIX principle, which are called LIX microsensors. The preparation of the LIX microsensors has similar procedures. Therefore, it is described in one section as follows.

LIX microsensor

A LIX microsensor system consists of an ion-selective electrode with LIX membrane and a half-cell reference electrode with liquid junction. The reference electrode is commercially available. The preparation of a LIX microsensor is described in the following part.

Selection and preparation of chemicals. The chemicals used during the preparation of a LIX microsensor include internal reference solution, membrane

solution (or liquid ion-selective membrane), conditioning solution and standard solution. The internal reference solution for each LIX microsensor was selected and prepared as follows: pH 7.0 buffer solution (Cat.# SB107-500, Fisher Scientific) + 0.3 M KCl for pH microsensor, 0.01 M NH_4Cl ((Cat.# 09677, Fluka, Sigma-Aldrich, Canada) for ammonia microsensor and 0.1 M KCl +0.1 M KNO_3 for nitrate microsensor (de Beer *et al*., 1997). The membrane solution for each LIX microsensor was commercially available: Hydrogen ionophore I - cocktail B (Cat.# 95293, Fluka, Sigma-Aldrich, Canada), for pH microsensor. Ammonium ionophore I - cocktail A (Cat.# 09879, Fluka, Sigma-Aldrich, Canada) for the ammonium microsensor and Nitrate ionophore - cocktail A (Cat.# 72549, Fluka, Sigma-Aldrich, Canada) for the nitrate microsensor. The conditioning solution is prepared as follows: pH 7 buffer solution (Cat.# SB108-500, Fisher Scientific) for the pH microsensor, 0.02 M NH_4Cl made from 0.1 M NH_4^+ standard solution (Cat.# 09683, Fluka, Sigma-Aldrich, Canada) for the ammonia microsensor and 0.1 M KNO_3 for the nitrate microsensor (Yu, 2000).

A series of standard solutions were used during the calibration for each LIX microsensor: buffer standard solution of pH 6, 7, 8 and 9 (Cat.# SB104B-500, Cat.# SB108-500, SB112B-500 and SB114-500, respectively, Fisher Scientific) for the pH microsensor; 10^{-5}, 10^{-4}, 10^{-3}, 10^{-2} M of NH_4^+ made from 0.1 M NH_4Cl standard solution (Cat.# 09683, Fluka) for the ammonia microsensor; 10^{-5}, 10^{-4}, 10^{-3}, 10^{-2} M of NO_3^- made from KNO_3 solution for the nitrate microsensor (Yu, 2000).

Fabrication. All of the LIX microsensors used in this research have similar fabrication steps. Most of the materials and instruments are the same except the chemicals listed in the above section. The fabrication approach is mainly based on the procedures described by Yu (2000) and Lu (2008).

Step 1: Pulling the glass micropipettes. A microprocessor-controlled vertical pipette puller (PUL-100, World Precision Instruments Inc., USA) with a trough-shaped heating filament (Cat.# 13835, World Precision Instruments Inc., USA) was used to pull the glass micropipettes (OD: 1.2 mm, length: 150 mm; Cat.# 1B120F-6, World Precision Instruments Inc., USA). The puller can be programmed to obtain different tip sizes and shapes. In this research, the pulled micropipettes were around 75 mm long with a 15 mm length of tip.

Step 2: Breaking the tip of the pulled micropipettes. After the pulling, the tip of the glass micropipette was usually sealed. The sealed tip of the freshly pulled micropipette was broken by either bumping with a tip-closed Pasteur pipette mounted on a manipulator (Model: M3301R, World Precision Instruments Inc., USA) or gently cutting with a microdissecting tweezer (Cat.# RS-4905, Roboz Surgical Instrument Co., USA). The process of breaking the tip was conducted under a horizontal stereomicroscope (Model: Stemi SV11, Carl Zeiss). The final diameter of the tip was different for each kind of microsensor, depending on the performance of that microsensor and the properties of LIX membrane for that microsensor, such as the viscosity. The tip diameter was around 3-5 μm for pH and ammonia microsensors and 8-10 μm for nitrate

microsensors. The unsealed micropipettes were temporarily stored in an electrode storage jar (Cat.# E212, World precision Instruments Inc., USA).

Step 3: Silanization of the tip. The "Dip and bake" silanization method was used: The tip of the unsealed micropipettes was dipped into silanization reagent N, N-dimethyltrimethylsilylamine (Cat.# 41716, Fluka) for a few seconds. Then, the tip was drawn up and dipped into the silanization reagent several times. Afterwards, the micropipettes were placed in a custom-made holder and baked in a pre-heated oven at 180 ^{0}C for around 24 hours. During this process, the silicone compound of the silanization reagent was expected to bind covalently with the free hydroxyl groups of the glass to yield a lipophilic glass surface. After the micropipette cooled down to room temperature in a dark and vacuumed desiccator, it was ready for the electrode filling.

Step 4: Electrode filling: This step consisted of back-filling (filling through the stem) with internal reference solution and front- filling (filling through the tip) with LIX membrane. Note that each type of microsensor has its own internal reference solution and membrane solution. The internal reference solution was filled into the micropipette through the stem (back end of the micropipette) with the help of micro-fill needle (Cat.# MF28G-5, World Precision Instruments Inc.) attached to a syringe. Once a full drop of internal reference solution was seen to flow out of the tip, the tip (front end of the micropipette) was immediately dipped into the LIX membrane solution until a column of the membrane was formed at the tip by the capillary forces. The length of the membrane at the tip and the clear division between the membrane solution and

internal reference solution (Figure 3-6) could be observed under the microscope. The length of the membrane was of the order of 500 µm for the pH and ammonium microsensors and 100 µm for the nitrate microsensor, depending on the membrane properties.

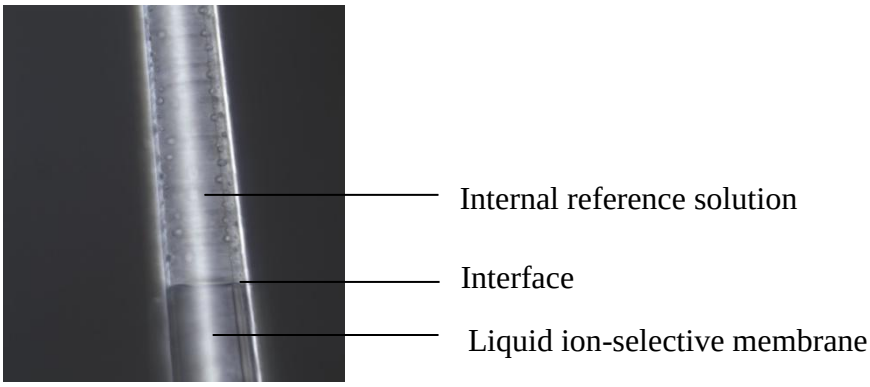

Figure 3-6 Microscopic photographic illustration of a LIX microsensor

Step 5: Coating with protein layer: to keep the membrane stay longer inside the LIX microsensor tip, an insoluble protein layer was coated onto the tip according to the following procedure: after electrode filling, inserting the micropipette tip into a cellulose acetate/acetone solution (10%, w/v) for a few seconds and then into 1 mL of protein solution containing 10% bovine serum albumin, 50 mM sodium phosphate and 10 µL of 50% glutaraldehyde for several minutes

Step 6: Conditioning the microsensor: The completed microsensor was put into the conditioning solutions for at least 2 hours before its use.

Calibration. Before calibration, an Ag/AgCl wire was inserted into the microsensor from the stem, which served as the internal reference electrode.

Preparation of the Ag/AgCl wire was the same as the preparation of the reference electrode for the oxygen microsensor as described in the Step 4 of Section 3.2.1. The LIX microsensor with internal reference electrode would serve as a working electrode. During calibration, a LIX microsensor and a commercially purchased Ag/AgCl micro-reference electrode (Cat.# MI-409, Microelectrodes Inc., USA) were connected to an electrochemical analyzer (Model 600B, CH Instruments). and placed into a series of standard solution for a specific microsensor. Then the potential measurements were taken when the reading was stable. Note that the standard solution was stirred on an electric stirrer and then stopped stirring before both electrodes were lowered into the standard solution. To avoid electromagnetic interference, this setup (two electrodes, standard solutions and the stirrer) were put in a Faraday cage (Technical Manufaturing Corporation, USA).

The calibration curves for pH, ammonium and nitrate microsensors are illustrated in Figure 3-7, 3-8 and 3-9 respectively. These calibration results showed that this procedure produced good microsensors but each microsensor needs to be individually calibrated. The results also demonstrated that the selected chemicals and fabrication procedures are effective for the pH, ammonia and nitrate microsensors.

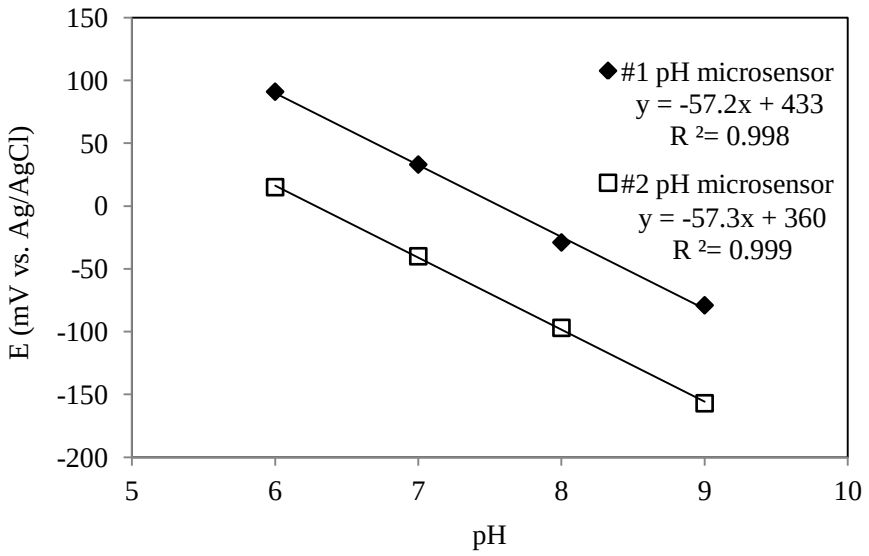

Figure 3-7 Calibration curves of pH microsensors

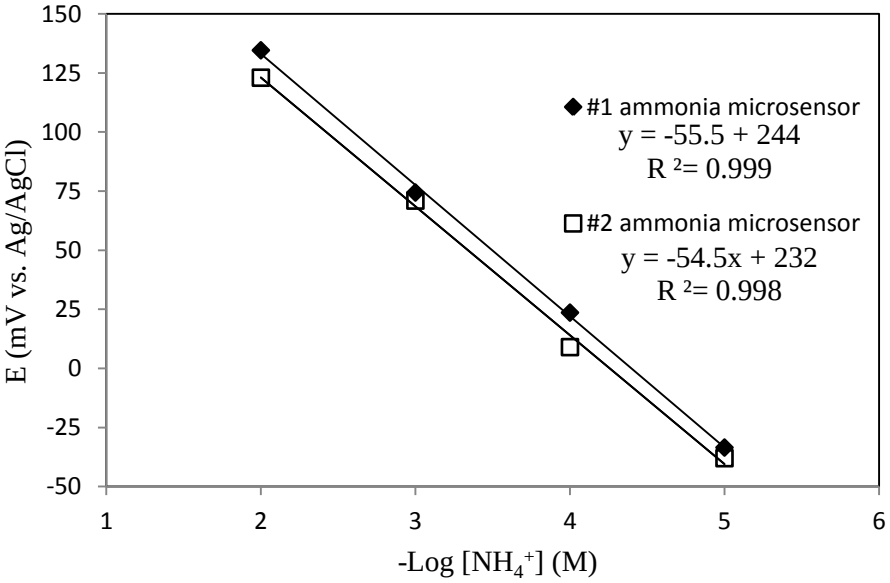

Figure 3-8 Calibration curves of ammonium microsensors

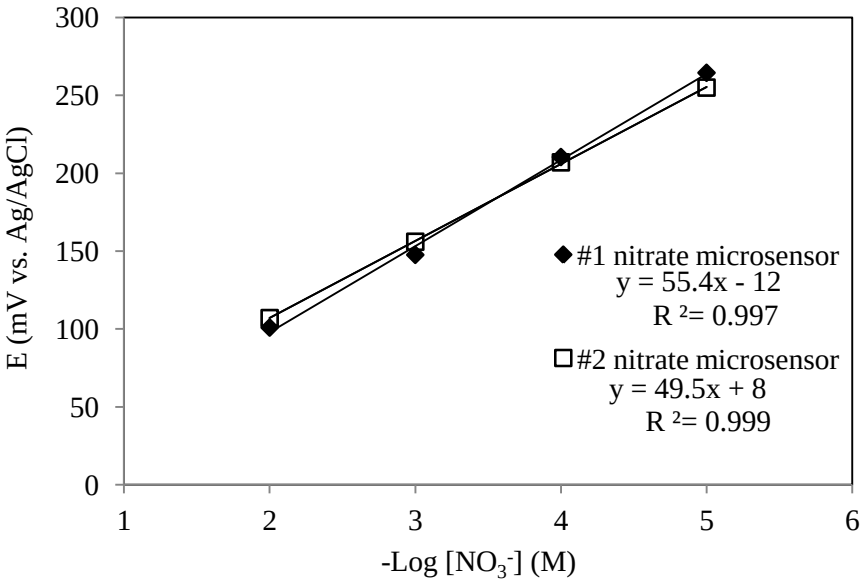

Figure 3-9 Calibration curves of nitrate microsensors

ORP microsensor

The principle of an ORP microsensor is simple: measure the potential drop across a measuring electrode (or working electrode) and a reference electrode, with a solution in between. The fabrication procedures of the measuring electrode are the same as those of the working cathode for oxygen microsensor described in section 3.2.1. This approach produced an ORP microsensor with a tip diameter of approximately 10 μm. The following evaluation process was based on the literature (Yu, 2000).

Evaluation. The potential response of an ORP microsensor was checked against both standard and reference solutions. The ferrous-ferric solution was used as standard solution, which contained 0.1 M $Fe(NH_4)_2(SO_4)_2 \cdot 6H_2O$, 0.1 M $Fe(NH_4)(SO_4)_2 \cdot 12H_2O$ and 1.0 M H_2SO_4. Two quinhydrone solutions, one at pH 4 and the other at pH 7, were used as reference solutions, as suggested by the

American Society for Testing and Materials (ASTM D1498-93). The pH 4 quinhydrone reference solution was freshly prepared by dissolving 1 g quinhydrone in 100 mL of pH 4 buffer solution and the pH 7 quinhydrone reference solution was freshly prepared by dissolving 1 g quinhydrone in 100 mL of pH 7 buffer solution. The nominal potentials of the standard and reference solutions can be obtained and combiled according to ASTM D1498-93 (Yu, 2000). To check the potential response, in a Faraday cage (Technical Manufacturing Corporation), the ORP microsensor and a commercially purchased Ag/AgCl micro-reference electrode (Cat.# MI-409, Microelectrodes Inc., USA) were placed in the standard or reference solutions, respectively. The electrolyte solution in the reference electrode was a 3 M KCl solution. The experimental temperature during the calibration was 23 ^{0}C. The potential drops between the ORP microsensor and the reference electrode in the standard and reference solutions were read from an electrochemical analyzer (Model 600B, CH Instruments). Figure 3-10 shows the response curves of two ORP microsensors against the standard and reference solutions. The slopes of both curves are 1.01 and 1.02, respectively, which are quite close to the theoretical value of 1.00. These results show that this procedure produced good microsensors but each microsensor needs to be individually calibrated.

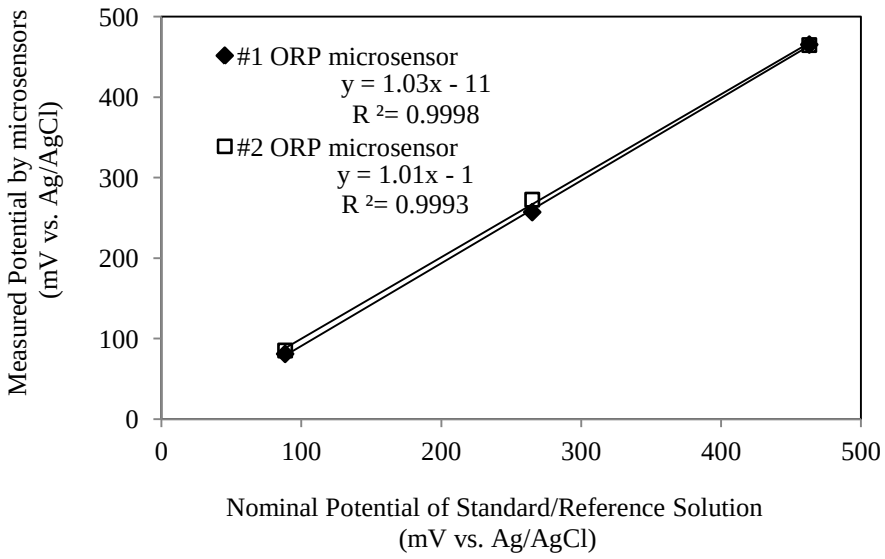

Figure 3-10 Potential response of ORP microsensors in standard and reference solutions

3.3 Biofilm measurements

When all of the microsensors and biofilms were ready for measurements, each microsensor was fastened onto a micromanipulator. The electrode assembly and the biofilm in the reactor were put inside a Faraday cage to reduce the electrical noise. The schematic diagram of the measurement setup is shown in Figure 3-11. Immediately before and after the measurement, each electrode was calibrated. The biofilm thickness was viewed by using a horizontal stereomicroscope and determined by the distance traveled by the micromanipulator. During measurements, the reactor was paused in order to avoid any disturbances and the tip of microsensors was advanced into the biofilm from the access window at the top of the reactor through the movement of the micromanipulator. The profiles of O_2, pH, H_2S, ORP, NH_4^+ and NO_3^- along the biofilm depth were measured using corresponding microsensors.

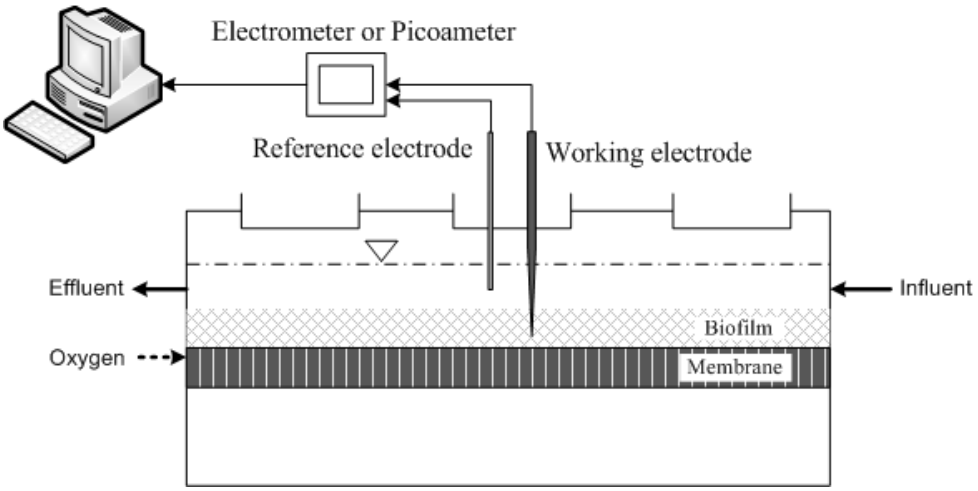

Figure 3-11 Schematic diagram of measurement setup using microsensors

3.4 Microscopy observation

After completing all of the microsensor measurements inside the MABs, the biofilm samples were cut together with the membranes. Then, the biofilm samples together with the membranes were sent to the Department of Biology at University of Alberta to treat the samples for SEM observation according to standard methods. During the sample treatments, the biofilms were separated from the membranes. Finally, the cross section of the biofilm samples, the biofilm surface near the membrane and the biofilm surface near the bulk liquid were observed using a SEM.

References

APHA, AWWA and WEF. 1999. Standard methods foor the examination of water and wastewater. 20th edition. American Public Health Association. Washington D.C.

Dawson M. P., Humphrey B. A., Marshall K C. 1981. Adhesion: a tactic in the survival strategy of a marine vibrio during starvation. Curr Microbiol, 6: 195-199

Kjelleberg S., Hermansson M. 1984. Starvation-induced effects on bacterial surface characteristics. Appl.Environ Microbiol, 48:497-503

De Beer, Schramm S., Santegoeds C. M., Kuhl M. 1997. A Nitrite Microsensor for Profiling Environmental Biofilms. Applied and Environmental Microbiology, 973–977

Lu, R. and Yu, T. 2002. Fabrication and evaluation of an oxygen microsensor applicable to environmental engineering and science. J. Environ. Eng. Sci. (1): 225-235.

Lu, C. 2008. Monochloramine penetration in biofilms and nitrification detection in a model chloraminated water distribution system. University of Alberta. Doctor of Philosophy thesis.

Yu, T. 2000. Stratification microbial process and redox potential changes. University of Cincinnati. Doctor of Philosophy thesis.

Chapter 4

Fabrication of H_2S Microsensor Applicable to Biofilm Studies

4.1 Introduction

H_2S is one of the principle end products of the sulfate reduction process (Barton, 1995) and plays an important role in biogeochemical processes of the environmental system (Jeroscheski *et al*. 1996). Oxidation of H_2S by sulfide oxidizing bacteria might lead to the corrosion of concrete or metal pipes carrying sewage (Sawyer *et al*. 2003). Reaction of H_2S with heavy metal might cause the formation of precipitates (Boothman *et al*. 2006). Moreover, H_2S is malodorous and toxic to higher organisms even at low levels ((Jeroscheski *et al*. 1996). Therefore, the *in situ* determination of H_2S concentration during the biogeochemical or biochemical processes in microbial community such as environmental biofilms is significant.

Microsensor techniques have exhibited excellent superiority in the *in situ* determination of chemical gradients and the bacterial activities in microbial communities (Santegoeds *et al*., 1998; Okabe *et al*., 2003; Okabe *et al*., 2005; de la Rosa and Yu, 2006). To apply the microsensor techniques in biofilm studies, the microsensors' tip must be small and robust enough, and the microsensors must be sensitive and highly selective enough (Schreiber *et al*., 2008). Two kinds of microsensors have been used for the determination of H_2S concentration in biofilm studies: potentiometric sulfide microsensor and amperometric H_2S microsensor. The potentiometric sulfide microsensor measures total sulfide

concentration and the H_2S concentration is calculated according to the proton equilibrium equation (Revsbech and Jorgensen, 1986; Yu *et al*., 1998; Okabe *et al*., 1999). The potentiometric sulfide microsensors can be very small (a few μm), but it can have relatively long response time, signal drifting and deviation from ideal Nerstian response at low sulfide concentrations (Kuhl *et al*., 1998). In contrast, the amperometric H_2S microsensor is relatively new and it can directly determine H_2S concentration. Amperometric H_2S microsensors have many advantages that Lewandowshi and Beyenal (2007) conclude that, whenever there is a choice of using an amperometric or a potentiometric microsensor in a biofilm study, using the amperometric microsensor is preferred.

Jeroschewski *et al*. (1996) first reported an amperometric H_2S microsensor applicable to aquatic environments. This H_2S microsensor had a faster response time and lower detection limit than the potentiometric sulfide microsensor. It could be applied in the study of oxic-anoxic interfaces.

In this chapter, the fabrication procedure of a modified Clark-type amperometric H_2S microsensor is described in detail. The working principle of the H_2S microsensor is addressed. Some effects on the performance of this amperometric H_2S microsensor are also investigated. This H_2S microsensor has high spatial resolution and has been applied in biofilm studies. Two biofilm samples were used in this study: a MAB growing on a silicone membrane in a MABR and a conventional biofilm growing on an aerobic rotating biological contactor wastewater treatment system. The results of microsensor measurements were supplemented with FISH results to demonstrate the activity of sulfate

reduction in biofilms.

4.2 Principle of the H_2S microsensor

This Clark-type amperometric H_2S microsensor consisted of three electrodes: a working anode (Pt wire), guard anode (Pt wire) and reference cathode (Pt wire). These electrodes and the electrolyte potassium ferric cyanide ($K_3Fe(CN)_6$) were combined into one body. The H_2S microsensor's tip was covered with a layer of silicone membrane. The configuration of the H_2S microsensor is shown in Figure 4-1.

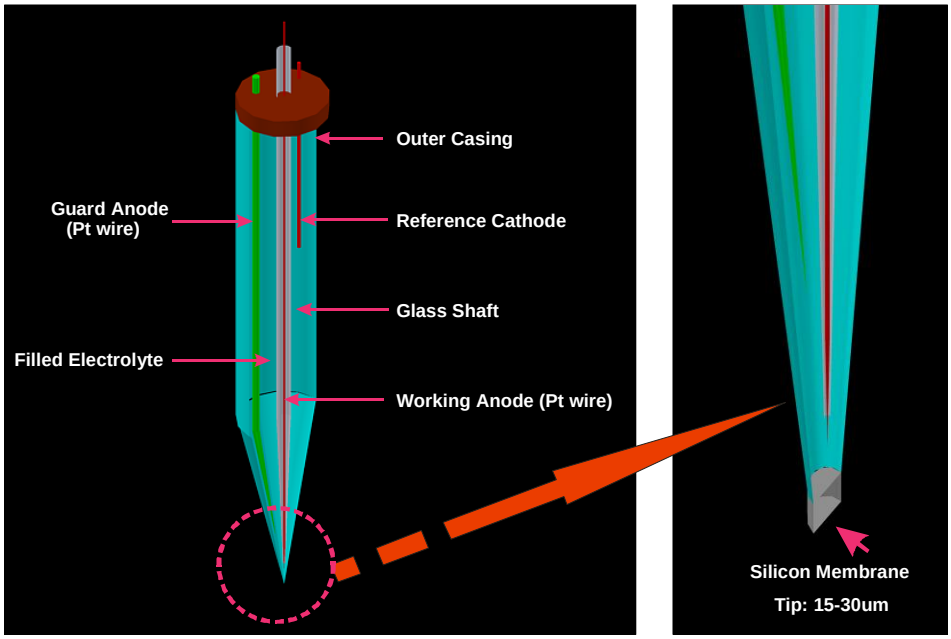

Figure 4-1 Schematic diagram of H_2S microsensor

Before measurements, the Clark-type amperometric H_2S microsensor was polarized and calibrated. The reactions involved during the polarization, calibration and measurements are shown as follows.

$$2Fe(CN)_6^{3-} + 2e^- = 2Fe(CN)_6^{4-} \qquad \text{(Eq.4-1)}$$

$$2Fe(CN)_6^{3-} + H_2S = 2Fe(CN)_6^{4-} + 2H^+ + S \qquad \text{(Eq.4-2)}$$

$$2Fe(CN)_6^{4-} = 2Fe(CN)_6^{3-} + 2e^- \qquad \text{(Eq.4-3)}$$

The illustration of the reactions during calibration and measurement are shown in Figure 4-2:

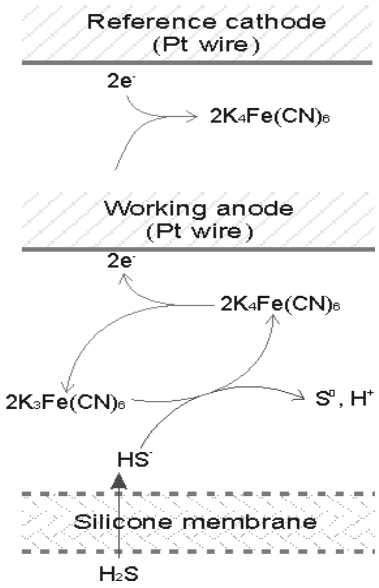

Figure 4-2 Illustration of the reactions during calibration and measurement

During polarization, the working anode and guard anode were polarized at controlled positive potential versus reference cathode, which was determined by the experiment shown in Figure 4-3. If any possible reducer existed in the electrolyte or at the surface of the microsensor, it could be oxidized there. Thus, the subsequent measurements on currents could accurately reflect H_2S transportation across the silicone membrane. The equilibrium of $Fe(CN)_6^{3-}$ /$Fe(CN)_6^{4-}$ was established at the reference cathode (Eq.4-1). This polarization step was like a control test.

During calibrations and measurements, H_2S from the samples penetrated the gas permeable silicone membrane and reacted with $Fe(CN)_6^{3-}$ in the solution of the tip region (Eq.4-2). Usually, the H_2S concentration is very small in biofilm samples, therefore, large excess of pH 10.0 buffer and $Fe(CN)_6^{3-}$ in the solution could make the change of the pH value and $Fe(CN)_6^{3-}$ concentration negligible (Eq.4-2). The produced ferrous cyanide ($Fe(CN)_6^{4-}$) reached the tip of the working anode and was re-oxidized to $Fe(CN)_6^{3-}$ there (Eq.4-3). Any excess $Fe(CN)_6^{4-}$ would be transported to the tip of the guard anode and re-oxidized to $Fe(CN)_6^{3-}$ there (Eq.4-3). Therefore, several steps might occur in the tip region: (1) H_2S transportation across the membrane; (2) H_2S reaction with $Fe(CN)_6^{3-}$ to produce $Fe(CN)_6^{4-}$ (Eq.4-2); (3) $Fe(CN)_6^{4-}$ transportation to the working anode or guard anode surface; (4) $Fe(CN)_6^{4-}$ re-oxidization to $Fe(CN)_6^{3-}$ at the working anode or guard anode surface (Eq.4-3). Due to the usually very small H_2S concentration from the biofilm samples, $Fe(CN)_6^{4-}$ could transport to the reference cathode area, and the equilibrium of $Fe(CN)_6^{3-}$ /$Fe(CN)_6^{4-}$ under alkaline conditions near the reference cathode would not be disturbed. The measured current signal of this amperometric H_2S microsensor was the re-oxidation current of potassium ferrous cyanide ($K_4Fe(CN)_6$) at the tip of working anode. The produced $Fe(CN)_6^{4-}$ amount was proportional to the H_2S amount in the sample.

To determine the measuring or polarization voltage, a $\log|i|$ ~E curve (the relationship between the current and potential) was obtained using an electrochemical analyzer (Model 600B, CH Instruments). Figure 4-3 illustrates the $\log|i|$ ~E curve measured between Pt microsensor *vs.* reference Pt in pH 10

phosphate buffer $Fe(CN)_6^{3-}/Fe(CN)_6^{4-}$ solution. In this figure, the potential is from positive to negative from the left to right of the X-axis. When the potential is larger than +0.21 V, the current has no change, which indicates the mass transfer limiting region. When the voltage is smaller than +0.21 V, the current will change rapidly with small changes in potential, which indicates the charge-transfer limiting region (Bard and Faulkner, 2001). To measure the steady-state current of the H_2S microsensor, we have to set the measuring voltage (or polarization voltage) in the mass transfer limiting region.

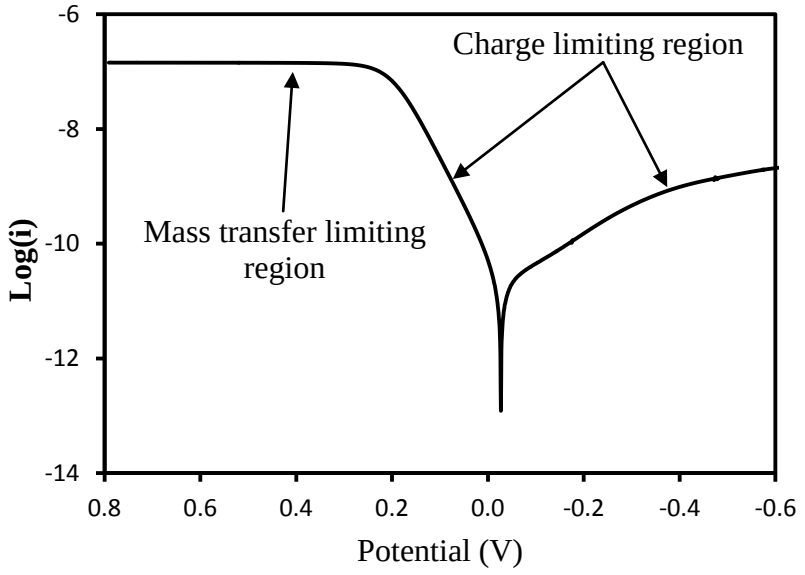

Figure 4-3 $\log|i|$ ~E curve for the $Fe(CN)_6^{3-}/Fe(CN)_6^{4-}$ in pH=10 phosphate buffer, Pt microsensor *vs.* reference Pt

The steady-state currents of a microsensor can be expressed as follows (Bard and Faulkner, 2001):

$$i = nFAm_0C_0^* \qquad \text{(Eq.4-4)}$$

where *i* is steady-state limiting current; n is number of electrons involved in the reaction; F is Faraday constant; A is anode area; m_o is steady-state mass transfer coefficient, which depends on geometry of the microsensor; C_0^* is bulk concentration of species (oxidant).

The terms $nFAm_0$ in Eq.4-4 are constant for a specific microsensor and can be determined by a calibration process. Therefore, for a specific H_2S microsensor, the steady state current is linearly proportional to the $Fe(CN)_6^{4-}$ concentration, which is proportional to H_2S concentration in the sample, shown in Eq.4-2.

4.3 Fabrication procedures and experimental methods

Figure 4-1 illustrated the configuration of the amperometric H_2S microsensor. The basic construction techniques of this H_2S microsensor were derived from those of the Clark-type amperometric oxygen microsensor (Lu and Yu, 2002). The principle design was based on the amperometric H_2S microsensor described by Jeroschewski and Steuckart *et al*. (1996). Due to the presence of the redox couples $Fe(CN)_6^{3-}/Fe(CN)_6^{4-}$ under alkaline conditions, more rigorous selection of materials and the determination of geometric parameters for the tip of the amperometric H_2S microsensor were required. Therefore, better performance of the amperometric H_2S microsensor was more dependent on the practical experience and skills of the researchers. The detailed fabrication procedure could provide better reference for other colleagues. In this section, the fabrication procedure was described in detail based on the author's own laboratory

experience. The evaluation processes of this H_2S microsensor and its measurement procedures were also included.

4.3.1 Fabrication of the H_2S Microsensor

Preparation of the working anode

The working anode consisted of a tapered Pt wire that was coated with a glass shaft. Three steps were involved: preparation of a glass shaft, preparation of a tapered Pt wire and assembly of the working anode. These steps are similar to those for the oxygen microsensor, as described in Chapter 3. To keep the integrity of the fabrication procedures of the H_2S microsensor and provide convenience for the readers, they are again described in detail in this section.

The glass shaft was made of white glass tubing (ID / OD: 3.0 / 4.0 mm; Schott 8350, Schott-Rohrglas GmbH, Germany) and green glass tubing (ID / OD: 2.69 / 3.33 mm; Schott 8533, Schott Glas Export GmbH, Germany). The green and white tubings were pulled, cut and jointed in the following manners: Firstly, the cleaned glass tubing, either the green or the white one, was heated at the middle section over a CH_4 gas burner. When the heated portion became very soft, the glass tubing was taken out of the flame and immediately pulled horizontally by both hands. The middle section of the white glass tubing was pulled until its outer diameter smaller than the inner diameter of green glass tubing, while the middle section of the green glass tubing was pulled until its inner diameter was slightly bigger than the diameter of the Pt wire (99.99%, diameter: 0.1 mm, Sigma-Aldrich Company, Canada). Secondly, the pulled part of the white glass

tubing was cut so that the pulled ends were about 2 cm in length. The pulled part of the green glass tubing was cut in half and then the two un-pulled ends were cut so that they were slightly longer than or just fit for the pulled end of the white glass tubing. Subsequently, the glass shaft was made by vertically inserting the pulled end of the white glass tubing into the un-pulled end of the green tubing and melting them together by appropriately rolling them over a horizontal frame of butane burner (Model #: ST1000TS, Micro Torch, USA).

The tapered tip of the Pt wire was prepared by etching the Pt wire in 1M alkaline (pH >13) KCN solution in a well-ventilated fume hood. One end of the piece of Pt wire (about 6 cm long) was welded to one end of a piece of Ag wire (about 8 cm long, 99.99+%, diameter: 0.25 mm; Sigma-AldrichCompany, Canada), referred to as Ag-Pt wire. The introduction of Ag wire could make the handling easier and decrease the cost of the metal wire because the Ag wire was thicker and cheaper than the Pt wire. The Ag wire of the Ag-Pt wire would not come into contact with the electrolyte and would not undergo redox reactions, but it can pass the electron. The Ag wire end of the Ag-Pt wire was connected with one end of a graphite rod via an adjustable power supply containing two transformers (transformer 1: primary: 115V, secondary: 12.6V, 10A, Model #:167S12, Hammond Manufacturing, Ont., Canada; transformer 2: Type 116, the Superior Electric Company, USA), while the Pt wire end of the Ag-Pt wire and the other end of the graphite rod were placed in the 1 M alkaline KCN solution to etch the Pt wire end. During the etching process, the Ag-Pt wire was moved up and down continuously. Meanwhile, the voltage was decreased slowly from 4 V

to 1 V. This process might be repeated several times until the tapered tip diameter becomes very small (targeting at 1-2 μm). The tip diameter of the Pt wire was checked under a vertical microscope with built-in scale (Model: Axioskop 2 Plus, Carl Zeiss) after cleaning the etched Pt wire by immersing it into three beakers containing DI water in series.

The working anode was assembled after the preparation of the glass shaft and the tapered tip of the Pt wire. The etched Ag-Pt wire with a tip diameter of 1-2 μm was gently inserted into the glass shaft from the end of the white glass tubing. The Ag wire end was extended out of the white glass tubing, and the etched Pt wire end was into the green capillary about 4-5 cm. The tip was again checked under the microscope to confirm that it was not broken or bent during the insertion. Then the capillary end of the glass shaft (with the Pt wire in it) was hung using a small clip mounted on the micromanipulator (Model: M3301R, World Precision Instruments Inc., USA). An illuminator (KL 1500 LCD, Carl Zeiss) was used for clear observation. The following process was monitored under a horizontal stereomicroscope (Model: Stemi SV11, Carl Zeiss, Germany): First, by adjusting the micromanipulator, the capillary part was placed in the center of a W-shaped heating loop, which was connected with a power supply. Second, the tip of the Pt wire inside the glass shaft was placed 1.5-2.0 cm above the heating loop. Then, the heating loop was gradually heated, and the glass capillary was gently moved up and down. Finally, once the glass capillary was very close to the Pt wire (at about 0.5-1.0 cm above the heating loop) due to the melting of the glass shaft, the voltage was suddenly increased (doubled). Thereafter, the tip of

the Pt wire was coated with the melted glass shaft, and the whole glass shaft fell into a beaker underneath, with tissue paper around the inside. In order to expose a surface for electrode reaction, the glass coating over the tip of the Pt wire was removed by using a piece of scientific delicate paper (Fisher Scientific) and a pair of micro-dissecting tweezers (Cat. #: RS-4905, Roboz Surgical Instrument Co., USA). This step was conducted under a vertical microscope and required careful hand-eye coordination. It resulted in a naked tip (2-20 μm long). The surface area of the naked tip, the anode area as indicated in Eq.4-4, is proportional to the current. Therefore, the working anode with proper area will be then carefully stored (not touching anything) for the assembly step of the H_2S microsensor.

Preparation of the guard anode

A piece of white glass tubing was pulled until its inner diameter became very small and then cut into capillary sections (about 8 cm long) as described in the section of oxygen microsensor fabrication in Chapter 3. A piece of Pt wire (20 cm long) was inserted into a glass capillary section. Two ends of the Pt wire were extended out of the capillary. Then, the two ends of the capillary were sealed with epoxy (Permapoxy, Permatex Canada). After the epoxy completely dried, one exposed end of the Pt wire was etched until a tapered tip (1-5 μm in diameter) was obtained. The etching process of the Pt wire was the same as described in the preparation of the working anode.

Assembly of the H_2S microsensor

This process can be summarized in the following steps: the outer casing was tapered; the working anode, guard anode and reference cathode were inserted

into the tapered outer casing; silicone membrane and epoxy were applied; and electrolyte and glass beads were injected.

The tapered outer casing was prepared by pulling the fine section (close to the joint) of a cleaned Pasteur pipette (Cat. #.: 13-678-20C, Fisher Scientific, Canada). The outer casing was firstly pulled horizontally by hand until its inner diameter became about 0.5 mm. This procedure was similar to that used for pulling the white glass tubing. Then, the pulled end was vertically pulled until a very small capillary was obtained. This procedure was similar to that used to pull the capillary end of the glass shaft for the working anode. Then the tapered outer casing was horizontally fixed by a spring clip on the vertical microscope stage. A pair of micro-dissecting tweezers was used to cut the capillary of the outer casing, so that the capillary's inner diameter was about 20-30 μm.

Then, the working anode, guard anode and reference cathode were inserted into the tapered outer casing in the following manners: First, the shaft of the working anode was horizontally inserted from the large end into the capillary of the outer casing. The distance between the tip of the working anode and the outer casing was about 30-40 μm. Second, the working anode was fixed by another spring clip on the vertical microscope stage, and the guard anode was horizontally inserted along the working anode into the capillary section of the outer casing. The tip of the guard anode was located behind the tip of the working anode. The distance between the tip of the working anode and the guard anode was about 150-300 μm. Finally, a piece of Pt wire (100 μm in diameter, around 8 cm long) used for the reference cathode, was horizontally inserted into the outer

casing until its one end was located in the middle and the other end was extended out of the outer casing.

In order to seal the outer casing's tip with the silicone membrane, another Pasteur pipette with silicone (Medical Adhesive Silicone Type A, Dow Corning, USA) at its tip was horizontally mounted on a micromanipulator. Under a vertical microscope, advancing the tip of the Pasteur pipette toward the tip of the outer casing by adjusting the micromanipulator, a silicone membrane (about 10-20 μm in depth) could be obtained within the tip of the outer casing. Afterwards, epoxy was applied to fix the working anode, guard anode and reference cathode onto the large end of the outer casing (open space between the three electrodes and the outer casing was required for injecting the electrolyte and pouring the glass beads at later steps). The open end of the glass shaft was also sealed using the epoxy. Let the epoxy and silicone membrane air-dry for at least one night.

Before injecting the electrolyte solution, DI water was heated over a gas burner. Then, fresh electrolyte solution (0.05 M $K_3Fe(CN)_6$ in pH 10 buffer) was slowly injected into the fine section along the wall of the outer casing using a 1 mL syringe (Becton Dickinson & Co., USA) with a filter device (0.2 μm, Puradisc 25pp, Whatman; Fisher Scientific, Canada). The fine section of the outer casing was checked under the vertical microscope to see if there were any air bubbles. If bubbles were present, the tip region of the outer casing was dipped into the above-mentioned boiling DI water several times until the air bubbles disappeared. Thereafter, a very small quantity of glass beads (diameter: 20-40 μm, filter aid 400, 3M Empore, USA) were added into the tip region of the outer

casing. The glass beads were used to keep the possible deposition of particles, such as the produced sulfur, from the tip area. Subsequently, more electrolyte solution was injected until the outer casing was full. Epoxy was immediately applied to seal the outer casing completely. When the epoxy was air dried, the outer surface of the H_2S microsensor was painted black to avoid or decrease the degradation of hexacyanoferrate under ultraviolet light or natural light (Asperger, 1952). Note that the very tip with silicone membrane should not be painted. This is to avoid reaction between the paint and silicone. If storage was required, the H_2S microsensor should be kept in the dark.

4.3.2 Evaluation

Two processes, polarization and calibration, were used to evaluate the H_2S microsensor fabricated by the above-mentioned procedures. Parameters such as response time (the time the H_2S microsensor reached 90% of the limiting current upon the H_2S concentration change), residual signals (or zero current, lowest current reading for the H_2S-free condition), sensitivity (slope of the calibration curvesthe difference between currents produced at different H_2S concentrations) and linearity of a calibration curve were obtained from these two processes.

During the polarization process, the H_2S microsensor was secured in a calibration chamber with its tip immersed in the DI water. It was connected to a picoammeter (PA2000, Unisense, Denmark). The connections were made in the following order: reference cathode to reference terminal, working anode to input terminal, guard anode to guard terminal. The polarization voltage was fixed at the

mass transfer region. Initially, the signal was very high but dropped very quickly within the first few minutes. Then it became smaller and smaller until a stable zero current was achieved, which fluctuated within ±1 pA.

A calibration test produced a calibration curve and other parameters, such as response time, sensitivity and residual current signal for a specific H_2S microsensor. The H_2S microsensors might be calibrated at different sulfide concentrations under different pH values. Environmental biofilms were usually at near neutral pH values (Yu 2000), therefore, we introduced the calibration processes under neutral pH conditions.

In a well-ventilated fume hood, Na_2S stock solution was prepared by adding $Na_2S \cdot 9H_2O$ into air-free DI water, which was purged with N_2. The methylene blue method was used to measure the actual sulfide concentration in the stock solution. Once the solid $Na_2S \cdot 9H_2O$ was completely dissolved, a series of H_2S standard solutions (*e.g.*, 0-400 μM) were prepared by transferring a certain amount of the Na_2S stock solution into the de-aerated pH 7.0 phosphate buffer. Then, the H_2S microsensor was dipped into the H_2S standard solution of different concentrations. The steady state current in each solution was recorded. Between measurements at different concentrations, the H_2S microsensor was rinsed with DI water. It was important that all of the above air-free steps were done as soon as possible to avoid the oxidation of sulfide in the stock solution and standard solution. The steady state currents versus H_2S concentrations would produce a calibration curve. When this H_2S microsensor was used to conduct biofilm measurements, H_2S concentrations could be read from the calibration curve if the

steady-state currents were measured. The response time, residual signal, sensitivity and the linearity of the calibration curve were used to evaluate the performance of the H_2S microsensor.

4.3.3 H_2S Measurements

The combined amperometric H_2S microsensor was used to measure H_2S concentrations in a MAB and a conventional biofilm. The MAB grew on a silicone membrane in an MABR, which was described in Chapter 3. The conventional biofilm and wastewater sample were taken from the first stage of a four-stage, half-submerged rotating biological contactor system at the municipal wastewater treatment plant in the Town of Devon in Alberta, Canada. The wastewater was transferred to a flow cell in the lab, and its pH and temperature were then recorded. A small piece of plastic disk with the intact biofilm on was cut and put into the wastewater. The procedures of microsensor measurements for the two biofilms were summarized as follows: First, right before the measurements, the H_2S microsensor was polarized and calibrated. Then the H_2S microsensor was fastened onto a micromanipulator and connected to the picoammeter. The tip of the H_2S microsensor was advanced into the biofilm through the movement of the micromanipulator to measure the current signal change at different locations within the biofilms. The surface of the biofilm was observed under the horizontal stereomicroscope. The biofilm thickness was calculated according to the distance traveled by the micromanipulator. The concentration profiles of H_2S along the biofilm depth were obtained after the

microsensor measurements. Finally, after the measurements, the H_2S microsensor was again calibrated to check whether there was any change in the calibration curves. No significant changes in the calibration curves were observed.

4.4 Results and Discussion

4.4.1 Performance and characteristics of the H_2S microsensor

Good performance of the microsensor is indicated by a low zero current, high sensitivity, narrow signal drift, short response time and long lifetime. H_2S concentrations were linearly related to the current within the investigated range from 30 μM (1.02 mg L^{-1}) to 600 μM (21.40 mg L^{-1}) H_2S. Figure 4-4 illustrated one of the calibration curves. The R^2 in both of the calibration curves was higher than 0.99. One of the H_2S microsensors had a sensitivity of 0.93 pA μM^{-1} and the other had a sensitivity of 1.21 pA μM^{-1}, which was higher than the previously reported sensitivity (Kuhl, 1998; Jeroscheski, 1996). The zero currents of both H_2S microsensors were less than 5 pA. The response time depended on the change of H_2S concentration, and it could be less than 1 second upon a change of 100 μM. The lifetime depended on the usage frequency. It could be used for a few weeks up to 6 months.

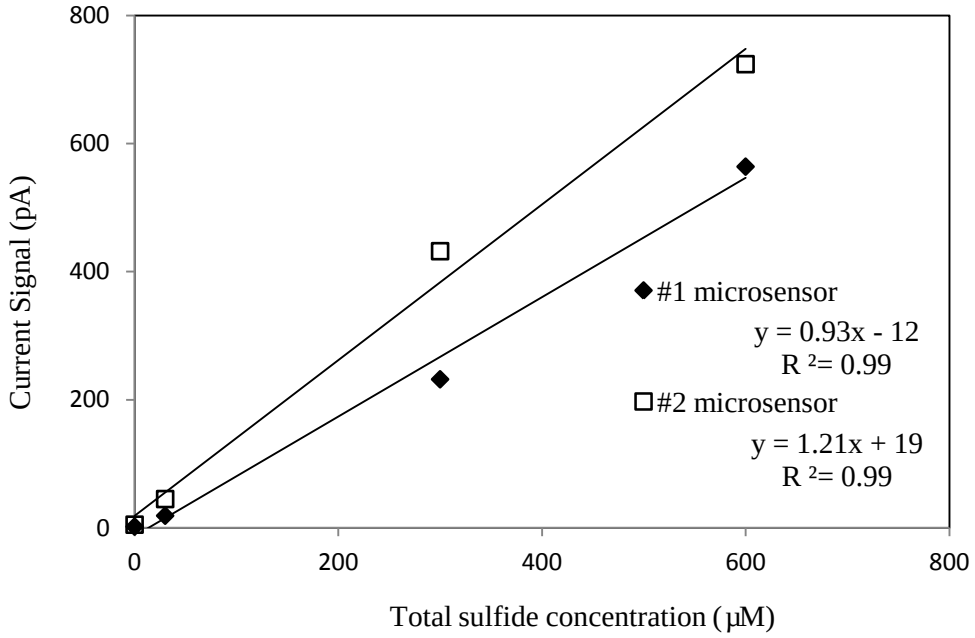

Figure 4-4 Calibration curve of a H_2S microsensor

The geometric size of the H_2S microsensor tip affected the performance of the H_2S microsensor. Generally, to minimize the disturbance of the biofilms, the microsensor with a smaller tip was preferred because the spatial resolution of the measurements is roughly twice the tip diameter of the sensor (Schreiber *et al*., 2008). Although a smaller tip was better, there is a need to balance the tip size and performance. The Clark-type design H_2S microsensor is robust, and the electromagnetic interference is shielded because the sensing electrode and the reference electrode were situated in an internal solution integrated into one body. In this study, if the tip was too small, it would have contained little electrolyte. According to Eq.4-2, the H_2S microsensor might have a short lifetime and large signal drifting if the tip was too small. The compromise tip size of this H_2S

microsensor was 15~30 μm in diameter (Jeroscheski, 1996). The microsensor tip contains the following components: working anode tip, guard anode tip, silicone membrane, electrolyte and glass beads. According to the working principle of the Clark-type H_2S microsensor, the geometric size of the tip region would affect the mass transfer coefficient and thereby affect the sensitivity. In this study, the tip diameter of working anode and guard anode was 1-2 μm and 1-5 μm, respectively. The silicone membrane depth was 10-20 μm. The distance between the membrane and working anode tip would influence response time and possible sulfur deposit at the working anode tip. The distance of 15 to 20 μm between the silicone membrane and working anode tip were proven to achieve better performance. The guard anode tip stayed behind the working anode tip in order to oxidize excess $Fe(CN)_6^{4-}$. The distance between the guard anode tip and working anode tip was 150-300 μm.

After the H_2S microsensor was used for several times or for a long time, depending on individual microsensor, an increase in polarization voltage might be required. According to Nernstian equation, the ratio of $Fe(CN)_6^{3-}/Fe(CN)_6^{4-}$ might drop so that its redox potential shifted to more negative values. According to Figure 4-1, i~E behavior would fall in the charge transfer limiting region, where currents would change remarkably with slight redox potential shift (Bard and Faulkner, 2001). By increasing the polarization voltage, currents could be again located in the mass transfer limiting region and stable current signals could be obtained.

4.4.2 H_2S concentration profile in biofilms

This H_2S microsensor was used for the measurements of conventional biofilm and MABs. A H_2S concentration profile along the depth of conventional biofilm measured using this H_2S microsensor was illustrated in Figure 4-5. The H_2S concentration profiles inside the MABs will be discussed in detail in Chapter 5 and 6.

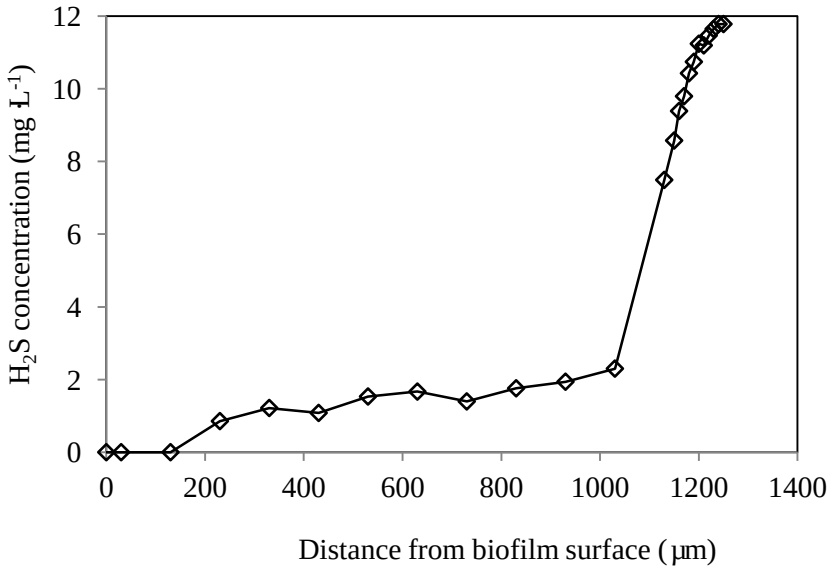

Figure 4-5 An illustration of H_2S concentration profile in a conventional biofilm. Note: distance of 0 μm indicates the biofilm surface.

Figure 4-5 shows that no H_2S was present or detected at the top of the biofilm (near to the biofilm surface). In this Figure, between 230 μm and 1030 μm, H_2S concentration increased gradually from 25.16 μM (10.86 mg L^{-1}) to 67.6 μM (2.3 mg L^{-1}). Then, the H_2S concentration increased drastically from 67.6 μM (2.3 mg L^{-1}) to 342.5 μM (11.7 mg L^{-1}) within the next 200 μm. These results demonstrated that the H_2S microsensor can quantitatively detect the change of H_2S concentration in a very narrow region of biofilms. The good performance of

the H_2S microsensor for the conventional biofilm and MABs means that the H_2S microsensor can be used to measure the change of H_2S concentrations from the lower to higher concentrations (shown in Figure 4-5) and from the higher to lower concentrations (shown in Chapter 5 and 6). Since H_2S is the principle end product of sulfate reduction process, the H_2S concentrations measured by the H_2S microsensor reflect the activities of SRB in the biofilms. These results also indicated that sulfate reduction occurred actively in the deep (bottom) section of the conventional biofilm and in the shallow (top) region near the bulk liquid-biofilm interface in MAB.

The H_2S concentrations measured by the H_2S microsensor revealed the distribution of sulfate reduction in the biofilms by means of measuring chemical species of H_2S as the end product of sulfate reduction. In addition, with the help from Dr. P. Fedorak in the Department of Biological Sciences at University of Alberta, the distribution of SRB in the same piece of the convential biofilm was inspected using the fluorescence *in situ* hybridization (FISH) techniques in combination with CLSM images. The results from FISH techniques, as shown in Figure 4-6, demonstrated that the SRB were abundant in the bottom and few near the biofilm surface of the conventional biofilm. These results from the H_2S microsensor measurements were consistent and in agreement with the results from the FISH techniques in combination with CLSM images.

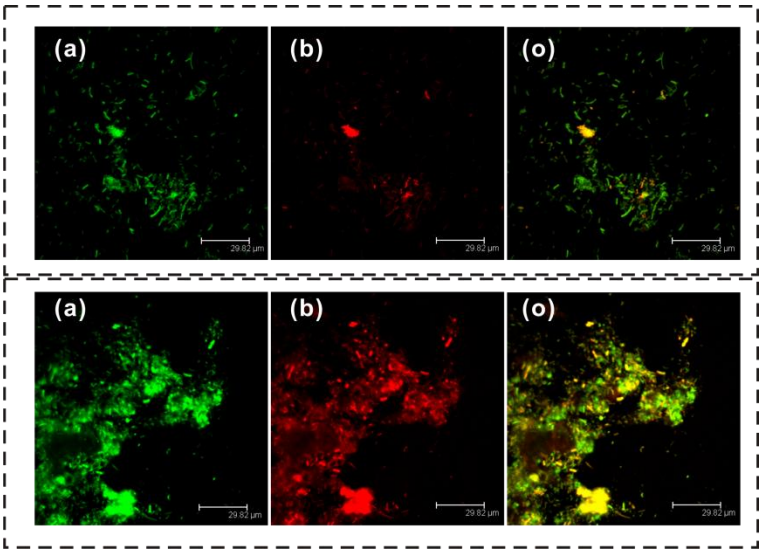

Figure 4-6 Representative CLSM images observed using FISH techniques for the conventional biofilm: The upper pictures- from the top surface of the biofilm sample; the bottom pictures –from the bottom of the biofilm sample. Note: (a) - all bacteria probe (EUB338); (b) - only SRB probe; and (o) - overlapped signal (a + b).

4.5 Conclusions

A Clark-type amperometric H_2S microsensor was successfully fabricated. This fabrication procedure can produce a H_2S microsensor with good performance. The H_2S microsensor with a relatively small tip -- contributing to high spatial resolution -- has a long lifetime. The geometric size of the H_2S microsensor's tip is important to the performance of the microsensor.

This H_2S microsensor could measure H_2S concentrations ranging from 0 to 600 µM (21.40 mg L^{-1}). Its sensitivity could reach 1.21 pA μM^{-1}, which was higher than the previously reported sensitivity. The zero currents could be less than 5 pA. The response time could be less than 1 second.

This H_2S microsensor can be used to measure the change of H_2S concentrations both from the low to high concentrations and from the high to low concentrations, which is very useful for the *in situ* measurement of H_2S concentration in terms of SRB's activity in a biofilm sample. The results from the H_2S microsensor measurements in conventional biofilms and MAB can be supplemented with the results from the FISH techniques.

References

Asperger, S. 1952. Kinetics of the decomposition of potassium ferrocyanide in ultra-violet light. Transactions of the Faraday Society. 48(7): 617-624.

Bard, A. J. and Faulkner, L. R. 2001. Electrochemistry methods - Fundamentals and application. John Wiley &Sons Inc.: 2nd edition.

Barton, L. L. 1995. Sulfate-reducing bacteria. New York: Plenum press

Boothman, C., Hockin, S., Holmes, D. E., Gadd, G. M. and Lloyd, J. R. 2006. Molecular analysis of a sulphate-reducing consortium used to treat metal-containing effluents. Biometals 19(6): 601-609.

De la Rosa, C. and Yu, T. 2006. Development of an automation system to evaluate the three-dimensional oxygen distribution in wastewater biofilms using microsensors. Sensors and Actuators B-Chemical. 113(1): 47-54.

Jeroschewski, P., Steuckart, C. and Kuhl, M. 1996. An amperometric microsensor for the determination of H_2S in aquatic environments. Analytical Chemistry. 68(24): 4351-4357

Kuhl, M., Steuckart, C., Eickert, G. and Jeroschewski, P. 1998. A H_2S microsensor for profiling biofilms and sediments: application in an acidic lake sediment. Aquatic Microbial Ecology. 15(2): 201-209.

Lewandowshi, Z. and Beyenal, H. 2007. Fundamentals of biofilm research. Baco Raton: CRC Press

Lu, R. and Yu, T. 2002. Fabrication and evaluation of an oxygen microsensor applicable to environmental engineering and science. J. Environ. Eng. Sci. (1): 225-235.

Okabe, S., Ito, T., Satoh, H. and Watanabe, Y. 2003. Effect of nitrite and nitrate on biogenic sulfide production in sewer biofilms determined by the use of microsensors. Water Science and Technology. 47(11): 281-288.

Okabe, S., Ito, T., Sugita, K. and Satoh, H. 2005. Succession of internal sulfur cycles and sulfur-oxidizing bacterial communities in microaerophilic wastewater biofilms. Applied and Environmental Microbiology. 71(5): 2520-2529.

Okabe, S., Itoh, T., Satoh, H. and Watanabe, Y. 1999. Analyses of spatial distributions of sulfate-reducing bacteria and their activity in aerobic wastewater biofilms. Applied and Environmental Microbiology. 65(11): 5107-5116.

Revsbech, N. P. and Jorgensen, B. B. 1986. Microsensors - their use in microbial ecology. Advances in Microbial Ecology. 9: 293-352

Santegoeds, C. M., Schramm, A. and de Beer, D. 1998. Microsensors as a tool to determine chemical microgradients and bacterial activity in wastewater biofilms and flocs. Biodegradation. 9(3-4): 159-167

Sawyer, C. N., Mccarty, P. L. and Parkin, G. F. 2003. Chemistry for Environmental Engineering and Science. McGraw-Hil Companies, Inc

Schreiber, F., Polerechy L. and de Beer, D. 2008. Nitric Oxide Microsensor for High Spatial Resolution Measurements in Biofilms and Sediments. 80(4): 1152-1158

Yu, T. and Bishop, P. L. 1998. Stratification of microbial metabolic processes and redox potential change in an aerobic biofilm studied using microsensors. Water Science and Technology. 37(4-5): 195-198

Yu, T. 2000. Stratification of microbial processes and redox potential changes in biofilms. University of Cincinnati. Doctor of Philosophy thesis.

Chapter 5

Microsensor Determination of Multiple Microbial Processes in an Oxygen-Based MAB

5.1 Introduction

MABRs have attracted increasing interests in recent years due to their flexibility to manipulate biofilm processes, low capital costs and high pollutant removal rate (Nerenberg, 2005). Up to date, most previous studies have focused on nitrification and denitrification in oxygen-based MABRs. These studies have demonstrated that the mechanisms of pollutant removal in MABs have been quite different from those in conventional biofilms due to the different diffusion mechanisms of substrates in the two kinds of biofilms (Lapara *et al*., 2006; Terada *et al*., 2003). Although sulfate reduction has been demonstrated to occur in conventional aerobic wastewater biofilms (Okabe *et al*., 1999; Okabe *et al*, 2005), whether it can coexist with nitrification and denitrification and how it affects nitrogen removal in an oxygen-based MAB have not been investigated yet.

Microsensor techniques have exhibited excellent superiority in *in situ* determination of chemical gradients and bacterial activity in microbial communities with minimal disturbance and high spatial resolution (Santegoeds *et al*., 1998; Revsbech, 2005). The microsensors with small tips, low detection limits, fast response times and high sensitivity are crucial to studying the internal structure and function of biofilms. Although microsensors techniques have been successfully used to determine *in situ* metabolic activities in microbial

communities (Santegoeds *et al*., 1998; Okabe *et al*., 2003; Okabe *et al*., 2005; de la Rosa and Yu, 2006), the microsensor types are very limited. For example, to the author's knowledge, amperometric H_2S microsensors for understanding sulfate reduction process have rarely been used in biofilm studies, especially in oxygen-MAB studies.

In this study, a laboratory-scale, oxygen-based MABR was run for 6 months to ensure pseudo-steady-state conditions. COD, O_2, pH, ORP, NH_4^+, NO_3^- and SO_4^{2-} in the bulk liquid were measured daily according to the standard analytical methods. To investigate the occurrence of simultaneous sulfate reduction and nitrogen removal in the MAB, O_2, pH, ORP, NH_4^+, NO_3^- and H_2S microsensors were fabricated and used to measure chemical gradients *in situ* in the oxygen-based MAB. Net specific consumption rates of NH_4^+, NO_3^-, O_2 and H_2S were estimated from the measured concentration profiles.

5.2 Materials and methods

5.2.1 Biofilm reactor operation

The experiments were conducted in MABR 1. The detailed description of the reactor was provided in Chapter 3. The reactor was constructed using acrylic board. The cover of the reactor had openings for microsensor measurements. During normal operations, openings were blocked using rubber stoppers. The reactor volume was about 0.9 L. The membrane module consisted of gas permeable, silicone tubing membranes. The membranes were parallel to each other, forming a sheet in the reactor. About 20 mL min^{-1} of pure oxygen flowed

through the silicone tubing membrane. Nitrogen gas was purged into the influent of synthetic wastewater to ensure the wastewater was oxygen-free and the oxygen gas in the bulk liquid was from membrane side and not from the wastewater. The synthetic wastewater consisted of COD, SO_4^{2-}, NH_4^+ and minor minerals (see Table 3-1 in Chapter 3). NO_3^- was absent in the influent. The influent flow rate of the wastewater was around 2 mL·min^{-1}. The MABR was operated at a temperature of 23 ± 1 ℃, at a pH of 7.6 ± 0.2, and at a recirculation rate of around 200 mL·min^{-1}.

5.2.2 Microsensors and microsensor measurements

A Clark-type O_2 microsensor with a tip diameter of approximately 15 μm was fabricated as described by Lu and Yu (2002). The oxygen microsensor was calibrated by a 3-point calibration in N_2, air-saturated and oxygen-saturated water. The detailed fabrication and calibration procedures were provided in Chapter 3. The Clark-type H_2S microsenor with tip diameters of approximately 25 μm was fabricated as described in Chapter 4. LIX-type microsensors for pH, NH_4^+ and NO_3^- with tip diameters of approximately 8 μm, and the ORP microsensor were fabricated, calibrated and used according to Yu (2000).

Microsensor measurements of O_2, pH, ORP, NH_4^+, NO_3^- and H_2S were directly taken in the MAB under actual growth conditions in the reactor on operating day 230. When all of the microsensors and the biofilm were ready for measurements, each microsensor was fastened onto a micromanipulator. The microsensor assembly and the MABR were put inside a Faraday cage to reduce

electrical noise. Immediately before and after the measurements, each microsensor was calibrated. Biofilm thickness was determined by the following procedure: a glass micropipette mounted on a micromanipulator was positioned on the surface of the biofilm. Then it was moved down until it touched the membrane surface. The movement was viewed through a horizontal dissection microscope. An illuminator was used to enhance the view of the micropipette's movement. Biofilm thickness was read from the distance travelled by the micromanipulator. In order to take measurements, the tips of microsensors were advanced into the biofilm from the openings on the cover of the reactor. Through the movement of the micromanipulator, readings were taken at intervals of 10-50 μm. The concentration of O_2, NH_4^+, H_2S and NO_3^- and pH along the biofilm depth were calculated using the equations obtained from calibration curves.

5.2.3 Estimation of production and consumption rates

Production and consumption rates of O_2, H_2S, NH_4^+ and NO_3^- were calculated using Fick's second law of diffusion. The details of this method have been reported previously (Meyer *et al*., 2001; Okabe *et al*., 1999; Lorenzen *et al*., 1998).

According to Fick's second law of diffusion including production and consumption rates (Lorenzen *et al*., 1998):

$$\partial C_{(z,t)} / \partial t = D_s \times \partial^2 C_{(z,t)} / \partial z^2 - R(z) + P(z) \qquad \text{(Eq.5-1)}$$

where $C_{(z,t)}$ is the concentration at time t and depth z, D_s is the diffusion coefficient. R is the consumption rate, and P is the production rate.

Assuming steady state,

$$\partial C_{(z,t)} / \partial t = 0 \qquad \text{(Eq.5-2)}$$

Therefore, Eq.5-1 can be reduced to

$$D_s \times \partial^2 C_{(z,t)} / \partial z^2 = R(z) - P(z) = A(z) \qquad \text{(Eq.5-3)}$$

where A(z) is the activity at depth z. A negative A(z) value reflects net production activity and a positive A(z) reflects net consumption activity. The concentration profiles are analyzed mathematically by means of a discrete version of Fick's first law (Meyer *et al*., 2001):

$$J_{(z+1/2\Delta z)} = D_s \frac{C_{(z+\Delta z)-}C_{(z)}}{\Delta z} \qquad \text{(Eq.5-4)}$$

where $J_{(z+1/2\Delta z)}$ is the flux at the depth between 2 data points, C is the concentration and Δz is the vertical distance between the 2 data points.

In this paper, the molecular diffusion coefficients of 1.38×10^{-5} cm^2 s^{-1} for NH_4^+, 1.23×10^{-5} cm^2 s^{-1} for NO_3^-, 2.09×10^{-5} cm^2/s for O_2 and 1.38×10^{-5} cm^2 s^{-1} for H_2S were used for calculations (Okabe, 2003). A flux profile was derived from the concentration profile using Eq.5-4. The flux profile was then used to calculate the activity profile by determining the first derivative:

$$A(z) = \frac{[J_{(z-1/2\Delta z)} - J_{(z+1/2\Delta z)}]}{\Delta z} \qquad \text{(Eq.5-5)}$$

Differentiation of the raw data in a concentration profile will often lead to a very noisy activity profile due to small variations in the data points. To increase the signal-to-noise ratio, an increasing number of data points (i.e. consecutive readings at equally spaced depths) to calculate the depth-specific activity was

used (Meyer *et al*., 2001). Most activity profiles were based on 7 data points (i.e. 3 readings above and 3 readings below the depth for which the activity was calculated). This resulted in smoothening of the activity profile, as the depth-specific activity was calculated as the average change in flux over the distance from 3Δ*z* above and below depth *x*. The formula for activity calculation based on 7 data points therefore is as follows:

$$A(z) = \frac{[J_{(z-2\frac{1}{2}\Delta z)} + J_{(z-1\frac{1}{2}\Delta z)} + J_{(z-\frac{1}{2}\Delta z)} - J_{(z+2\frac{1}{2}\Delta z)} - J_{(z+1\frac{1}{2}\Delta z)} - J_{(z+\frac{1}{2}\Delta z)}]}{6\Delta z} \qquad \text{(Eq.5-6)}$$

5.2.4 Chemical analytical methods

The detailed description of the analytical methods for the wastewater samples was shown in Chapter 3. DO, pH, NH_4^+ and ORP in the influent and effluent were measured regularly using corresponding commercial electrodes. COD was analyzed according to the standard methods (APHA *et al*., 1999). The concentration of SO_4^{2-} and NO_3^- in the influent and effluent were determined periodically using ion chromatography (Dionex ICS-2000). The samples for SO_4^{2-} and NO_3^-were filtered through a 0.45 μm membrane filter and stored in the refrigerator at 4 ℃ for up to two weeks before analysis.

5.3 Results and discussions

Reactor performance. The reactor performance in terms of sulfate, COD and ammonia removal in the reactor are shown in Figure 5-1, Figure 5-2 and Figure 5-3.

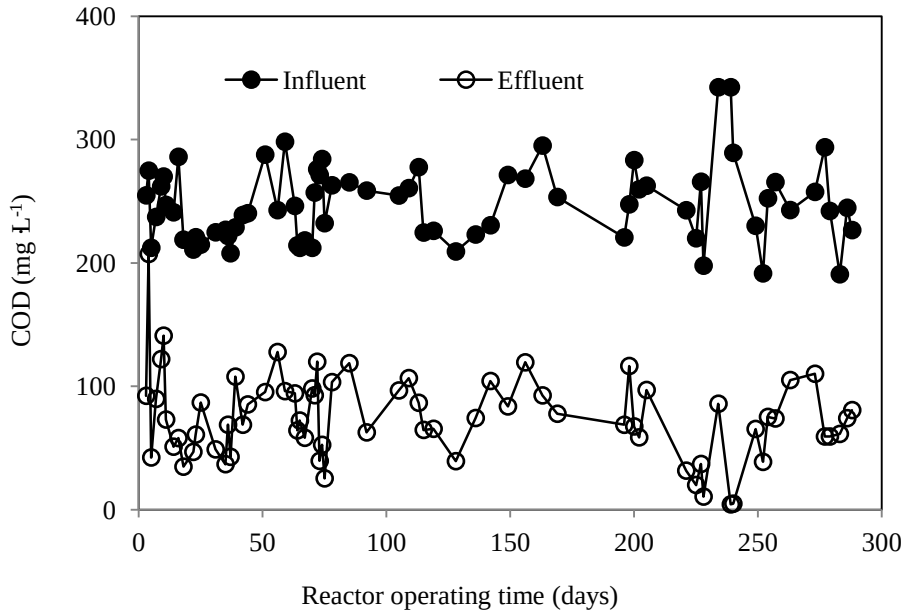

Figure 5-1 Reactor performance for COD removal in MABR 1

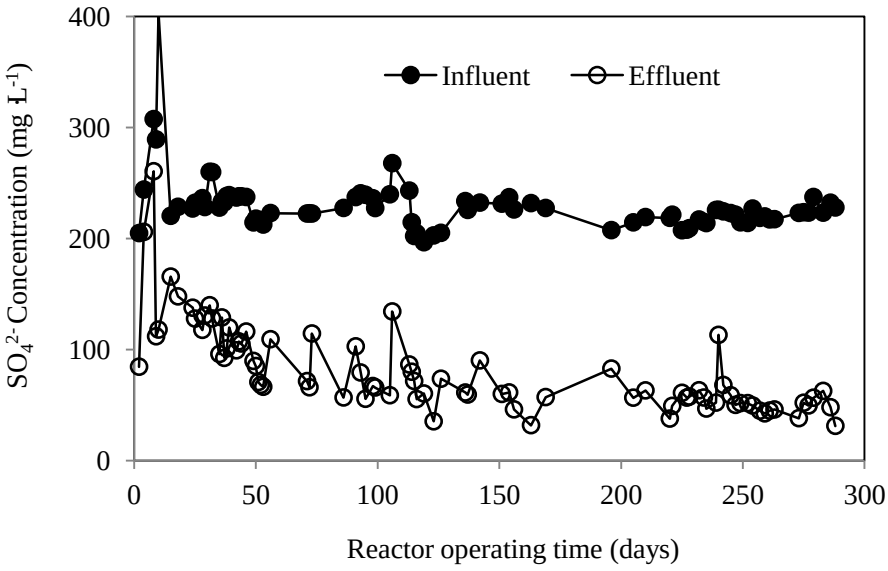

Figure 5-2 Reactor performance for sulfate removal in MABR 1

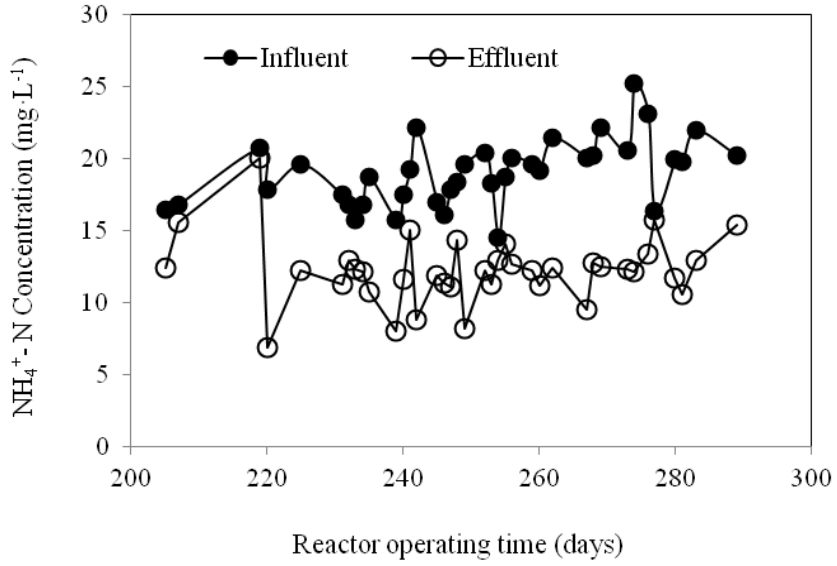

Figure 5-3 Reactor performance for ammonia removal in MABR 1

These figures of reactor performance indicate that the reactor was operated at pseudo-steady state before the microsensor measurements were taken. Although the removal rates of COD, sulfate and ammonia were low for typical biological reactors, they are expected because these reactors were designed for growing the type of biofilms to study the multiple microbial processes inside the biofilms but not for improving the treatment performance. The monitoring of these operating parameters was to ensure the occurrence of possible microbial processes such as sulfate reduction, oxidation of organic compounds, nitrification and denitrification inside the biofilms.

A note is some noticeable variability in the data presented in these figures. This variability might result from: 1) longer storage time of samples due to the limited avalilability of the analytical instruments at the time of sampling; 2) maintenance and cleaning of the reactors caused the errors. The magnitude and

impact of these errors was determined to be minimal because these isolated events occurred at specific days and these errors were later eliminated by shortening the sample storage time and maintaining proper operating conditions.

Microsensor measurements. Figure 5-4 shows the pseudo-steady-state profiles of O_2, pH, ORP, NH_4^+, NO_3^- and H_2S along the biofilm depth measured *in situ* using the microsensors. Figure 5-5 shows the estimated net specific consumption and/or production rates of O_2, NH_4^+, NO_3^- and H_2S on the basis of profiles draw in Figure 5-4. The O_2 profile is used to identify the oxic and anoxic zone within the biofilm. The H_2S profile is used to study the sulfate reduction, in terms of sulfate-reducing activity inside the biofilm. The pH profile shows pH change within the biofilm and is also necessary for the determination of H_2S concentration due to the relationship of H_2S concentration with pH. The profiles of ammonia and nitrate are used to investigate nitrification and denitrification inside the biofilm. The ORP profiles reveal redox potential changes inside the biofilm. The results show that in the anoxic zone, located from the interface between biofilm and bulk liquid to about 550 μm below the interface, both sulfate reduction and denitrification occurred. High levels of sulfate-reducing activity (H_2S production rates around 0.27 mg L^{-1} s^{-1}) were found in a narrow band about 400 to 450 μm below the interface. Below the anoxic zone, oxygen was available and an aerobic zone was present. H_2S was oxidized in aerobic zone. High H_2S oxidation activity occurred in around 550-700 μm below the biofilm-liquid interface, which was located just below the sulfate reducing zone. High ammonia consumption at around 500-600 μm and nitrate production in oxic zone,

indicating nitrification. High oxygen consumption rates (0.34 mg L^{-1} s^{-1}) indicating aerobic oxidation occurred in around 750-900 μm below the interface. Along the entire biofilm depth, the pH changed slightly (within 0.1 units). Near the interface of the aerobic and anoxic zones, there was a large redox potential change.

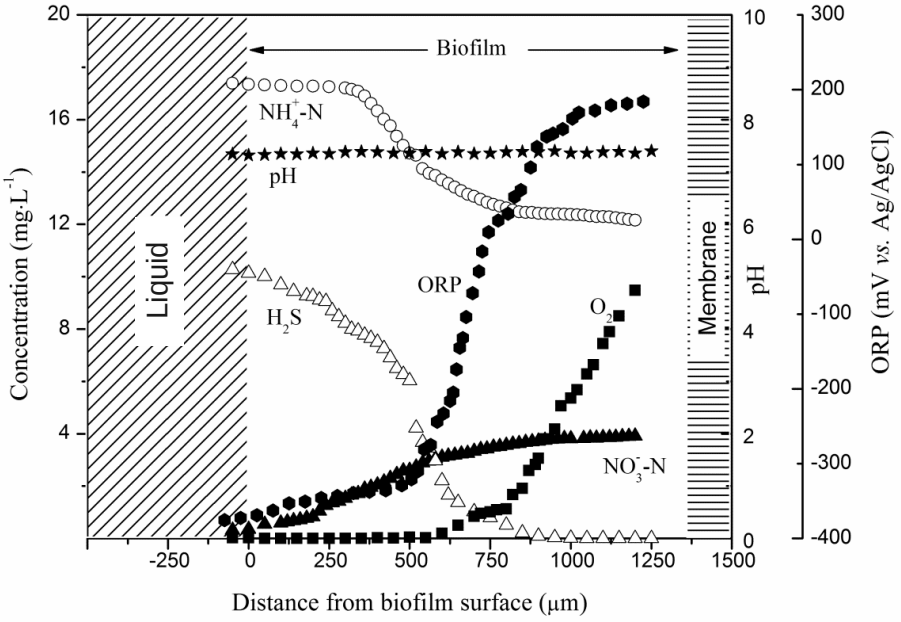

Figure 5-4 Profiles of O_2, pH, ORP, NH_4^+, NO_3^- and H_2S in a piece of MAB. The interface between the biofilm and bulk liquid is indicated by depth of 0 μm.

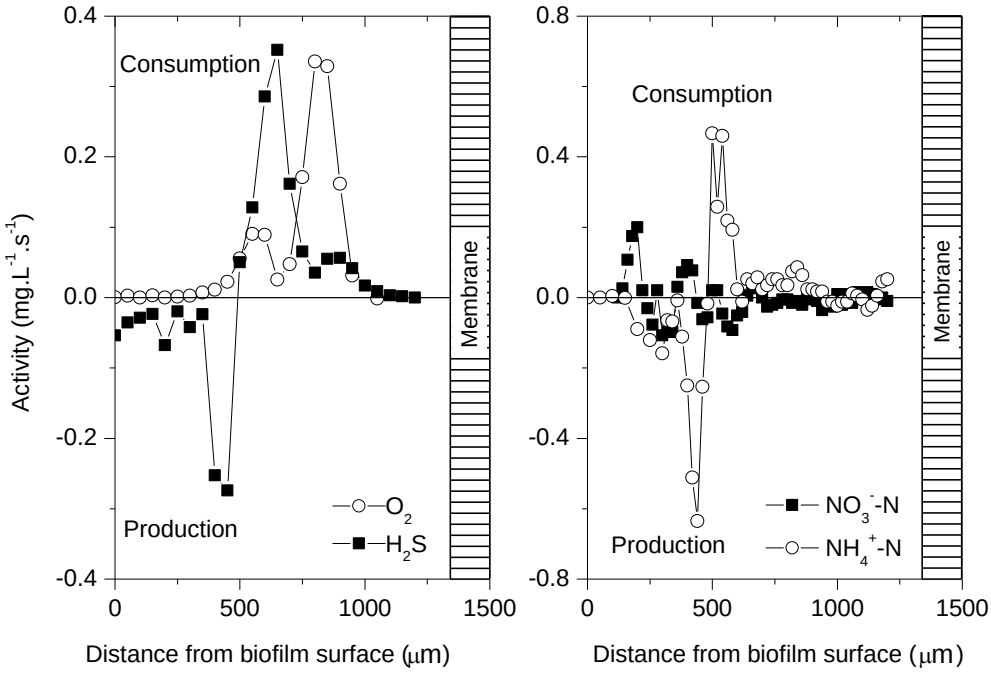

Figure 5-5 The net specific consumption and production rates of ammonia, nitrate, H_2S and O_2 in the MAB. The interface between the biofilm and bulk liquid is indicated by depth of 0 μm.

5.4 Conclusions

This study revealed simutaneous multiple processes in a piece of MAB. Using microsensor techniques, a stratification of multiple microbial processes was found. Sulfate reduction and denitrification occurred near the bulk liquid-biofilm interface. Nitrification and sulfide oxidation existed in the middle of MAB. Aerobic oxidation was present near the membrane.

References

APHA, AWWA and WEF. 1999. Standard methods foor the examination of water

and wastewater. 20th edition. American Public Health Association. Washington D.C.

Jeroschewski, P., Steuckart, C. and Kuhl, M. 1996. An amperometric microsensor for the determination of H_2S in aquatic environments. Analytical Chemistry, 68(24): 4351-4357.

Kuhl, M., Steuckart, C., Eickert, G. and Jeroschewski, P. 1998. A H_2S microsensor for profiling biofilms and sediments: application in an acidic lake sediment. Aquatic Microbial Ecology, 15(2): 201-209.

LaPara, T. M., Cole, A. C., Shanahan, J. W. and Semmens, M. J. 2006. The effects of organic carbon, ammoniacal-nitrogen, and oxygen partial pressure on the stratification of membrane-aerated biofilms. Journal of Industrial Microbiology and Biotechnology, 33(4): 315-323.

Lorenzen, J., Larsen L.H., Kjaer T. and Revsbech N. 1998. Biosensor determination of the microscale distribution of nitrate, nitrate assimilation, nitrification, and denitrification in a diatominhabited freshwater sediment. Applied and Environmental Microbiology, 64 (9): 3264-3269

Lu, R. and Yu, T. 2002. Fabrication and evaluation of an oxygen microsensor applicable to environmental engineering and science. Journal of Environmental Engineering and Science, (1): 225-235.

Meyer, R.L., Kjar T., Revsbech N.P. 2001. Use of NOx- micorsensors to estimate the activity of sediment nitrification and NOx- consumption along an estuarine salinity, nitrate, and light gradient. Aquatic Microbial Ecology, 26: 181-193.

Nerenberg, R. 2005. Membrane biofilm reactors for water and wastewater treatment. A Seminar on advances in water and wastewater treatment, Borchardt Conference, Ann Arbor, Michigan, February 23-25.

Okabe, S., Ito, T. and Satoh, H. 1999. Analyses of spatial distribution of sulphate-reducing bacteria and their activity in aerobic wastewater biofilms. Applied Microbiology and Biotechnology, 65(11): 5107-5116.

Okabe, S., Ito, T. and Satoh, H. 2003. Sulfate-reducing bacterial community structure and their contribution to carbon mineralization in a wastewater biofilm growing under microaerophilic conditions. Applied Microbiology and Biotechnology , 63(3): 322-334.

Okabe, S., Ito, T., Sugita, K. and Satoh, H. 2005. Succession of internal sulfur cycles and sulfur-oxidizing bacterial communities in microaerophilic wastewater biofilms. Applied and Environmental Microbiology, 71(5): 2520-2529.

Revsbech, N. P. 2005. Analysis of microbial communities with electrochemical microsensors and microscale biosensors. Environmental Microbiology, 397: 147-166.

Santegoeds, C. M., Schramm, A. and de Beer, D. 1998. Microsensors as a tool to determine chemical microgradients and bacterial activity in wastewater biofilms and flocs. Biodegradation, 9(3-4): 159-167.

Satoh H., Ono H., Rulin B., Kamo J., Okabe S., and Fukushi K. 2004. Macroscale and microscale analyses of nitrification and denitrification in biofilms

attached on membrane-aerated biofilm reactors. Water Research, 38: 1633-1641

Terada, A., Hibiya, K., Nagai, J., Tsuneda, S. and Hirata, A. 2003. Nitrogen removal characteristics and biofilm analysis of a membrane-aerated biofilm reactor applicable to high-strength nitrogenous wastewater treatment. Journal of Bioscience and Bioengineering, 95(2): 170-178.

Yu, T. 2000. Stratification microbial process and redox potential changes in biofilms. University of Cincinnati. Doctor of Philosophy thesis.

Chapter 6

Effects of COD/SO_4^{2-} and COD/NH_4^+-N Ratios on Multiple Microbial Processes in Oxygen-Based MAB

6.1 Introduction

Simultaneous nitrification and denitrification processes within oxygen-based MABs have been investigated (Cole *et al*.., 2002; Terada *et al*., 2003; Cole *et al.*, 2004; Satoh *et al*., 2004). However, there is little information on sulfate reduction within the oxygen-based MABs, although several studies have demonstrated the occurrence of sulfate reduction in conventional wastewater biofilms under bulk-phase "aerobic" conditions (Kuhl and Jorgensen, 1992; Santegoeds *et al*., 1998; Okabe *et al*., 1999; Ito *et al*., 2002; Ito *et al*., 2002). Sulfate reduction has been reported to contribute up to 45% of carbon mineralization in conventional wastewater biofilms (Okabe *et al*., 2003). Bhagat *et al*. (2004) reported that metal toxicity could be controlled by the sulfate reduction process. Nevertheless, sulfate reduction could be a concern due to the production of the highly reactive and corrosive H_2S (Jahani *et al*., 2001).

Physiochemical and ecological roles of complex microbial communities in wastewater biofilms depend on the availability of electron acceptors and other environmental and operational factors. Conventional biofilms are fundamentally different from oxygen-based MABs due to different mass transfer mechanism within the biofilms: co-diffusion of gas and liquid substrates for conventional

biofilms and counter-diffusion of gas and liquid substrates for oxygen-based MABs. Therefore, observations of microbial activities for conventional biofilms are not necessarily applicable to the oxygen-based MABs. However, a limited number of studies performed to characterize oxygen-based MAB indicate that these biofilms might be affected by the same reactor conditions although the response to the input might be distinctly different from conventional biofilms. For example, Cole (2004) demonstrated that proper COD/NH_4^+-N ratios have a significant impact on the occurrence of simultaneous nitrification and denitrification in oxygen-based MABs in non-sulfate wastewater. In the same paper, using O_2 microsensor and molecular techniques, it was reported that the response of oxygen penetration depth, nitrification and denitrification to the COD/NH_4^+-N ratios was quite different in oxygen-based MABs from conventional biofilms.

In this study, six types of microsensors, H_2S, O_2, ammonia, nitrate, pH and ORP microsensors were fabricated in our lab and used to investigate the effect of COD/SO_4^{2-} and COD/NH_4^+-N ratios on multiple microbial processes in an oxygen-based MAB. Although microsensors techniques have been successfully used to determine *in situ* metabolic activities in microbial communities (Santegoeds *et al*., 1998; Okabe *et al*., 2003; Okabe *et al*., 2005; de la Rosa and Yu, 2006), the microsensor types are very limited. For example, to the author's knowledge, amperometric H_2S microsensors for understanding sulfate reduction process have not been used in oxygen-based MAB studies. After microsensor measurements, the production rates and consumption rates of H_2S, O_2, ammonia

and nitrate were calculated to compare the multiple microbial activities within oxygen-based MABs grown under different COD/SO_4^{2-} and COD/NH_4^+-N ratios. The COD/SO_4^{2-} ratios of 1 and 2 were chosen to investigate the effect of COD/SO_4^{2-} on multiple microbial processes in oxygen-based MAB. The COD/NH_4^+-N ratios of 4 and 10 were selected to investigate the effect of COD/NH_4^+-N on multiple microbial processes in oxygen-based MAB.

6.2 Experimental Methods

Biofilm reactor operation. The experiments were conducted in MABR1. The detailed information such as size dimensions, fabrication and schematic diagram of MABR1 were presented in Chapter 3. The reactor was inoculated with activated sludge collected from the anaerobic digester at Gold Bar Wastewater Treatment Plant in Edmonton. After start-up of the reactor, about 20 mL·min^{-1} of pure O_2 flowed through the silicone membrane. Nitrogen gas was pursed into the influent of synthetic wastewater to ensure the synthetic wastewater was O_2-free. NO_3^- was absent in the influent. Once the oxygen-based MABs were well developed and reached pseudo-steady state, the chemical gradients inside the biofilms were measured using microsensors. Thereafter, the operational conditions were changed to study the effect of COD/SO_4^{2-} ratio and COD/NH_4^+-N ratio on the occurrence of multiple microbial processes within oxygen-based MABs.

Table 6-1 shows the designed operational conditions in bulk liquid phase for studying the effect of COD/SO_4^{2-} ratio on the occurrence of multiple microbial

processes within the oxygen-based MAB. The COD/SO_4^{2-} ratio of 1 and 2 were studied. During these two runs, other operational conditions were kept the same except the SO_4^{2-} concentration. The COD concentration was chosen to represent a typical weak level of COD commonly found in wastewater. The chosen COD/SO_4^{2-} ratios were based on the fact that the theoretical COD/SO_4^{2-} ratio for total sulfate reduction is 0.67 but actual COD/SO_4^{2-} ratio in most wastewater is higher than 1 (Freese and Stuckey, 2004). In addition, Freese and Stuckey (2004) demonstrated that sulfate reduction would be suppressed if the COD/SO_4^{2-} ratio is larger than 2 in the bulk liquid.

Table 6-1 Operational conditions for studying the effect of COD/SO_4^{2-} ratio

Parameters	Biofilm growth conditions	
	Stage 1	Stage 2
COD (mg L^{-1})	250	250
$SO4^{2-}$ (mg L^{-1})	250	125
COD/SO_4^{2-}	**1**	**2**
NH_4^+-N (mg-N/L)	25	
pH	7.2	
DO (mg L^{-1})	<0.5	
ORP (mV)	-150 to -250	
Temperature (°C)	22	

Table 6-2 shows the operational conditions in bulk liquid phase for studying the effect of COD/NH_4^+-N ratio on the occurrence of multiple microbial processes within the oxygen-based MAB. The COD/NH_4^+-N ratio of 4 and 10 were studied. During these two runs, the other operational conditions were kept the same except for the NH_4^+-N concentration. The chosen COD/NH_4^+-N ratios were based on the fact that the theoretical COD/NH_4^+-N ratio for total denitrification is around 5 and high COD concentrations are beneficial for denitrification but harmful for nitrification (Cole, 2004). In addition, in most conventional wastewater treatment processes, the COD/NH_4^+-N ratio of 4 was demonstrated to have best performance for nitrification and denitrification, and nitrification disappeared when the COD/NH_4^+-N ratio reached 10 (Cole, 2004).

Table 6-2 Operational conditions for studying the effect of COD/NH_4^+-N ratio

Parameters	Biofilm growth conditions	
	Stage 1	Stage 3
COD (mg ŁL^{-1})	250	250
$NH4^+$-N (mg-N/L)	25	62.5
COD/N	**10**	**4**
SO_4^{2-} (mg ŁL^{-1})	275	
pH	7.2	
DO (mg ŁL^{-1})	< 0.5	
ORP (mV)	-150 to -250	
Temperature (ºC)	22	

Standard chemical analysis. During regular reactor run and microsensor measurements, bulk reactor conditions were monitored daily. The detailed information on the methods of chemical analysis was provided in Chapter 3. DO concentration, pH and ORP in the influent and effluent were measured using commercial electrodes and meters. COD was analyzed according to the standard methods (APHA *et al*., 1999) using Digital Reactor Block 200 digester (Model: DRB 200, Hatch). The concentration of SO_4^{2-}, NO_2^- and NO_3^- in the influent and effluent were determined periodically using ion chromatography (Model: ICS-2000, Dionex).

Microsensors and microsensor measurements. A Clark-type O_2 microsensor with tip diameter of approximately 15 μm was fabricated as described by Lu and Yu (2002). The oxygen microsensor was calibrated by a 3-point calibration in N_2, air-saturated and oxygen-saturated water. The detailed fabrication and calibration procedures were provided in Chapter 3. The Clark-type H_2S microsenor with tip diameter of approximately 25 μm was fabricated as described in Chapter 4. LIX-type microsensors for pH, NH_4^+ and NO_3^- with tip diameters of approximately 8 μm, and the ORP microsensor were fabricated, calibrated and used as described in Chapter 3.

When all of the microsensors and the biofilms are ready, microsensor measurements were directly taken in the MABR under actual growth conditions. The initial set of microsensor measurements of O_2, pH, ORP, NH_4^+, NO_3^- and H_2S were directly taken at day 285 (the reactor operating day). Immediately before and after the measurements, each microsensor was calibrated. During measurements,

each microsensor was mounted on a micro-manipulator (Model M3301R, World Precision Instruments Inc, USA). The microsensor tip was advanced into the biofilm from the openings in the cover of the reactor. When the tip touched the biofilm surface, the microsensor penetrated the biofilm through the movement of the micromanipulator at intervals of 10 to 50 μm. The movement was viewed through a horizontal dissection microscope (Model: Stemi SV11, Carl Zeiss, Jena, Germany). An illuminator was used to enhance the view of movement area.

After one set of microsensor measurements, the reactor conditions were changed by decreasing the SO_4^{2-} concentration according to Table 6-1. First, the biofilm was left to grow one or two days. Then, the microsensor measurements were taken again. The reactor conditions were finally returned to the original conditions. The biofilm was again left to grow one or two days and then the reactor conditions were changed by increasing NH_4^+-N concentration according to Table 6-2. Finally, the biofilm was left to grow one or two more days and the microsensor measurements were subsequently taken.

Calculation of consumption and production rates. The detailed information about the calculation of consumption and production rates was given in Chapter 5.

Microscopy Observation. After completing investigating the effects of operating conditions on the occuurence of multiple microbial processes, the biofilm samples were observed under a SEM. The detailed sample preparation was introduced in Chapter 3.

6.3 Results and Discussion

Reactor performance. The reactor operating data (shown in Chapter 5) demonstrated that the reactor reached pseudo-steady state before the first set of microsensor measurements. Table 6-3 summarizes the reactor performance under the pseudo-steady state. This reactor was designed not to evaluate the performance of MABR but to provide the best reactor configurations for *in situ* measurements by using microsensors. Therefore, the removal rates in Table 6-3 should not be taken as indications of the best performance of MABR. Nevertheless, they did reflect the incident of microbial processes. From Table 6-3, the SO_4^{2-} removal rate was 65 (±15) %, which indicated the occurrence of sulfate reduction. The NH_4^+-N removal rate was 34 (±15) %, which indicated the occurrence of nitrification.

Table 6-3 Reactor performance under pseudo-steady state

Main constituents	COD (mg L^{-1})	SO_4^{2-} (mg L^{-1})	NH_4^+-N (mg L^{-1})
Effluent concentration	75 (±34)	82 (±39)	15 (±5)
Removal rate (%)	70(±13)	65 (±15)	34 (±15)

Microscopy observation. Figure 6-1 shows the SEM photographs for a piece of biofilm sample (A), magnification photo for the biofilm near the membrane (B), magnification photo for the middle of the biofilm (C) and magnification photo for the biofilm near the bulk liquid (D) in MABR1. The shape of the biofilm in Figure 1 (A) was curved. This might result from the

shrinkage of the sample during the treatment. Figure 1 (A) demonstrated quite different structure from the membrane side to the bulk liquid side: fluffy near the membrane but clay-like near the bulk liquid. This might be due to the high gas pressure from the membrane but no or little gas pressure from the bulk liquid side. Figure 6-1 (B), (C) and (D) showed that microorganisms were immersed in compact extracellular polymer slimes. High cell density was present near the bulk liquid and few cells near the membrane, resulting in porous structure near the membrane and denser structure near the bulk liquid. The explanation might be that the high concentration of COD and nutrients near the biofilm-liquid interface is more important for cell growth, leading to high cell density.

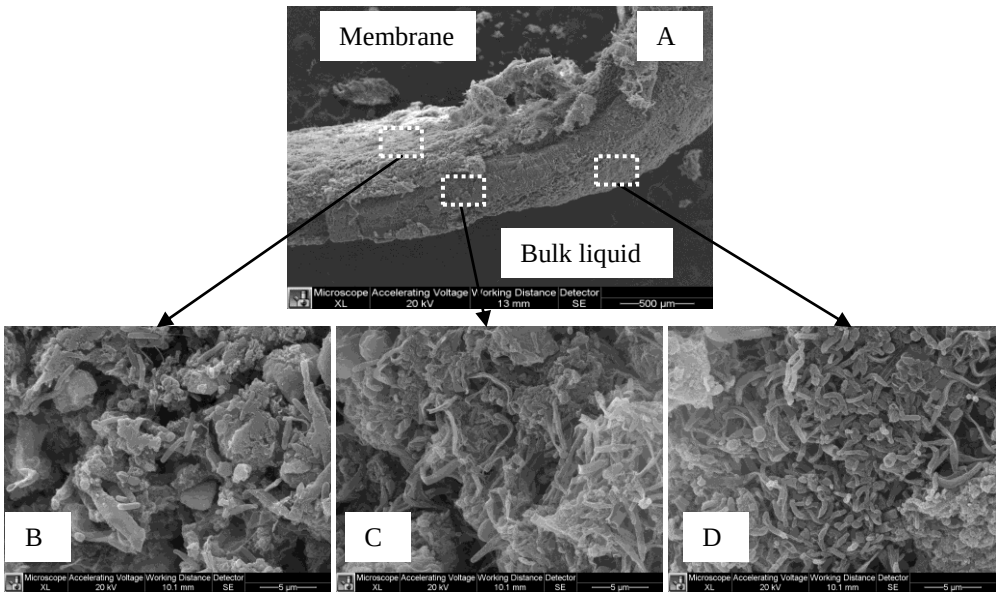

Figure 6-1 SEM photograph for a piece of biofilm sample (A); magnification photo for the biofilm section near the membrane (B); magnification photo for the middle of the biofilm (C); magnification photo for the biofilm section near the biofilm-liquid interface (D)

Microsensor measurements. Compared with previous studies (Okabe *et al*., 1999; Ito *et al*., 2002), microsensor measurements for *in situ* metabolic activity in this study have been improved in that the measurements were performed under actual growth conditions in the MABR. Concentration profiles of O_2, H_2S, NH_4^+, NO_3^-, pH and ORP are shown in Figure 6-2 for the oxygen-based MABs grown under COD/SO_4^{2-} ratio of 1 and COD/NH_4^+-N ratio of 10, Figure 6-4 for the oxygen-based MABs grown under COD/SO_4^{2-} ratio of 2 and COD/NH_4^+-N ratios of 10, and Figure 6-6 for the oxygen-based MABs grown under COD/SO_4^{2-} ratio of 1 and COD/NH_4^+-N ratios of 4. Consumption and production rates of O_2, H_2S, NH_4^+ and NO_3^- are shown in Figure 6-3 for the oxygen-based MABs grown under COD/SO_4^{2-} ratio of 1 and COD/NH_4^+-N ratios of 10, Figure 6-5 for the oxygen-based MABs grown under COD/SO_4^{2-} ratio of 2 and COD/NH_4^+-N ratios of 10, and Figure 6-7 for the oxygen-based MABs grown under COD/SO_4^{2-} ratio of 1 and COD/NH_4^+-N ratios of 4. Table 6-4 and 6-5 show the comparison of the activity of consumption and production.

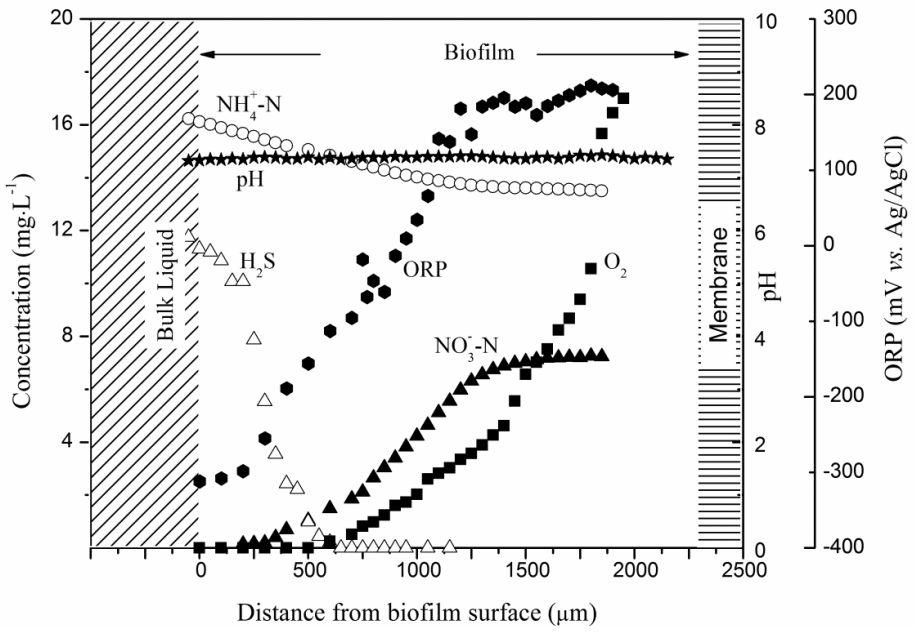

Figure 6-2 Profiles within oxygen-based MAB grown under COD/SO_4^{2-} ratio of 1 and COD/NH_4^+-N ratios of 10

From Figure 6-2, the O_2 concentration profile revealed that O_2 penetrated from the gas permeable membrane, and was gradually consumed and then depleted at about 500 μm below the biofilm/bulk liquid interface, indicating oxic and anoxic zone in the MAB. The H_2S concentration profile showed that H_2S was present in the whole anoxic zone (500 μm below the biofilm/bulk liquid interface) until at 600 μm below the biofilm/bulk liquid interface. From the bulk liquid to the membrane, ammonia concentration decreased and nitrate concentration increased, which indicated nitrification. Along the entire biofilm depth, pH changed slightly (within 0.2 unit). Across the biofilm from the bulk liquid to the membrane, the redox potential changes from -312 to +212 mV (Vs. Ag/AgCl).

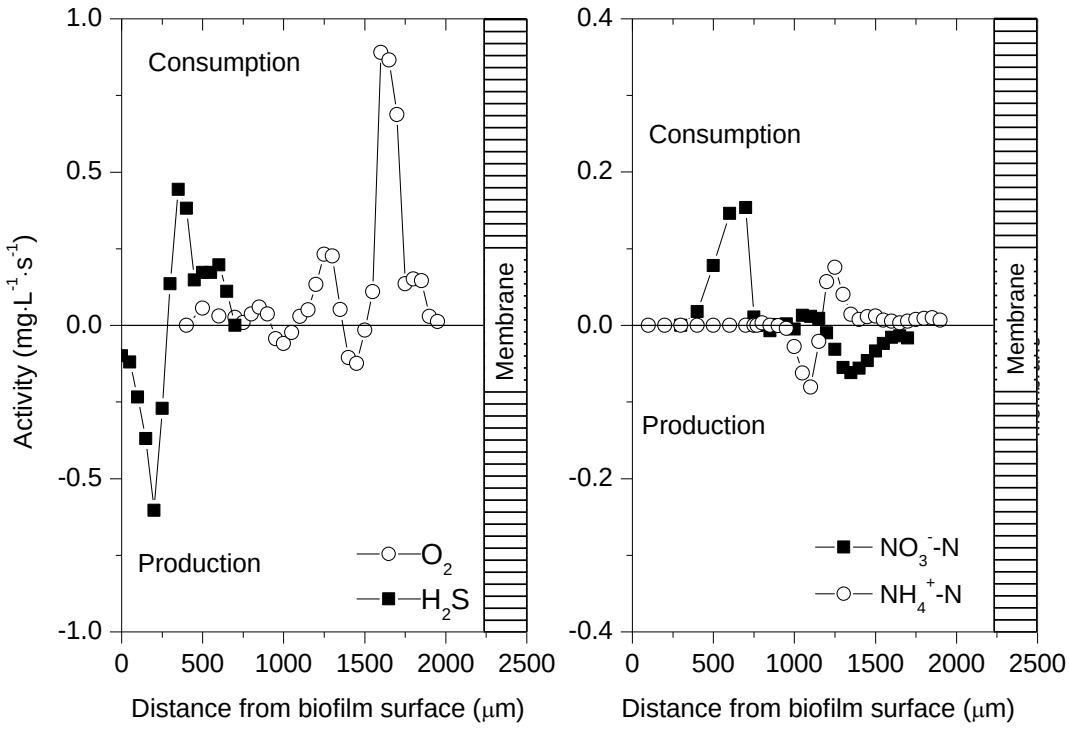

Figure 6-3 Production and consumption rates within oxygen-based MAB grown under COD/SO_4^{2-} ratio of 1 and COD/NH_4^+-N ratios of 10

The results from Figure 6-3 show that multiple microbial processes occurred simultaneously in an oxygen-based MAB growing under $COD/SO_4^2 = 1$ and COD/NH_4^+-N = 10. From the right figure in Figure 6-3, the maximal NH_4^+-N production rate was 0.08 mg L^{-1} s^{-1} at 1100 μm below the bulk liquid-biofilm interface and the maximal NH_4^+-N consumption rate was 0.08 mg L^{-1} s^{-1} at 1250 μm below the bulk liquid-biofilm interface. The maximal NO_3^--N consumption occurred at 600-700 μm below the bulk liquid-biofilm interface and the maximal NO_3^--N production at 1300-1400 μm below the bulk liquid-biofilm interface. The NH_4^+-N consumption and NO_3^--N production in the aerobic zone (shown in

Figure 6-2) indicated the presence of nitrification. The presence of NH_4^+-N production on oxic zone might be due to the ammonification of organic compounds, which is released when the dead cell was degraded. The NO_3^--N consumption indicated the presence of denitrification. From the O_2 rates in the left figure of Figure 6-3, a large peak near the membrane (1600-1650 μm below the bulk liquid- biofilm interface) indicated the oxidation of organic compounds occurred near the membrane where high oxygen concentrations were available. This might contribute to the degradation of COD resulting from aerobic heterotrophs. In the same curve, a relatively small peak (1200-1300 μm below the bulk liquid- biofilm interface) was present, which might be due to the oxygen utilization by nitrifiers. The maximal H_2S production occurred near the bulk liquid-biofilm interface (200 μm below the bulk liquid- biofilm interface) and the maximal H_2S consumption occurred at 350 μm below the bulk liquid - biofilm interface. The H_2S production indicated the presence of sulfate reduction and the H_2S consumption indicated the presence of sulfide oxidation.

Based on the data from the Figure 6-3, total consumption and production rates (area under the peak) were calculated. The results are shown in Table 6-4. Compared with other literatures (Hibiya *et al*., 2003; Okabe *et al*., 1999), more data on consumption and production rates of the multiple microbial processes were obtained, which will help expand the fundamental understanding of internal function of biofilms. The NH_4^+-N consumption rate and NO_3^--N consumption rate in this study was lower but the H_2S production rate was higher than the above references. This might imply the biofilm is beneficial for sulfate reduction but not

favorable for nitrification and denitrification even though the multiple microbial processes occurred simultaneously.

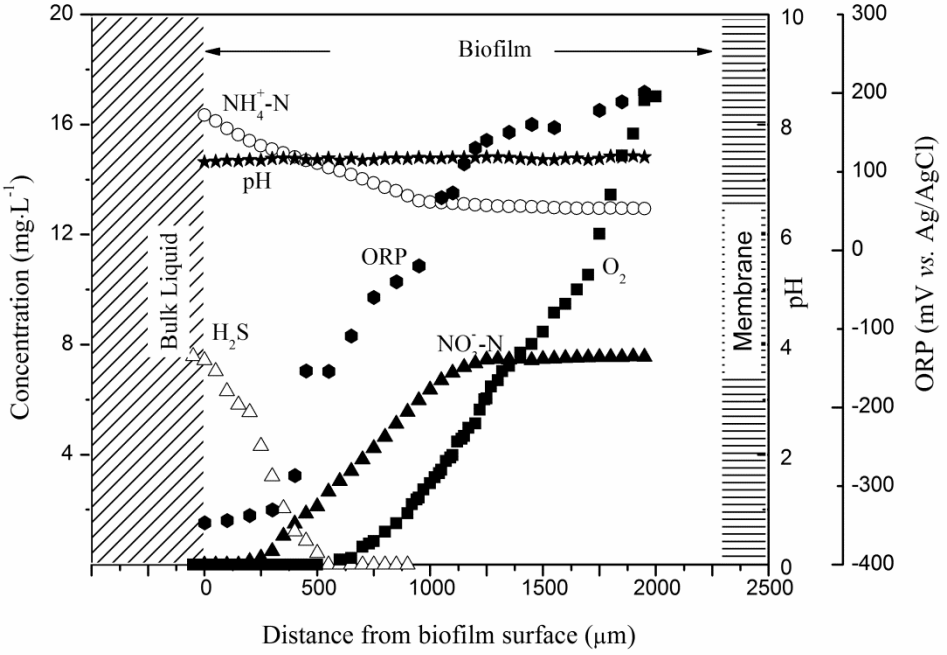

Figure 6-4 Profiles within oxygen-based MAB grown under COD/SO_4^{2-} ratio of 2 and COD/NH_4^+-N ratios of 10**.**

Compared with Figure 6-2, Figure 6-4 reveals the change of concentration profiles when the COD/SO_4^{2-} ratio was increased by decreasing the SO_4^{2-} concentration. Oxygen penetrated into the biofilm from the membrane and depleted at 500 μm below the bulk liquid-bioiflm, which is similar to that in Figure 6-2. H_2S concentration decreased from 7.43 mg $L^{-1,}$ which is much lower than 11.31 mg L^{-1} in Figure 6-2. H_2S penetration depth was 550 μm below the bulk liquid-bioiflm interface. This depth was near to the 600 μm H_2S penetration depth in Figure 6-2. This reflects smaller H_2S amount was produced but similar H_2S penetration depth was obtained when the SO_4^{2-} concentration was decreased.

The trend of NH_4^+-N concentration decrease and NO_3^- concentration increase was also found in Figure 6-4, which indicated the presence of nitrification.

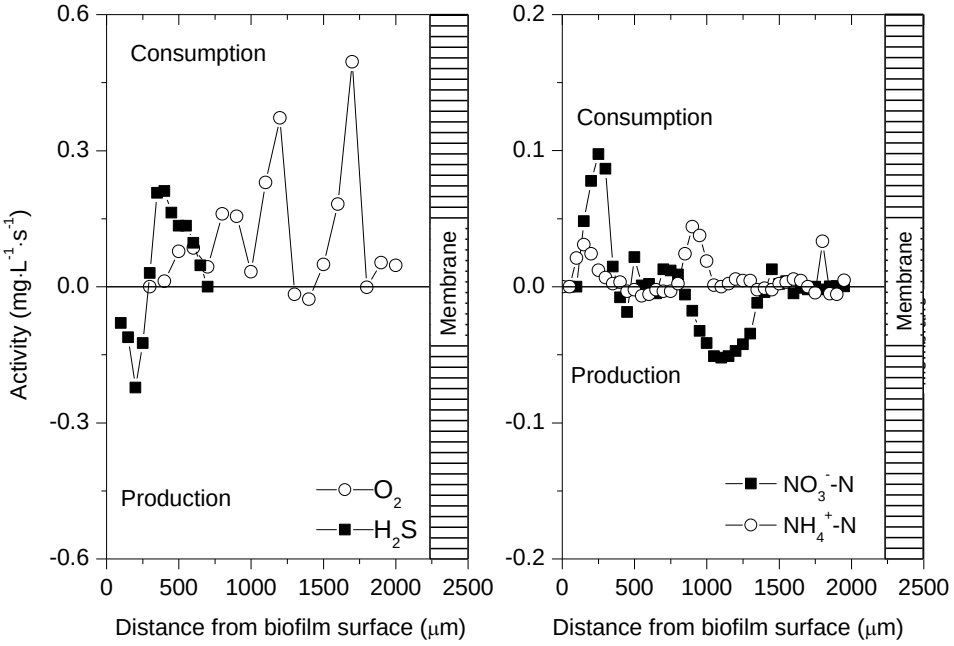

Figure 6-5 Production and consumption rates within oxygen-based MAB grown under COD/SO_4^{2-} ratio of 2 and COD/NH_4^+-N ratios of 10

Figure 6-5 shows that multiple microbial processes occurred simultaneously in an oxygen-based MAB growing under COD/SO_4^{2-} = 2 and COD/NH_4^+-N = 10. The maximal NH_4^+-N consumption rate was 0.04 mg L^{-1} s^{-1} and occurred at 900-950 μm (oxic zone). Another peak was present at 150 μm (anoxic zone) below the bulk liquid-biofilm interface. The NH_4^+-N consumption in anoxic zone might result from the presence of anaerobic ammonia bacteria. The maximal NO_3^--N consumption occurred at 250 μm below the bulk liquid-biofilm interface and the maximal NO_3^--N production was 0.05 mg L^{-1} s^{-1} and present at

1050-1200 μm below the bulk liquid-biofilm interface. The peak of NH_4^+-N consumption and NO_3^--N production in the oxic zone indicated that the decrease of the SO_4^{2-} concentration affected the maximal nitrifcation activity. For the O_2 rates, a large peak was present near the membrane (1700 μm below the bulk liquid- biofilm interface), which indicated the oxidation of organic compounds occurred near the membrane where high oxygen concentrations were available. In the same curve, a few relatively small peaks (600, 800 and 1200 μm below the bulk liquid- biofilm interface) were present, which might be due to the oxygen utilization of nitrification or the oxidation of other reducers such as sulfide. The maximal H_2S production occurred near the bulk liquid-biofilm interface (200 μm below the bulk liquid- biofilm interface) and the maximal H_2S consumption occurred at 350-400 μm below the bulk liquid- biofilm interface. The H_2S production indicated the presence of sulfate reduction and the H_2S consumption indicated the presence of sulfide oxidation. The peak of sulfide oxidation overlapped with O_2 consumption and NO_3^--N consumption. This indicated the sulfide might be oxidized by O_2 and NO_3^-.

Figure 6-3 and Figure 6-5 also showed a stratification of multiple microbial processes in the MAB. Sulfate reduction and denitrification was present near the bulk liquid-biofilm interface. Nitrification and sulfide oxidation occurred in the middle of bifilm. Aerobic oxidation existed near the membrane. This could provide previously unavailable bifilm data to future modelers.

Table 6-4 lists a comparison of consumption and production rates of O_2, H_2S, NH_4^+-N and NO_3^- for the two conditions: biofilm growing under COD/SO_4^{2-} ratios of 1 and 2.

Table 6-4 Comparison of total consumption and production rates for the MABs grown under COD/SO_4^{2-} ratio of 1 and 2

COD/SO_4^{2}	NH_4^+-N		NO_3^--N		H_2S	O_2
	Consumption	Production	Consumption	Production	Oxidation	Consumption
1	0.12	0.13	0.16	1.30	0.52	-
2	0.18	0.15	0.14	0.23	0.45	-
Other data sources	1.00[a]	-	1.17[b]	0.02[b]	-	1.69[b]

Note: The unit of total consumption and production rates is g-N m^{-2} d^{-1}. a - data reported by Hibiya *et al.*, 2003, and b - reported by Okabe *et al.*, 1999.

The results from Table 6-4 show that H_2S production rates decreased by 5.6 times when the ratio of COD/SO_4^{2-} was increased by 2 times. Note that the increase of the COD/SO_4^{2-} ratio was by decreasing the SO_4^{2-} concentration. Therefore, the higher ratio of COD/SO_4^{2-} ratio have less available electron acceptor SO_4^{2-} due to the lower SO_4^{2-} concentration, which resulted in the decrease of H_2S production. Freese and Stuckey (2004) reported the same trend that the H_2S production rate decreased as the COD/SO_4^{2-} ratio increased if the COD/SO_4^{2-} was larger than the theoretical value 0.67, although the increase of the

COD/SO_4^{2-} ratio was by increasing the COD concentration. In addition, they calculated the consumption and production rates based on the changes of sulfate concentration in the bulk liquid phase in conventional biofilm reactors. Therefore, by exploring the inside biofim, the results from this study was supplemented with previous studies. The information extracted from the biofilm would help us understand the internal structure and function of the microbial environment and herein better understand the microbial processes under different operational conditions, which would help reactor design. Previous studies on the consumption and production of substrates in biofilms mainly focused on the conventional biofilms (Hibiya *et al*., 2003; Okabe *et al*., 1999). This study first quantified the consumption and production rates in MAB growing under different COD/SO_4^{2-} ratios. Compared with the other literatures on biofilm studies (Hibiya *et al*., 2003; Okabe *et al*., 1999), NH_4^+-N consumption rates and NO_3^- consumption rate were lower but H_2S production rate is higher than those in the literatures. This might imply these two conditions, COD/SO_4^{2-} ratios of 1 and 2 were favorable for sulfate reduction. This would provide more selections of biofilm reactors and improve reactor design.

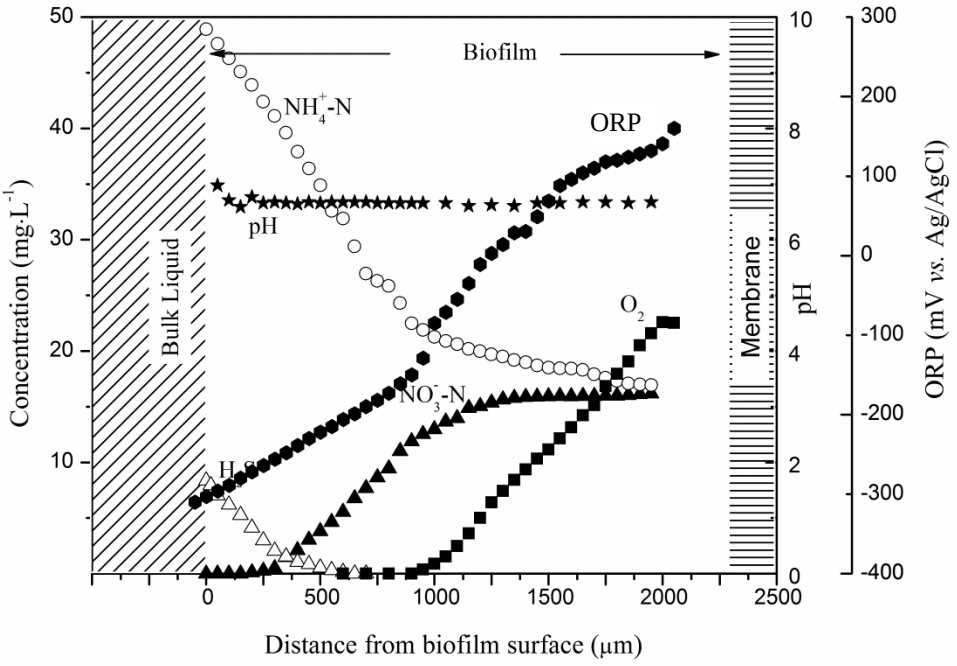

Figure 6-6 Profiles within oxygen-based MAB grown under COD/SO_4^{2-} ratio of 1 and COD/NH_4^+-N ratios of 4

Figure 6-6 illustrates the concentration profiles in MAB growing under under COD/SO_4^{2-} ratio of 1 and COD/NH_4^+-N ratios of 4. This figure combined with Figure 6-2 could be used to explain the change of concentration profiles under different COD/NH_4^+-N ratios. Note that the COD/NH_4^+-N ratio was decreased by increasing NH_4^+-N concentration. From Figure 6-6, the O_2 concentration profile revealed that O_2 penetrated from the gas permeable membrane side, and then depleted at about 900 μm below the biofilm/bulk liquid interface. Compared with Figure 6-2, the O_2 penetration depth decreased in Figure 6-6 (1500 μm in Figure 6-2 and 1200 μm in Figure 6-6), which might be due to more oxygen utilization by nitrification under higher NH_4^+-N concentrations. The

NH_4^+-N concentration decreased from 48.9 mg Ł$^{-1}$ to 22.5 mg Ł$^{-1}$ within 900 μm distance, and then gradually consumed further into the biofilm. Although no NO_3^- was added in the bulk solution, 16 mg Ł$^{-1}$ NO_3^- was detected inside the MAB, which indicated the presence of nitrification. The H_2S concentration profile showed that H_2S penetrated near the bulk liquid-biofilm interface (600 μm below the biofilm/bulk liquid interface).

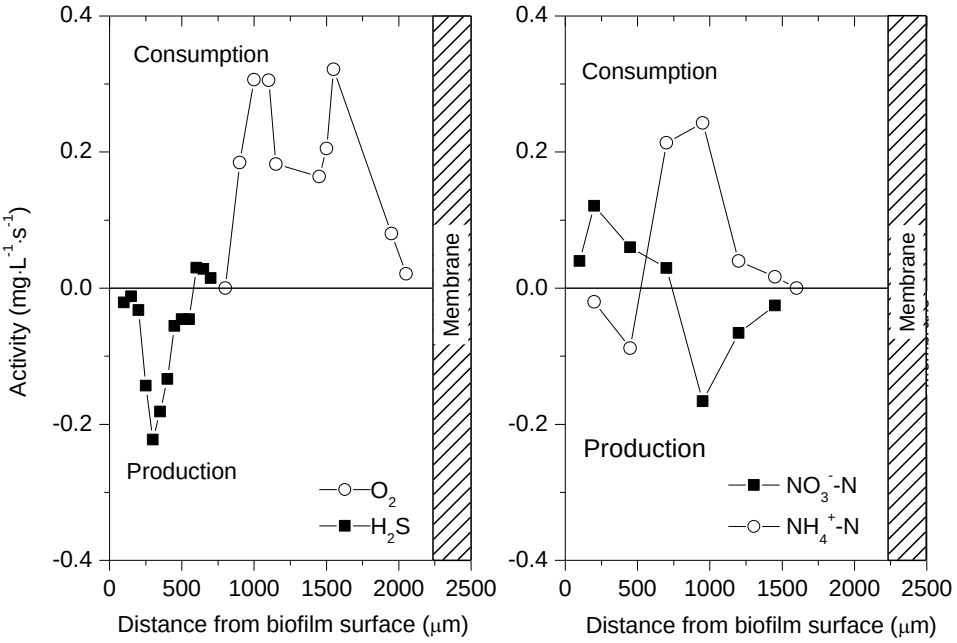

Figure 6-7 Production and consumption rates within oxygen-based MAB grown under COD/SO_4^{2-} ratio of 1 and COD/NH_4^+-N ratios of 4

Figure 6-7 shows the production and consumption rates in an oxygen-based MAB growing under COD/SO_4^{2-} ratio of 1 and COD/NH_4^+-N ratios of 4. For this set of data, the differentiation of raw data resulted in a very noisy profile in concentration profiles, which might be due to the increased nitrogen

metabolism under higher NH_4^+-N concentration. Therefore, more data points instead of raw data points were used to calculate the depth-specific activity in order to increase signal-to-noise ratio and herein extract the information inside the MAB under the ratio of COD/NH_4^+-N ratios of 4. The detailed method of calculation was provided in Chapter 5.

From the NH_4^+-N rates, the maximal NH_4^+-N production rate was 0.09 mg L^{-1} s^{-1} at 450 μm below the bulk liquid-biofilm interface and the maximal NH_4^+-N consumption rate was 0.24 mg L^{-1} s^{-1} at 950 μm below the bulk liquid-biofilm interface. The NH_4^+-N production might be due to the degradation of dead cells and ammonification of organic compounds. The maximal NH_4^+-N consumption rate under the COD/NH_4^+-N ratios of 4 was about 3 times higher than that under the COD/NH_4^+-N ratios of 10 (shown in Figure 6-3), which might indicate the higher nitrification activity under the COD/NH_4^+-N ratios of 4. From the NO_3^--N rates, the maximal NO_3^--N consumption rate was 0.12 mg L^{-1} s^{-1} and the maximal NO_3^--N production rate was 0.17 mg L^{-1} s^{-1}. Compared with Figure 6-3, O_2 consumption consumed by nitrifiers increased when increasing the NH_4^+-N concentration. The maximal H_2S production rate was 0.22 mg L^{-1} s^{-1} and the maximal H_2S consumption rate was negligible. The decrease of the activity of sulfide oxidation might result from the following reason: when the COD/NH_4^+-N ratios decrease by increasing the NH_4^+-N concentration, more O_2 was utilized by nitrifiers. Thereafter, O_2 would be not enough for sulfide oxidation.

Table 6-5 Comparison of total consumption and production rates for the MABs grown under COD/NH_4^+-N ratio of 10 and 4

COD/N	NH_4^+-N	NO_3^--N		H_2S		O_2
	Consumption	Production	Consumption	Production	Oxidation	Consumption
10	0.12	0.13	0.16	1.30	0.52	1.30
4	1.03	0.78	0.32	0.42	Negligible	-
Other data sources	1.00[a]	-	1.17[b]	0.02[b]	-	1.69[b]

Note: The unit of total consumption and production rates is g-N m^{-2} d^{-1}. a - data reported by Hibiya *et al.*, 2003, and b - reported by Okabe *et al.*, 1999.

Table 6-5 listed the comparison of consumption and production rates of O_2, H_2S, NH_4^+-N and NO_3^- for the two conditions: biofilm growing under COD/NH_4^+-N ratio of 10 and 4. The results from Table 6-5 showed that the total NH_4^+-N consumption rates increased by 8.6 times and the NO_3^--N production rate increased by 6 times when the ratio of COD/NH_4^+-N was decreased from 10 to 4. This indicated the COD/NH_4^+-N ratio would affect nitrification activity: higher nitrification activity at lower COD/NH_4^+-N ratios. Note that the decrease of the COD/NH_4^+-N ratio in this study was by increasing the NH_4^+-N concentration. Using oxygen microsensor measurement and molecular techniques, Cole (2005) reported the same trend at different COD/NH_4^+-N ratios by changing NH_4^+-N concentrations. This study expanded the understanding of the internal structure

and functions by the *in situ* measurements using six types of microsensors. Compared with Hibiya *et al*. (2003), the NH_4^+-N consumption rates were is a little higher at the COD/NH_4^+-N ratio of 4 and 9 times lower at the COD/NH_4^+-N ratio of 10.

6.4 Conclusions

The stratification of multiple microbial processes in the oxygen-based MAB was repeatedly demonstrated under different COD/SO_4^{2-} and COD/NH_4^+-N ratios. Sulfate reduction and denitrification existed near the bulk liquid-biofilm interface. Nitrification and sulfide oxidation occurred in the middle of the biofilm. Aerobic oxidation took place near the membrane. The results validated the previous conceptual MAB model and produced previously unavailable biofilm data to future model builders.

The ratios of COD/SO_4^{2-} and COD/NH_4^+-N affected the activities of multiple microbial processes in an oxygen-based MAB. H_2S production rates decreased when the ratio of COD/SO_4^{2-} was increased. Although the multiple microbial processes occurred simultaneously, it was favorable for sulfate reduction under COD/SO_4^{2-} ratios of 1 and 2. By using microsensor measurements this study, for the first time, quantified the consumption and production rates inside MAB growing under different COD/SO_4^{2-} ratios. The COD/NH_4^+-N ratios affected nitrification activity: higher nitrification activity at lower COD/NH_4^+-N ratios as for the COD/NH_4^+-N ratios of 10 and 4. This information helps us understand the internal structure and functions of the

microbial environment and herein better understand the microbial processes under different operational conditions. This would provide more selections of biofilm reactors and improve reactor design.

References

Bhagat, M., J.E. Burgess, A.P.M. Antunes, C.G. Whiteley and J.R. Duncan. 2004. Precipitation of mixed metal residues from wastewater utilising biogenic sulphide. Miner. Eng., 17, 925-932.

Cole, A.C., M.J. Semmens and T.M. LaPara. 2004. Stratification of activity and bacterial community structure in biofilms grown on membranes transferring oxygen. Applied and Environmental Microbiology. 70, 1982-1989.

Cole, A.C., J.W. Shanahan, M.J. Semmens and T.M. LaPara. 2002. Preliminary studies on the microbial community structure of oxygen-based membrane-aerated biofilms treating municipal wastewater. Desalination. 146, 421-426.

de la Rosa, C. and T. Yu. 2006. Development of an automation system to evaluate the three-dimensional oxygen distribution in wastewater biofilms using microsensors. Sensors and Actuators B-Chemical., 113, 47-54.

Freese, L. H. and Stuckey, D. C. 2004. Anaerobic treatment of sulphate-enriched wastewaters. Proceedings of the Institution of Civil Engineers-Water Management **157**(4): 187-195.

Hibiya, K., Terada, A., Tsuneda, S. and Hirata, A. 2003. Simultaneous nitrification and denitrification by controlling vertical and horizontal microenvironment in a membrane-aerated biofilm reactor. Journal of Biotechnology 100(1): 23-32.

Ito, T., J.L. Nielsen, S. Okabe, Y. Watanabe and P.H. Nielsen. 2002. Phylogenetic identification and substrate uptake patterns of sulfate-reducing bacteria inhabiting an oxic-anoxic sewer biofilm determined by combining microautoradiography and fluorescent in situ hybridization. Appl. Environ. Microbiol. 68, 356-364.

Ito, T., S. Okabe, H. Satoh and Y. Watanabe. 2002. Successional development of sulfate-reducing bacterial populations and their activities in a wastewater biofilm growing under microaerophilic conditions. Appl. Environ. Microbiol. 68, 1392-1402.

Kuhl, M. and B.B. Jorgensen. 1992. Microsensor measurements of sulfate reduction and sulfide oxidation in compact microbial communities of aerobic biofilms. Appl. Environ. Microbiol. 58, 1164-1174.

Lu, R. and T. Yu. 2002. Fabrication and evaluation of an oxygen microelectrode applicable to environmental engineering and science. Journal of Environmental Engineering and Science. 1, 225-235.

Okabe, S., T. Ito and H. Satoh. 2003. Sulfate reducing bacterial community structure and their contribution to carbon mineralization in a wastewater biofilm growing under microaerophilic conditions. Appl. Microbiol. Biotechnol., 63, 322-334.

Okabe, S., T. Ito, K. Sugita and H. Satoh. 2005. Succession of internal sulfur cycles and sulfur-oxidizing bacterial communities in microaerophilic wastewater biofilms. Appl. Environ. Microbiol., 71, 2520-2529.

Okabe, S., T. Itoh, H. Satoh and Y. Watanabe. 1999. Analyses of spatial distributions of sulfate-reducing bacteria and their activity in aerobic wastewater biofilms. Appl. Environ. Microbiol., 65, 5107-5116.

Santegoeds, C.M., T.G. Ferdelman, G. Muyzer and D. de Beer. 1998. Structural and functional dynamics of sulfate-reducing populations in bacterial biofilms. Appl. Environ. Microbiol. 64, 3731-3739.

Satoh, H., H. Ono, B. Rulin, J. Kamo, S. Okabe and K.I. Fukushi. 2004. Macroscale and microscale analyses of nitrification and denitrification in biofilms attached on oxygen-based membrane-aerated biofilm reactors. Water Research., 38, 1633-1641.

Tan, S.Y. and Yu, T. 2007. Fabrication of an amperometric h_2s microsensor and its application in wastewater biofilms. Proceedings of International Workshop on Monitoring and Sensors for Water Pollution Control, Beijing, China, June 13-14.

Terada, A., K. Hibiya, J. Nagai, S. Tsuneda and A. Hirata. 2003. Nitrogen removal characteristics and biofilm analysis of a oxygen-based membrane-aerated biofilm reactor applicable to high-strength nitrogenous wastewater treatment. Journal of Bioscience and Bioengineering. 95, 170-178.

Chapter 7

Conclusions and Recommendations

Multiple microbial processes in MABs were investigated by using O_2, pH, ORP, NH_4^+, NO_3^- and H_2S microsensors. The chemical gradients were determined *in situ* in the MABs grown under different operating conditions. The images of the MABs were viewed by using scanning electron microscopy. Based on the experimental results from the microsensor measurements and microscopic pictures, the following conclusions can be drawn:

1 A Clark-type amperometric H_2S microsensor was successfully fabricated. This H_2S microsensor could measure a range from 0 to 600 μM (20.4 mg·L^{-1}) H_2S. Its sensitivity could reach 1.21 pA ·μM^{-1}. The zero currents were less than 5 pA. The response time could be less than 1 second. This H_2S microsensor can be used to measure the change of H_2S concentrations both from the low to high concentrations and from the high to low concentrations, which is very useful for the *in situ* measurement of H_2S concentration in terms of SRB's activity in a biofilm sample. The results from the microsensor measurements were consistent and supplemented with the results from the FISH techniques.

2 This study produced the first experimental evidence on the sulfate reduction process inside the oxygen-based MABs. Besides the sulfate reduction process, the results from microsensor measurements and net specific consumption and production rates revealed simultaneous occurrences of multiple microbial processes in a single piece of MAB. The stratification of multiple microbial

processes in the oxygen-based MAB was determined in following order: sulfate reduction or denitrification, nitrification or sulfide oxidation, aerobic oxidation from the bulk liquid-biofilm interface to the membrane side.

3 The consumption and production rates within MABs growing under various COD/SO_4^{2-} and COD/NH_4^+-N ratios were quantified for the first time based on microsensor measurements. It has been demonstrated that the ratio of COD/SO_4^{2-} and COD/NH_4^+-N could affect the activities of multiple microbial processes in MABs. H_2S production rates decreased when the ratio of COD/SO_4^{2-} was increased. Although the multiple microbial processes occurred simultaneously, it was favorable for sulfate reduction but not beneficial for nitrification and denitrification under the COD/SO_4^{2-} ratios of 1 and 2 at the same COD concentrations. The COD/NH_4^+-N ratios significantly affected nitrification activity: higher nitrification activity at lower COD/NH_4^+-N ratios as for the two conditions, COD/NH_4^+-N ratios of 10 and 4. This information would help understand the internal structure and function of the microbial environment and herein better understand the microbial processes under different operational conditions, which would help reactor design and could provide suggestion for the biofilm selection.

4 The microscopic observations demonstrated quite different biofilm structure from the membrane side to the bulk liquid side: fluffy near the membrane but clay-like near the bulk liquid. This might be due to the high gas pressure from the membrane but low gas pressure from the bulk liquid side. Another difference was observed from the microscopic images: high cell density

was present near the bulk liquid and low cell density near the membrane. The explanation might be that the high concentration of COD and nutrients near the biofilm-liquid interface is more important for cell growth, leading to high cell density.

Due to the complexity of the microbial processes and the biofilm system itself, the following future research works are strongly recommended:

1 More microsensors are required to be developed and improved in order to explain more clearly the multiple microbial processes. According to this recommendation, with respect to sulfate reduction process, a sulfate microsensor has been developed by an MSc student, Shujie Ren in our group. Future works on the improvements of the performance of this sulfate microsensor are also recommended.

2 A combination of microsensor techniques and other analytical methods such as molecular techniques are important to elucidating the relationship of the metabolic activity and microbial community structure involved in multiple microbial processes. According to this recommendation, another Ph.D student, Hong Liu, in our group has been investigating the distribution of SRB using molecular techniques.

3 As detected in this study, shown in Chapter 5 and 6, more in-deep research such as anaerobic ammonium oxidation is also proposed.

Appendices

Appendix A - Data for Figures in Chapter 3

Data for Figure 3-5 – Calibration curves of oxygen microsensors

	Oxygen concentration ($mg \cdot L^{-1}$)	Current (nA) #1 oxygen microsensor	Current (nA) #2 oxygen microsensor
Nitrogen	0	0.05	0
Air	8.36	2.12	2.06
Oxygen	40	9.84	10.33

Data for Figure 3-7 – Calibration curves of pH microsensors

pH	The potential readings (mV) (vs. Ag/AgCl) #1 pH microsensor	#2 pH microsensor
6	91	15
7	33	-40
8	-29	-97
9	-79	-157

Data for Figure 3-8 – Calibration curves of ammonia microsensors

Ammonia concentration (M)	Ammonia concentration ($mg \cdot L^{-1}$) as NH_4^+	-LOG(M)	The potential readings (mV) (vs. Ag/AgCl) #1 ammonia microsensor	#2 ammonia microsensor
1.00E-05	0.18	5	-34	-38
1.00E-04	1.8	4	24	9
1.00E-03	18	3	74	71
1.00E-02	180	2	135	123

Data for Figure 3-9 – Calibration curves of nitrate microsensors

Nitrate concentration			The potential readings (mV) (vs. Ag/AgCl)	
(M)	(mg•L^{-1}) as NO_3^-	-LOG (M)	#1 nitrate microsensor	#2 nitrate microsensor
1.00E-05	0.62	5	265	255
1.00E-04	6.2	4	210	207
1.00E-03	62	3	148	156
1.00E-02	620	2	101	107

Data for Figure 3-10 – Potential response of ORP microsensors in standard and reference solutions

Standard or reference solutions	Nominal potential* (mV Vs. Ag/AgCl)	Measured potential (mV) (Vs. Ag/AgCl)	
		#1 ORP microsensor	#2 ORP microsensor
Ferrous-Ferric standard solution	463	465	465
pH4 quinhydrone reference solution	265	257	273
pH7 quinhydrone reference solution	88.4	81	85

*: The values of nominal potentials were for 23 ^{0}C.

Appendix B Data for Figures in Chapter 4

Data for Figure 4-4 – Calibration curves of H_2S microsensors

Total sulfide concentration		Current (pA)	
(μM)	$mg \cdot L^{-1}$	#1 H_2S microsensor	#2 H_2S microsensor
0	0	2	5
30	1.02	19	45
300	10.2	232	432
600	20.4	564	724

Data for Figure 4-5 – An illustration of H_2S concentration profile in a conventional biofilm

Distance from the biofilm surface	Concentration	
	($mg \cdot L^{-1}$)	(μM)
0	0.00	0.00
30	0.00	0.00
130	0.00	0.00
230	0.86	25.16
330	1.22	35.78
430	1.08	31.80
530	1.53	45.08
630	1.67	49.06
730	1.40	41.09
830	1.76	51.72
930	1.94	57.03
1030	2.30	67.65
1130	7.49	220.35
1150	8.58	252.22
1160	9.39	276.12
1170	9.79	288.07
1180	10.43	306.66
1190	10.74	315.96
1200	11.24	330.56
1210	11.19	329.24
1220	11.46	337.20
1230	11.65	342.52
1240	11.78	346.50
1250	11.78	346.50

Appendix C Data for Figures in Chapter 5

Data for Figure 5-1 – Reactor operating data for COD in the influent and effluent of MABR 1

Reactor operating time (Days)	Influent COD ($mg \cdot L^{-1}$)	Effluent COD ($mg \cdot L^{-1}$)
3	254.8	92.3
4	274.8	207.3
5	212.3	42.3
7	237.3	89.8
9	262.0	122.0
10	270.0	141.0
11	247.0	73.0
14	241.0	51.0
16	286.0	58.0
18	218.8	34.8
22	210.8	46.8
23	220.8	60.8
25	214.8	86.8
31	224.8	48.8
35	226.8	36.8
36	221.8	68.8
37	207.8	42.8
39	228.8	107.8
42	238.8	68.8
44	240.3	85.3
51	287.8	95.3
56	242.8	127.8
59	298.2	96.0
63	246.2	94.2
64	214.2	64.2
65	212.2	72.2
67	218.2	58.2
70	212.2	98.2
71	257.0	92.7
72	275.9	119.9
73	271.2	39.5
74	284.2	52.5
75	232.2	25.3
78	262.9	103.3

Data for Figure 5-1 – Reactor operating data for COD in the influent and effluent of MABR 1 (Cont')

Reactor operating time (Days)	Influent COD ($mg \cdot L^{-1}$)	Effluent COD ($mg \cdot L^{-1}$)
85	265.3	118.7
92	258.6	62.6
105	254.6	96.6
109	260.6	106.6
113	277.6	86.6
115	224.6	64.6
119	226.0	65.5
128	209.3	39.3
136	223.0	74.3
142	230.5	104.3
149	271.3	83.7
156	268.3	119.4
163	295.1	92.6
169	253.4	77.7
196	220.6	68.8
198	247.4	116.4
200	283.3	67.4
202	259.6	58.6
205	262.6	97.0
221	242.7	31.6
225	220.0	20.0
227	265.8	37.0
228	197.8	10.6
234	342.4	85.8
239	342.4	4.3
240	289.2	4.8
249	230.1	65.4
252	191.5	38.7
254	252.4	75.2
257	265.5	73.9
263	242.8	105.0
273	257.6	110.1
277	293.7	59.3
279	242.1	59.3
283	190.8	61.3
286	244.7	74.1
288	226.6	80.7

Data for Figure 5-2 – Reactor operating data for sulfate concentration in the influent and effluent of MABR 1

Reactor operating time (Days)	Influent SO_4^{2-} ($mg \cdot L^{-1}$)	Effluent SO_4^{2-} ($mg \cdot L^{-1}$)
2	204.9	84.5
4	244.1	205.9
8	307.5	260.6
9	289.3	111.9
10	403.4	117.9
15	220.4	165.7
18	228.5	147.8
24	227.0	137.6
25	232.2	127.8
28	236.3	117.7
29	228.3	130.6
31	260.1	139.8
32	259.9	127.9
35	227.8	95.9
36	233.3	128.8
37	232.6	92.4
38	238.2	100.9
39	239.0	119.8
42	236.9	99.2
43	238.0	107.2
44	237.9	105.4
46	237.4	116.2
49	214.5	89.7
50	217.8	85.1
51	215.5	70.7
52	216.5	68.1
53	212.5	66.4
56	222.9	109.2
71	222.5	71.5
72	222.7	65.9
73	222.5	114.4
86	227.5	56.7
91	237.3	102.8
93	240.7	79.2
95	239.3	55.6
98	236.2	67.0
99	227.4	65.7
105	239.8	58.8

Data for Figure 5-2 – Reactor operating data for sulfate concentration in the influent and effluent of MABR 1 (Cont')

Reactor operating time (Days)	Influent SO_4^{2-} ($mg \cdot L^{-1}$)	Effluent SO_4^{2-} ($mg \cdot L^{-1}$)
106	267.9	134.2
113	243.1	86.4
114	214.6	79.9
115	202.2	71.6
116	204.6	55.3
119	196.6	60.3
123	202.7	35.3
126	205.1	73.6
136	233.7	61.2
137	225.7	59.4
142	232.3	90.1
151	231.4	59.9
154	237.2	61.3
156	226.1	46.0
163	231.9	31.8
169	227.5	57.1
196	207.5	82.8
205	214.5	56.6
210	219.3	63.1
220	218.6	37.7
221	221.4	49.2
225	207.4	60.9
227	207.9	56.6
228	209.2	57.5
232	217.1	63.2
234	214.9	56.7
235	213.9	46.8
239	225.7	52.1
240	225.9	113.1
242	224.4	68.0
245	222.9	58.7
247	221.4	50.1
249	214.5	51.7
252	214.0	51.6
254	226.9	49.5
257	218.6	44.8
259	219.8	42.4
261	217.2	44.9

Data for Figure 5-2 – Reactor operating data for sulfate concentration in the influent and effluent of MABR 1 (Cont')

Reactor operating time (Days)	Influent SO_4^{2-} ($mg \cdot L^{-1}$)	Effluent SO_4^{2-} ($mg \cdot L^{-1}$)
263	217.4	45.9
273	223.0	38.1
275	223.6	52.0
277	223.3	49.5
279	237.4	56.5
283	223.3	62.7
286	232.2	47.9
288	227.9	31.2

Data for Figure 5-3 – Reactor operating data for ammonia concentration in the influent and effluent of MABR 1

Reactor operating time (Days)	Influent NH_4^+ ($mg \cdot L^{-1}$)	Effluent NH_4^+ ($mg \cdot L^{-1}$)
205	16.5	12.5
207	16.9	15.6
219	20.7	20.1
220	17.9	6.9
225	19.6	12.2
231	17.5	11.3
232	16.9	12.9
233	15.8	12.4
234	16.9	12.1
235	18.7	10.8
239	15.8	8.0
240	17.5	11.6
241	19.3	15.0
242	22.2	8.8
245	17.0	11.9
246	16.1	11.4
247	17.9	11.1
248	18.4	14.3
249	19.6	8.2
252	20.4	12.3
253	18.3	11.3
254	14.5	12.9
255	18.7	14.1
256	20.1	12.7
259	19.6	12.3
260	19.2	11.2
262	21.4	12.5
267	20.1	9.6
268	20.3	12.8
269	22.2	12.5
273	20.6	12.4
274	25.3	12.1
276	23.1	13.4
277	16.4	15.8
280	19.9	11.7
281	19.8	10.6
283	22.0	12.9
289	20.3	15.5

Data for Figure 5-4 – Profiles of O_2, pH, ORP, NH_4^+-N, NO_3^- and H_2S in a piece of MAB

Depth µm	O_2 mg Ł$^{-1}$	Depth µm	pH	Depth µm	ORP mV	Depth µm	NH_4^+-N mg•L^{-1}	Depth µm	NO_3^--N mg•L^{-1}	Depth µm	H_2S mg•L^{-1}
-50	0.0	-50	7.34	-75	-376	-50	17.39	-50	0.32	-50	10.27
0	0.0	0	7.32	-25	-373	0	17.35	0	0.36	0	10.14
50	0.0	50	7.33	25	-369	50	17.32	50	0.55	50	10.02
100	0.0	100	7.35	75	-363	100	17.30	100	0.60	100	9.70
150	0.0	150	7.34	125	-353	150	17.28	120	0.64	140	9.44
200	0.0	200	7.36	175	-351	200	17.28	140	0.68	180	9.28
250	0.0	250	7.35	225	-346	250	17.25	160	0.72	200	9.26
300	0.0	300	7.38	275	-343	300	17.21	180	0.78	220	9.12
350	0.0	350	7.39	325	-339	320	17.15	200	0.83	240	9.06
400	0.0	400	7.38	375	-338	340	17.09	220	1.05	260	8.70
450	0.0	450	7.36	425	-336	360	16.90	240	1.26	280	8.48
500	0.0	500	7.36	475	-329	380	16.62	260	1.37	300	8.23
550	0.0	550	7.39	505	-321	400	16.33	280	1.42	320	8.00
600	0.2	600	7.35	525	-310	420	16.01	300	1.54	340	7.94
650	0.5	650	7.38	545	-281	440	15.76	320	1.66	360	7.78
700	0.8	700	7.35	565	-275	460	15.37	340	1.72	380	7.65
720	0.1	750	7.36	585	-244	480	15.01	360	1.89	400	7.50
750	1.0	800	7.38	605	-233	500	14.72	380	1.96	420	7.26
770	1.1	850	7.39	625	-216	520	14.64	400	2.05	440	6.91
800	1.1	900	7.38	635	-205	540	14.13	420	2.16	460	6.50
820	1.7	950	7.40	645	-174	560	13.95	440	2.30	480	6.27
850	1.9	1000	7.36	655	-145	580	13.86	460	2.45	500	6.04
870	2.6	1050	7.36	665	-132	600	13.69	480	2.58	520	4.22
890	2.8	1100	7.38	675	-104	620	13.56	500	2.61	540	3.68
900	3.1	1150	7.39	695	-72	640	13.42	520	2.73	560	3.46
920	3.8	1200	7.36	715	-43	660	13.29	540	2.89	580	2.98
950	4.2	1250	7.40	725	-16	680	13.15	560	2.96	600	2.21
970	5.1			745	10	700	13.07	580	3.05	620	1.66
1000	5.4			775	25	720	12.96	600	3.11	650	1.38
1020	5.7			805	34	740	12.84	620	3.15	700	1.02
1050	6.3			825	57	760	12.76	640	3.19	750	0.80
1070	6.6			845	66	780	12.69	660	3.23	800	0.51

Data for Figure 5-4 – Profiles of O_2, pH, ORP, NH_4^+-N, NO_3^- and H_2S in a piece of MAB (Cont')

Depth µm	O_2 mg Ł$^{-1}$	Depth µm	ORP mV	Depth µm	NH_4^+-N mg•L^{-1}	Depth µm	NO_3^--N mg•L^{-1}	Depth µm	H_2S mg•L^{-1}
1100	7.4	875	96	800	12.62	680	3.26	850	0.22
1120	7.9	895	123	820	12.54	700	3.34	900	0.10
1150	8.5	925	137	840	12.48	720	3.40	950	0.03
1200	9.5	945	141	860	12.46	740	3.43	1000	0.02
		975	147	880	12.45	760	3.49	1050	0.00
		1005	162	900	12.42	780	3.52	1100	0.00
		1025	169	920	12.41	800	3.56	1150	0.00
		1075	172	940	12.40	820	3.61	1200	0.00
		1125	179	960	12.40	840	3.63	1250	0.00
		1175	181	980	12.39	860	3.68		
		1225	184	1000	12.38	880	3.70		
				1020	12.36	900	3.72		
				1040	12.35	920	3.76		
				1060	12.32	940	3.79		
				1080	12.30	960	3.80		
				1100	12.29	980	3.82		
				1120	12.28	1000	3.81		
				1140	12.25	1020	3.84		
				1160	12.22	1040	3.83		
				1180	12.18	1060	3.85		
				1200	12.16	1080	3.84		
						1100	3.86		
						1120	3.86		
						1140	3.87		
						1160	3.89		
						1180	3.90		
						1200	3.92		

Data for Figure 5-5 – The net specific consumption and production rates of ammonia, nitrate, H_2S and O_2 in the MAB

Depth µm	O_2 mg•L^{-1} s^{-1}	Depth µm	H_2S mg•L^{-1} s^{-1}	Depth µm	NO_3^--N mg•L^{-1} s^{-1}	Depth µm	NH_4^+-N mg•L^{-1} s^{-1}
0	0	0	-0.05	120	0.00	0	0
50	0	50	-0.04	140	0.03	50	0
100	0	100	-0.03	160	0.11	100	0.00
150	0	150	-0.02	180	0.17	150	0.00
200	0	200	-0.07	200	0.20	200	-0.09
250	0.00	250	-0.02	220	0.02	250	-0.12
300	0.00	300	-0.04	240	-0.03	300	-0.16
350	0.01	350	-0.02	260	-0.08	320	-0.06
400	0.01	400	-0.25	280	0.02	340	-0.07
450	0.02	450	-0.27	300	-0.11	360	-0.01
500	0.06	500	0.05	320	-0.10	380	-0.11
550	0.09	550	0.13	340	-0.10	400	-0.25
600	0.09	600	0.29	360	0.03	420	-0.51
650	0.03	650	0.35	380	0.07	440	-0.64
700	0.05	700	0.16	400	0.09	460	-0.25
750	0.17	750	0.07	420	0.08	480	-0.02
800	0.34	800	0.04	440	-0.02	500	0.47
850	0.33	850	0.06	460	-0.06	520	0.26
900	0.16	900	0.06	480	-0.06	540	0.46
950	0.03	950	0.04	500	0.02	560	0.22
1050	0.00	1000	0.02	520	0.02	580	0.19
		1050	0.01	540	-0.05	600	0.02
		1100	0.00	560	-0.08	620	-0.01
		1150	0.00	580	-0.09	640	0.05
		1200	0.00	600	-0.05	660	0.04
				620	-0.04	680	0.06
				640	0.01	700	0.02
				660	0.03	720	0.03
				680	0.03	740	0.05
				700	0.00	760	0.05
				720	-0.03	780	0.03
				740	-0.02	800	0.03
				760	-0.02	820	0.07
				780	-0.01	840	0.09
				800	-0.01	860	0.06
				820	-0.02	880	0.02
				840	-0.01	900	0.02
				860	-0.02	920	0.02
				880	0.00	940	0.02

Data for Figure 5-5 – The net specific consumption and production rates of ammonia, nitrate, H_2S and O_2 in the MAB (Cont')

Depth µm	O_2 mg•L^{-1} s^{-1}	Depth µm	H_2S mg•L^{-1} s^{-1}	Depth µm	NO_3^--N mg•L^{-1} s^{-1}	Depth µm	NH_4^+-N mg•L^{-1} s^{-1}
				900	-0.01	960	-0.01
				920	-0.01	980	-0.01
				940	-0.04	1000	-0.02
				960	-0.02	1020	-0.01
				980	-0.03	1040	-0.01
				1000	0.01	1060	0.01
				1020	-0.02	1080	0.01
				1040	0.01	1100	-0.01
				1060	-0.02	1120	-0.03
				1080	0.02	1140	-0.02
				1100	0.00	1160	0.01
				1120	0.02	1180	0.05
				1140	0.01	1200	0.05

Appendix D Data for Figures in Chapter 6

Data for Figure 6-2 Profiles within oxygen-based MAB grown under COD/SO_4^{2-} ratio of 1 and COD/NH_4^+-N ratio of 10

Depth μm	ORP mV	Depth μm	NO_3^--N mg•L^{-1}	Depth μm	NH_4^+-N mg•L^{-1}	Depth μm	pH	Depth μm	H_2S mg•L^{-1}	Depth μm	O_2 mg•L^{-1}
0	-312	0	0	-50	16.23	-50	7.32	-50	11.75	0	0.00
100	-308	100	0	0	16.12	0	7.33	0	11.31	100	0.00
200	-298.4	200	0.15	50	16.01	50	7.35	50	11.20	200	0.00
300	-255	250	0.17	100	15.89	100	7.34	100	10.86	300	0.00
400	-189	300	0.2	150	15.78	150	7.36	150	10.09	400	0.00
500	-156	350	0.4	200	15.67	200	7.35	200	10.09	500	0.00
600	-113	400	0.7	250	15.56	250	7.38	250	7.87	600	0.25
700	-95.6	500	1.05	300	15.44	300	7.39	300	5.54	700	0.52
750	-18.4	600	1.49	350	15.32	350	7.38	350	3.55	750	0.82
770	-68	700	1.86	400	15.21	400	7.36	400	2.44	800	0.98
800	-46.7	750	2.12	500	15.06	450	7.36	450	2.22	850	1.25
850	-61.1	800	2.65	600	14.84	500	7.39	500	1.00	900	1.60
900	-13.3	850	3.04	700	14.62	550	7.35	550	0.44	950	1.73
950	9.6	900	3.41	750	14.51	600	7.38	600	0.22	1000	2.03
1000	34.3	950	3.82	800	14.40	650	7.35	650	0.00	1050	2.61
1050	65.9	1000	4.24	850	14.29	700	7.36	700	0.00	1100	2.83
1100	141.3	1050	4.65	900	14.18	750	7.38	750	0.00	1150	3.03
1150	137.4	1100	5.12	950	14.09	800	7.39	800	0.00	1200	3.35
1200	181.4	1150	5.56	1000	14.03	850	7.38	850	0.00	1250	3.57
1250	147.2	1200	5.98	1050	13.95	900	7.4	900	0.00	1300	3.89
1300	184.2	1250	6.32	1100	13.89	950	7.39	950	0.00	1350	4.27
1350	189.2	1300	6.56	1150	13.83	1000	7.39	1050	0.00	1400	4.62
1400	195.6	1350	6.75	1200	13.77	1050	7.4	1150	0.00	1450	5.55
1450	184	1400	6.89	1250	13.72	1100	7.4			1500	6.57
1500	188.6	1450	6.99	1300	13.68	1150	7.4			1550	7.02
1550	172.9	1500	7.05	1350	13.66	1200	7.41			1600	7.52
1600	185	1550	7.12	1400	13.63	1250	7.41			1650	8.24
1650	192	1600	7.18	1450	13.62	1300	7.4			1700	8.68
1700	199	1650	7.19	1500	13.61	1350	7.38			1750	9.39
1750	205	1700	7.21	1550	13.60	1400	7.37			1800	10.56
1800	212	1750	7.2	1600	13.58	1450	7.36			1850	15.67
1850	208	1800	7.26	1650	13.57	1500	7.36			1900	16.45
1900	206	1850	7.24	1700	13.56	1550	7.38			1950	17
				1750	13.54	1600	7.39				

Data for Figure 6-2 Profiles within oxygen-based MAB grown under COD/SO_4^{2-} ratio of 1 and COD/NH_4^+-N ratio of 10 (Cont')

Depth µm	ORP mV	Depth µm	NO_3^--N mg•L^{-1}	Depth µm	NH_4^+-N mg•L^{-1}	Depth µm	pH	Depth µm	H_2S mg•L^{-1}	Depth µm	O_2 mg•L^{-1}
				1800	13.52	1650	7.36				
				1850	13.50	1700	7.38				
				1900		1750	7.42				
				1950		1800	7.41				
						1850	7.43				
						1900	7.41				
						1950	7.38				
						2000	7.36				
						2050	7.38				
						2100	7.37				
						2150	7.35				

Data for Figure 6-3 Production and consumption rates within oxygen-based MAB grown under COD/SO_4^{2-} ratio of 1 and COD/NH_4^+-N ratio of 10

Depth µm	O_2 mg•L^{-1} s^{-1}	Depth µm	H_2S mg•L^{-1} s^{-1}	Depth µm	NO_3^-N mg•L^{-1} s^{-1}	Depth µm	NH_4^+-N mg•L^{-1} s^{-1}
400	0	0	-0.10	300	0.00	100	0
500	0.06	50	-0.12	400	0.02	200	0.00
600	0.03	100	-0.23	500	0.08	300	0.00
700	0.03	150	-0.37	600	0.15	400	0.00
750	0.01	200	-0.60	700	0.15	500	0.00
800	0.04	250	-0.27	750	0.01	600	0.00
850	0.06	300	0.14	770	0.00	700	0.00
900	0.04	350	0.44	800	0.00	750	0.00
950	-0.04	400	0.38	850	-0.01	770	0.00
1000	-0.06	450	0.15	900	0.00	800	0.00
1050	-0.02	500	0.17	950	0.00	850	0.00
1100	0.03	550	0.17	1000	0.00	900	0.00
1150	0.05	600	0.20	1050	0.01	950	0.00
1200	0.13	650	0.11	1100	0.01	1000	-0.03
1250	0.23	700	0.00	1150	0.01	1050	-0.06
1300	0.23			1200	-0.01	1100	-0.08
1350	0.05			1250	-0.03	1150	-0.02
1400	-0.11			1300	-0.06	1200	0.06
1450	-0.12			1350	-0.06	1250	0.08
1500	-0.02			1400	-0.06	1300	0.04
1550	0.11			1450	-0.05	1350	0.01
1600	0.89			1500	-0.03	1400	0.01
1650	0.87			1550	-0.02	1450	0.01
1700	0.69			1600	-0.02	1500	0.01
1750	0.13			1650	-0.01	1550	0.01
1800	0.15			1700	-0.02	1600	0.01
1850	0.15					1650	0.00
1900	0.03					1700	0.01
1950	0.01					1750	0.01
						1800	0.01
						1850	0.01
						1900	0.01

Data for Figure 6-4 Profiles within oxygen-based MAB grown under COD/SO_4^{2-} ratio of 2 and COD/NH_4^+-N ratio of 10

Depth µm	ORP mV	Depth µm	NO_3^--N mg•L^{-1}	Depth µm	NH_4-N mg•L^{-1}	Depth µm	pH	Depth µm	H_2S mg•L^{-1}	Depth µm	O_2 mg•L^{-1}
0	-346.9	0	0	0	16.34	0	7.32	-50	7.58	-50	0
100	-343.9	50	0	50	16.13	50	7.33	0	7.43	0	0.00
200	-337.5	100	0	100	15.86	100	7.35	50	7.03	50	0.00
300	-330.4	150	0	150	15.63	150	7.34	100	6.31	100	0.00
400	-286.7	200	0.13	200	15.41	200	7.36	150	5.82	150	0.00
450	-153.6	250	0.25	250	15.23	250	7.35	200	5.54	200	0.00
550	-154.2	300	0.49	300	15.11	300	7.38	250	4.32	250	0.00
650	-109.2	350	1.05	350	14.97	350	7.39	300	3.21	300	0.00
750	-60	400	1.49	400	14.82	400	7.38	350	2.05	350	0.00
850	-40	450	1.86	450	14.7	450	7.36	400	1.21	400	0.00
950	-20	500	2.12	500	14.59	500	7.36	450	0.87	450	0.00
1050	67	550	2.65	550	14.43	550	7.39	500	0.42	500	0.00
1100	72.8	600	3.04	600	14.32	600	7.35	550	0	600	0.18
1150	110	650	3.41	650	14.18	650	7.38	600	0	650	0.24
1200	130	700	3.82	700	14.02	700	7.35	650	0	700	0.65
1250	140	750	4.24	750	13.88	750	7.36	700	0	730	0.77
1350	150	800	4.65	800	13.72	800	7.38	750	0	750	0.86
1450	160	850	5.12	850	13.59	850	7.39	800	0	800	1.20
1550	156	900	5.56	900	13.41	900	7.38	850	0	850	1.50
1750	178	950	5.98	950	13.23	950	7.4	900	0	900	1.87
1850	189	1000	6.36	1000	13.18	1000	7.39			920	2.20
1950	201	1050	6.7	1050	13.16	1050	7.39			940	2.37
		1100	6.98	1100	13.14	1100	7.4			950	2.43
		1150	7.18	1150	13.11	1150	7.4			970	2.73
		1200	7.32	1200	13.08	1200	7.4			1000	2.96
		1250	7.45	1250	13.06	1250	7.41			1020	3.18
		1300	7.48	1300	13.04	1300	7.41			1040	3.32
		1350	7.46	1350	13.02	1350	7.4			1050	3.45
		1400	7.49	1400	13.03	1400	7.38			1070	3.76
		1450	7.43	1450	13.01	1450	7.37			1090	3.89
		1500	7.48	1500	13	1500	7.36			1100	3.98
		1550	7.49	1550	12.98	1550	7.36			1120	4.47
		1600	7.51	1600	12.97	1600	7.38			1140	4.58
		1650	7.52	1650	12.96	1650	7.39			1150	4.68
		1700	7.53	1700	12.95	1700	7.36			1170	4.98
		1750	7.54	1750	12.96	1750	7.38			1200	5.13
		1800	7.55	1800	12.97	1800	7.42			1220	5.63
		1850	7.55	1850	12.96	1850	7.41			1240	6.00
		1900	7.57	1900	12.95	1900	7.43			1250	6.05

Data for Figure 6-4 Profiles within oxygen-based MAB grown under COD/SO_4^{2-} ratio of 2 and COD/NH_4^+-N ratio of 10 (Cont')

Depth µm	NO_3^--N mg•L^{-1}	Depth µm	NH_4-N mg•L^{-1}	Depth µm	pH	Depth µm	O_2 mg•L^{-1}
1950	7.56	1950	12.94	1950	7.41	1270	6.47
						1300	6.71
						1320	7.04
						1350	7.23
						1400	7.70
						1450	8.02
						1500	8.47
						1550	9.16
						1600	9.48
						1650	10.00
						1700	10.53
						1750	12.03
						1800	13.45
						1850	14.87
						1900	15.67
						1950	16.89
						2000	17.02

Data for Figure 6-5 Production and consumption rates within oxygen-based MAB grown under COD/SO_4^{2-} ratio of 2 and COD/NH_4^+-N ratio of 10

Depth µm	O_2 mg•L^{-1} s^{-1}	Depth µm	H_2S mg•L^{-1} s^{-1}	Depth µm	NO_3^--N mg•L^{-1} s^{-1}	Depth µm	NH_4^+-N mg•L^{-1} s^{-1}
300	0	100	-0.08	0	0.00	0	0
400	0.01	150	-0.11	50	0.00	50	0.00
500	0.08	200	-0.22	100	0.00	100	0.02
600	0.09	250	-0.12	150	0.05	150	0.03
700	0.04	300	0.03	200	0.08	200	0.02
800	0.16	350	0.21	250	0.10	250	0.01
900	0.15	400	0.21	300	0.09	300	0.01
1000	0.03	450	0.16	350	0.01	350	0.00
1100	0.23	500	0.13	400	-0.01	400	0.00
1200	0.37	550	0.13	450	-0.02	450	0.00
1300	-0.02	600	0.10	500	0.02	500	0.00
1400	-0.03	650	0.05	550	0.00	550	-0.01
1500	0.05	700	0.00	600	0.00	600	-0.01
1600	0.18			650	0.00	650	0.00
1700	0.50			700	0.01	700	0.00
1800	0.00			750	0.01	750	0.00
1900	0.05			800	0.01	800	0.00
2000	0.05			850	-0.01	850	0.02
				900	-0.02	900	0.04
				950	-0.03	950	0.04
				1000	-0.04	1000	0.02
				1050	-0.05	1050	0.00
				1100	-0.05	1100	0.00
				1150	-0.05	1150	0.00
				1200	-0.05	1200	0.01
				1250	-0.04	1250	0.00
				1300	-0.03	1300	0.00
				1350	-0.01	1350	0.00
				1400	-0.00	1400	0.00
				1450	0.01	1450	0.00
				1500	0.00	1500	0.00
				1550	0.00	1550	0.00
				1600	0.00	1600	0.00
				1650	0.00	1650	0.00
				1700	0.00	1700	0.00
				1750	0.00	1750	0.00
				1800	0.00	1800	0.03
				1850	0.00	1850	-0.01
				1900	0.00	1900	-0.01
				1950	0.00	1950	0.00

Data for Figure 6-6 Profiles within oxygen-based MAB grown under COD/SO_4^{2-} ratio of 1 and COD/NH_4^+-N ratio of 4

Depth μm	ORP mV	Depth μm	NO_3^--N mg•L^{-1}	Depth μm	NH_4^+-N mg•L^{-1}	Depth μm	pH	Depth μm	H_2S mg•L^{-1}	Depth μm	O_2 mg•L^{-1}
-50	-310	0	0	0	48.90	50	6.98	0	8.36	600	0
0	-303	50	0	50	47.60	100	6.71	20	7.95	700	0
50	-296	100	0	100	46.30	150	6.59	50	7.02	800	0
100	-289	150	0	150	45.10	200	6.77	100	6.2	900	0
150	-280	200	0.13	200	43.90	250	6.66	150	5.26	950	0.36
200	-272	250	0.25	250	42.40	300	6.68	200	4.13	1000	0.89
250	-264	300	0.49	300	41.12	350	6.66	250	2.98	1050	1.54
300	-256	350	1.49	350	39.60	400	6.64	300	2.06	1100	2.48
350	-248	400	2.12	400	37.90	450	6.68	350	1.53	1150	3.62
400	-239	450	3.04	450	36.40	500	6.66	400	1.05	1200	5.02
450	-230	500	3.82	500	34.90	550	6.68	450	0.86	1250	6.42
500	-222	550	4.65	550	32.60	600	6.68	500	0.56	1300	7.44
550	-215	600	5.56	600	31.91	650	6.68	550	0.32	1350	8.42
600	-206	650	6.78	650	29.40	700	6.68	600	0.16	1400	9.36
650	-199	700	7.68	700	26.95	750	6.66	650	0	1450	10.34
700	-190	750	8.65	750	26.30	800	6.66	700	0	1500	11.16
750	-182	800	9.45	800	25.83	850	6.66			1550	12.14
800	-173	850	11.01	850	24.30	900	6.66			1600	13.16
850	-161	900	11.89	900	22.50	950	6.66			1650	14.23
900	-150	950	12.56	950	21.90	1050	6.66			1700	15.13
950	-129	1000	12.98	1000	21.26	1150	6.61			1750	16.85
1000	-85	1050	13.65	1050	20.90	1250	6.63			1800	17.95
1050	-71.3	1100	13.98	1100	20.60	1350	6.61			1850	19.05
1100	-55	1150	14.87	1150	20.20	1450	6.66			1900	20.53
1150	-35	1200	15.05	1200	19.98	1550	6.66			1950	21.59
1200	-11	1250	15.37	1250	19.70	1650	6.68			2000	22.59
1250	2.8	1300	15.65	1300	19.50	1750	6.68			2050	22.53
1300	14	1350	15.78	1350	19.20	1850	6.66				
1350	28.7	1400	15.89	1400	19.00	1950	6.68				
1400	30.5	1450	15.92	1450	18.70						
1450	49	1500	15.93	1500	18.50						
1500	68.6	1550	15.96	1550	18.45						
1550	88.2	1600	15.93	1600	18.42						
1600	96	1650	15.95	1650	18.30						
1650	104	1700	15.97	1700	17.90						
1700	110	1750	15.98	1750	17.60						
1750	118	1800	16	1800	17.30						
1800	120	1850	16.05	1850	17.10						
1850	123.8	1900	16.12	1900	17.00						

Data for Figure 6-6 Profiles within oxygen-based MAB grown under COD/SO_4^{2-} ratio of 1 and COD/NH_4^+-N ratio of 4 (Cont')

Depth µm	ORP mV	Depth µm	NO_3^--N $mg \cdot L^{-1}$	Depth µm	NH_4^+-N $mg \cdot L^{-1}$
1900	128	1950	16.19	1950	16.93
1950	132				
2000	140.7				
2050	160				

Data for Figure 6-7 Production and consumption rates within oxygen-based MAB grown under COD/SO_4^{2-} ratio of 1 and COD/NH_4^+-N ratio of 4

Depth µm	O_2 mg•L^{-1} s^{-1}	Depth µm	H_2S mg•L^{-1} s^{-1}	Depth µm	NO_3^--N mg•L^{-1} s^{-1}	Depth µm	NH_4^+-N mg•L^{-1} s^{-1}
800	0	100	-0.021	100	0.04	200	-0.02
900	0.18	150	-0.012	200	0.12	450	-0.09
1000	0.31	200	-0.032	450	0.06	700	0.21
1100	0.31	250	-0.143	700	0.03	950	0.24
1150	0.18	300	-0.222	950	-0.17	1200	0.04
1450	0.16	350	-0.181	1200	-0.07	1450	0.02
1500	0.21	400	-0.133	1450	-0.03	1600	0.00
1550	0.32	450	-0.056				
1950	0.08	500	-0.046				
2050	0.02	550	-0.046				
		600	0.030				
		650	0.028				
		700	0.015				